Langtaosha (LTS) Preprint doi: https://doi.org/10.65215/apb7tn58 This version posted November 28, 2025. The copyright holder for this preprint (which was not certified by peer review) is the author/funder. Creative Commons license: CC Attribution-NonCommercial-NoDerivatives 4.0 https://creativecommons.org/licenses/by-nc-nd/4.0

# A Potent Interdomain-Targeting Antibody Protects against SFTSV in Mice and Non-Human Primates

## ONE SENTENCE SUMMARY

A single-dose human antibody potently neutralizes SFTSV by targeting a novel interdomain epitope, conferring robust protection in both mice and rhesus macaques, and reveals the presence of germline-encoded antibodies in human B cell repertoires.

## AUTHORS

Jinhao Bi[1,2,3,*], Ziniu Dai[1,3,*], Xiaoci Hong[1,3,*], Yuanyuan Zhang[4,5,6,7,*], Shuaiyao Lu[9,*], Qiujing Wang[8,*], Yunshu Liu[1,3], Xinyi Li[1,3], Mingxi Li[1,3], Guangyuan Song[1,3], Qing Chen[1,3], Wenhai Yu[9], Yun Yang[9], Yingqiu Ma[8], Huasheng Liu[8], Xiangzhi Meng[1,3], Zhaoqian Wang[1,3,5], Dan Liu[3,6,7], Ren Sun[1,3,5], Qiangming Sun[9,#], Shibo Li[8,#], Qiang Zhou[4,5,6,7,#], Dapeng Li[1,3,5,#]

## AFFILIATIONS

[1]Zhejiang Key Laboratory of Multi-Omics in Infection and Immunity, Center for Infectious Disease Research; [2]Affiliated Hangzhou First People's Hospital; [3]School of Medicine; [4]Zhejiang Key Laboratory of Structural Biology; [5]School of Life Sciences, Westlake University, Hangzhou, Zhejiang, 310024, China.

[6]Westlake Laboratory of Life Sciences and Biomedicine, Hangzhou, Zhejiang, 310024, China.

[7]Institute of Biology, Westlake Institute for Advanced Study, Hangzhou, Zhejiang, 310024, China.

[8]Department of Infectious Diseases, Zhoushan Hospital, Wenzhou Medical University, Zhoushan, 316000, Zhejiang, China.

[9]National Kunming High-Level Biosafety Primate Research Center, Institute of Medical Biology, Chinese Academy of Medical Sciences and Peking Union Medical College, Kunming, 650118, Yunnan, China.

Langtaosha (LTS) Preprint doi: https://doi.org/10.65215/apb7tn58 This version posted November 28, 2025. The copyright holder for this preprint (which was not certified by peer review) is the author/funder. Creative Commons license: CC Attribution-NonCommercial-NoDerivatives 4.0 https://creativecommons.org/licenses/by-nc-nd/4.0

[*]Co-first Authors

[#]Corresponding Authors. Email: Qiangming Sun qsun@imbcams.com.cn, Shibo Li lsb0398@126.com, Qiang Zhou zhouqiang@westlake.edu.cn, Dapeng Li lidapeng@westlake.edu.cn

**ABSTRACT**

Severe fever with thrombocytopenia syndrome virus (SFTSV) poses a growing global health threat with substantial mortality and no effective treatments. We report the discovery of ZS1C5, a human antibody that neutralizes SFTSV with subnanomolar potency by targeting a previously unknown interdomain epitope on glycoprotein Gn, mediated by an elongated CDRH3. A single dose of ZS1C5 conferred robust protection in both murine and, for the first time, non-human primate SFTSV infection models, demonstrating rapid viral control and immune restoration. Importantly, we applied a structure-guided mining approach to human B cell repertoires and identified germline-encoded ZS1C5-like antibodies, underscoring the potential for rapid recall of protective immunity. Together, these findings establish ZS1C5 as a promising clinical candidate and provide a blueprint for developing therapeutics and vaccines targeting interdomain epitopes in emerging bunyaviruses.

Langtaosha (LTS) Preprint doi: https://doi.org/10.65215/apb7tn58 This version posted November 28, 2025. The copyright holder for this preprint (which was not certified by peer review) is the author/funder. Creative Commons license: CC Attribution-NonCommercial-NoDerivatives 4.0 https://creativecommons.org/licenses/by-nc-nd/4.0

## MAIN TEXT

## INTRODUCTION

Severe fever with thrombocytopenia syndrome virus (SFTSV) is a tick-borne virus in the family *Phenuiviridae* of the order *Hareavirales (formerly Bunyavirales)*, causing hemorrhagic fever and thrombocytopenia. Identified in 2011 (*1*), SFTSV has rapidly spread across Asia over the past decade, with mortality rates ranging from 16.2% to 30% (*2-4*). Transmission primarily occurs through tick bites, with documented cases of human-to-human transmission, and multiple animals serve as natural reservoirs (*5, 6*). Therefore, SFTSV has been listed as one of the priority pathogens with high Public Health Emergency of International Concern (PHEIC) risk by the World Health Organization (WHO). Currently, there is no effective antiviral treatment or vaccine, and treatment remains supportive. Critically ill patients require intensive care such as plasma exchange therapy (*7*), highlighting the urgent need for potent therapeutic antibodies to reduce mortality and minimize the public health burden caused by SFTSV.

The SFTSV genome consists of three negative-sense RNA segments: L, M, and S. The M segment encodes a membrane protein precursor that undergoes proteolytic maturation to produce two glycoproteins, Gn and Gc, which form heterodimers and play crucial roles in viral entry. Gn is composed by the N-terminal Gn head region and C-terminal Gn stem region. The N-terminal Gn head consists of three domains (*8*): Domain I (or Domain A (*9*)), which is fully exposed and may directly interact with host receptors; Domain II (or β-connector (*9*)), which is mainly β-Strands and forms the major interface for interacting with Gc; and Domain III (or Domain B (*9*)), which caps the fusion loops of Gc (*8, 9*). Gn heads cluster together to form a crown on top of Gc, which is a class II viral fusion protein, making Gc less accessible and only becomes accessible during the intermediate states of membrane fusion (*9*).Thus, Gn head is a more potent target for neutralizing antibodies (NAbs).

Several NAbs targeting SFTSV Gn head have been developed. MAb4-5, the first documented NAb, targets helices α6 in Domain III of Gn but has limited *in vivo* protection (*8, 10*). Ab10, a single-chain variable fragment (scFv) antibody, binds to Domain II and stem region of Gn (*11*). Mouse mAbs 40C10 and S2A5 (*12-14*), as well as human mAb SF5 and JK-2/JK-8 (*15, 16*), recognize epitopes on Gn Domain

Langtaosha (LTS) Preprint doi: https://doi.org/10.65215/apb7tn58 This version posted November 28, 2025. The copyright holder for this preprint (which was not certified by peer review) is the author/funder. Creative Commons license: CC Attribution-NonCommercial-NoDerivatives 4.0 https://creativecommons.org/licenses/by-nc-nd/4.0

I and have shown protective effects in immunodeficient mouse models. Despite these advances, our understanding of SFTSV NAb epitopes, especially those with sufficient potency for therapeutic use, remains limited. Further characterization of novel neutralizing epitopes is the key to discovering more potent NAbs and designing effective vaccines. Additionally, it is crucial to test therapeutic NAbs in immunocompetent animal models, particularly non-human primates (NHPs), where SFTSV infection closely mimics human infection (*17*).

In the present study, we identified a human NAb ZS1C5 that neutralizes SFTSV with a subnanomolar neutralization titer. Structural analysis revealed that ZS1C5 recognizes a novel interdomain epitope that spans Domain I and Domain III of Gn head. A single dose of ZS1C5 demonstrated robust protection in immunodeficient mice against lethal SFTSV challenge and in rhesus macaques, reducing viremia and tissue viral RNA load while suppressing hyperinflammation and preserving immune homeostasis, as shown by transcriptomic profiling. Using the structural insight, computational BCR mining uncovered ZS1C5-like antibodies within the human repertoire capable of neutralizing SFTSV. These findings highlight the therapeutic potential of ZS1C5 and provide insights to inform SFTSV vaccine design.

## RESULTS

### Characterization of SFTSV Glycoprotein Gn/Gc-reactive BCRs from Convalescent Donors

To select convalescent donors for NAbs isolation, we obtained plasma samples from individuals who had suffered symptomatic laboratory-confirmed SFTSV infection during both acute ($n$=12) and convalescent ($n$=9) phases. We screened these samples for SFTSV-reactive antibody binding activities (***Fig. S1A***) and neutralization against authentic SFTSV (***Fig. 1A***). Based on these results, five donors were selected for the subsequential NAbs isolation steps, in which peripheral blood mononuclear cells (PBMCs) collected in the convalescent phase were antigen-specific sorted for single-cell PCR or single-cell BCR seqencing (***Fig. 1B-C***).

Langtaosha (LTS) Preprint doi: https://doi.org/10.65215/apb7tn58 This version posted November 28, 2025. The copyright holder for this preprint (which was not certified by peer review) is the author/funder. Creative Commons license: CC Attribution-NonCommercial-NoDerivatives 4.0 https://creativecommons.org/licenses/by-nc-nd/4.0

Transcriptomic analysis indicated that the SFTSV Gn/Gc-specific, $IgM^-/IgD^-$ B cells were mostly a cluster of cells that fell into the memory B cell subset (***Fig. 1C and S1B-E***). To characterize the gene usage of the antigen-specific BCRs, we analyzed all the Gn/Gc-specific B cells with paired heavy and light chain sequences (*n*=2,678) and compared with a reference human antibody repertoire (*18*). Over 16% of the heavy chain variable region ($V_H$) genes were VH3-33 in Gn/Gc-specific BCRs, whereas only 2.4% of reference B cells using VH3-33 (***Fig. 1D***). Light-chain variable regions ($V_\kappa/V_\lambda$) of the Gn/Gc-specific BCRs were not skewed (***Fig. 1D***). Importantly, Gn/Gc-specific BCRs showed a trend to have longer heavy-chain complementarity determining region 3 (CDRH3) lengths than reference antibodies, particularly ultra-long CDRH3 exceeding 24 amino acid (aa) in length, while no difference was observed for light-chain complementarity determining region 3 (CDRL3) (***Fig. 1E-F***). Next, we compared the Gn/Gc-specific BCRs with a reference human antibody repertoire containing both naïve and antigen-experienced antibodies (*19*). Both $V_H$ and $V_\kappa/V_\lambda$ genes exhibited antigen-experienced features, with averavge somatic hyper-mutation rates (SHM%) of 3.2% and 2.1%, respectively (***Fig. 1G***). Thus, SFTSV Gn/Gc-specific BCRs were derived from memory B cells, displayed skewed $V_H$ gene usage, and had long CDRH3.

**Identification of SFTSV-Specific Antibody Clonotypes in PBMC and Lymph Node**

To understand how SFTSV Gn/Gc-specific B cell clones expand after SFTSV infection, we performed single-cell and bulk BCR sequencing on PBMCs collected from five convalescent donors during both acute and convalescent phases (***Fig. 2A***). After clonal normalization based on heavy-chain genes, we obtained a non-antigen specific BCR repertoire with 84,025 clonotypes (***Fig. 2B***). For each donor, we identified shared clones present in both acute and convalescent stages, as well as clonotypes with highly mutated (SHM%>10%) VH genes (***Fig. 2B***), indicating these clones could develope from the early infection phase to the convalescent phase. The SFTSV Gn/Gc antigen-specific BCR pairs obtained from the previous FACS experiment (***Fig. 1B-C***) consisted of 2,451 clonotypes, including 314 clonotypes that were also observed in the non-specific BCR repertoire during both acute and convalescent phases

Langtaosha (LTS) Preprint doi: https://doi.org/10.65215/apb7tn58 This version posted November 28, 2025. The copyright holder for this preprint (which was not certified by peer review) is the author/funder. Creative Commons license: CC Attribution-NonCommercial-NoDerivatives 4.0 https://creativecommons.org/licenses/by-nc-nd/4.0

(***Fig. 2B and S1F***). To further validate the BCR specificities, out of these 2,451 clonotypes, we synthesized selected BCR pairs with certain criteria (HCDR3 length>17 aa and SHM% of VH>6%; or with differentially mutated BCRs in one clonotype) to generate recombinant IgG antibodies. After SFTSV Gn/Gc ELISA binding screening, we discovered 25 Gn-specific and 24 Gc-specific antibodies, some of which belongs to clonotypes that expanded across both acute and convalescent phases (***Fig. 2C***). Notably, we observed IgM and IgG with high VH mutation rates (>5%) in the acute phase (***Fig. 2C and Table S1***), which may suggest previous SFTSV exposure history.

To track BCR clonal dynamics induced by SFTSV infection in different locations, we obtained a submandibular lymph node (LN) from one hospitalized patient during acute SFTSV infection, sequenced and performed clonal analysis together with peripheral B cells collected in both acute and convalescent phases (***Fig. 2D***). Among the 151 BCR clonotypes identified from this donor, 131/151 were composed of B cell clones from different stages, and 120/151 contain at least one BCR from the LN (***Fig. S1G***). We expressed selected LN BCRs as recombinant IgGs and found two representative SFTSV Gn-specific clonotypes, Clone 29124 and Clone 77209. While the unmuated ancestor 29124-germline (29124-GL) antibody failed to bind Gn, the LN-derived antibody 29124-1 and PBMC-derived antibody 29124-2 equivalently bound to Gn in ELISA, despite being from different stages of infection and exhibiting different VH mutation rates (***Fig. 2E and S1H***). In Clone 77209, the LN-derived antibody 77209-1 was an unmuated germline antibody with no binding activity to Gn. However, antibody 77209-2 from the convalescent phase underwent SHM and acquired mutations essential for recognizing Gn (***Fig. 2E and S1H***). These clonal analysis data, together with the identification of Gn/Gc-binding antibodies, indicated that some SFTSV-reactive B cells may already exist and were rapidly recalled and expanded upon infection.

**Isolation of SFTSV Neutralizing Antibodies from Convalescent Donors**

Among the Gn/Gc-reactive recombinant IgG antibodies identified by ELISA (***Table S1***), we evaluated antibody affinity using bio-layer interferometry (BLI) and screened for NAbs against authentic

Langtaosha (LTS) Preprint doi: https://doi.org/10.65215/apb7tn58 This version posted November 28, 2025. The copyright holder for this preprint (which was not certified by peer review) is the author/funder. Creative Commons license: CC Attribution-NonCommercial-NoDerivatives 4.0 https://creativecommons.org/licenses/by-nc-nd/4.0

147 SFTSV. Of the 25 Gn-reactive antibodies, eight demonstrated potent neutralization with $IC_{50}$ values
148 below 1 μg/mL. In contrast, Gc-reactive antibodies exhibited weaker neutralization, with only one potent
149 neutralizer ($IC_{50}$ <1 μg/mL) and eight weak neutralizers (20 μg/mL<$IC_{50}$<1 μg/mL) (***Fig. 3A-B and S2A-***
150 ***D***). Notably, we identified an ultrapotent Gn-targeting neutralizing antibody, ZS1C5, which displayed
151 exceptionally high neutralizing efficacy against SFTSV, with an $IC_{50}$ of 0.3 ng/mL (***Fig. 3B and S2C***).
152 Furthermore, sequence analysis revealed a high somatic hypermutation (SHM) rate in ZS1C5 VH region
153 (SHM%=8.2%, ***Table S1***), indicating that ZS1C5 underwent extensive affinity maturation during B-cell
154 development.

155 To determine whether these NAbs recognize overlapping epitopes and thus compete for binding,
156 competitive binding assays were performed using BLI. The Gn-targeting NAbs were segregated into three
157 distinct clusters based on their ability to mutually block binding (***Fig. 3C and S2E***). ZS1C5 was grouped
158 into Gn Cluster I and demonstrated cross-blocking activity against five other potent Gn-targeting NAbs,
159 whose neutralization $IC_{50}$ values ranged from 0.037 to 0.257 μg/mL. In contrast, antibodies that did not
160 cross-block Cluster I exhibited relatively lower neutralization titers and were classified into Clusters II
161 and III. Unlike Gn NAbs, Gc-targeting NAbs showed weaker cross-competition, segregating into six
162 distinct clusters (***Fig. 3C and S2F***). Taken together, these findings indicate the presence of multiple
163 neutralizing epitopes on SFTSV Gn and Gc, with ZS1C5 emerging as an exceptionally potent antibody
164 warranting further structural analysis and *in vivo* experimental studies.
165

166 **Cyro-EM Structure Revealed a Novel Neutralization Epitope Spanning Domain I and Domain III**
167 **of Gn**

168 To elucidate the structural basis of the potent neutralizing activity of ZS1C5, we determined the cryo-
169 electron microscopy (cryo-EM) structure of the ZS1C5/SFTSV Gn complex at a resolution of 2.99 Å
170 (***Fig. 4A, S3 and Table S2***). The refined structure reveals that the ZS1C5 heavy chain occupies a groove
171 formed between Domain I (residues 20-175) and Domain III (residues 249-311) of Gn (***Fig. 4A and***
172 ***S6A***). Binding is predominantly mediated by the CDRH3 of ZS1C5, which forms multiple interactions

Langtaosha (LTS) Preprint doi: https://doi.org/10.65215/apb7tn58 This version posted November 28, 2025. The copyright holder for this preprint (which was not certified by peer review) is the author/funder. Creative Commons license: CC Attribution-NonCommercial-NoDerivatives 4.0 https://creativecommons.org/licenses/by-nc-nd/4.0

with Gn. Specifically, residues E104 and R116 of CDRH3 form salt bridges with K260 and E268 of Gn (***Fig. 4B***), while Y107, Y109, and Y114 form hydrogen bonds with R53 and E46 of Gn (***Fig. 4C***). Additionally, Y107 and Y114 engage in hydrophobic interactions with P39, L41, L42, and I55 of Gn (***Fig. 4D***). Importantly, Y114 also interacts with the N-linked glycosylation site at N63 of Gn through hydrophobic contact with the glycans (***Fig. 4D***).

The epitope targeted by ZS1C5, as defined by the antibody footprint on the Gn surface, spans 18 residues across Domain I and Domain III, with a total buried surface area of 742.7 Å$^2$ (***Fig. 4E***). Conservation analysis of all known SFTSV variants from GenBank, including genotypes C1–4 and J (***Fig. 4F***), shows that this interdomain epitope is highly conserved (***Fig. 4G***), underscoring ZS1C5's broad-spectrum neutralizing potential. Comparative epitope mapping against previously characterized NAbs (MAb4-5(*8, 10*), 40C10(*13, 14*), S2A5(*12*), and SF5 (*15*)) revealed distinct targeting patterns. Unlike MAb4-5, which exclusively binds to Domain III, or 40C10/S2A5/SF5, which target Domain I, ZS1C5 defines a unique class of NAbs that recognize a conformational epitope spanning both Domain I and Domain III (***Fig. 4H and S3E-F***). Notably, ZS1C5 possesses an elongated CDRH3 loop (23 aa), suggesting that its extended structure facilitates access to this inter-domain epitope.

To further explore binding modes within the same NAb cluster (***Fig. 3C***), we resolved the cryo-EM structures of Gn in complex with two competing NAbs, ZS336 (3.03 Å resolution) and ZS65 (3.50 Å resolution) (***Fig. 4I-J, S4, S5 and Table S2***). While ZS1C5 binding is predominantly mediated by CDRH3 interactions, both ZS336 and ZS65 utilize additional heavy chain CDRs, as well as light chain residues, for Gn recognition (***Fig. S6B-C***). ZS336 establishes an extensive polar network through interactions involving 10 heavy chain residues (T31, V56, S57, T58, Y103, Y105, D106, S107, S108, V109) and 2 light chain residues (D1, Q27), with hydrogen bonding to Gn glycosylation sites N33 and N63 (***Fig. S6D-F***). Structural π-π stacking interactions are observed between ZS336 light chain Y94, heavy chain H110, and Gn P39 (***Fig. S6F***). In contrast, ZS65 exhibits enhanced hydrophobic complementarity, involving heavy chain residues I54, F55, W104, A105, I109 and Gn residues A27, P29, I30, H31, I55, and Y70, along with polar interactions mediated by seven heavy chain residues (S28, S30,

Langtaosha (LTS) Preprint doi: https://doi.org/10.65215/apb7tn58 This version posted November 28, 2025. The copyright holder for this preprint (which was not certified by peer review) is the author/funder. Creative Commons license: CC Attribution-NonCommercial-NoDerivatives 4.0 https://creativecommons.org/licenses/by-nc-nd/4.0

Y32, R65, S102, A106, D108) and one light chain residue (S98) (***Fig. S6G-I***). Epitope comparison identifies seven conserved contact residues (P39, L41, Q50, R53, K260, T263, and A301) shared among ZS1C5, ZS336, and ZS65 (***Fig. 4K***). Despite minor variations, ZS336 and ZS65 adopt binding angles similar to ZS1C5, resulting in buried surface areas of 979.82 Å² (ZS336) and 914.67 Å² (ZS65) (***Fig. S6J-K***).

Notably, neither ZS336 nor ZS65 exhibited neutralizing potency comparable to that of ZS1C5, highlighting the distinct functional properties of the ZS1C5 epitope. In comparison to ZS336 and ZS65, ZS1C5 possesses the longest CDRH3 loop and forms a more stable complex with the Gn head, as indicated by lower energies calculated using both FoldX and Rosetta (***Fig. 4L***). These computational results suggest that ZS1C5 engages Gn with higher stability than ZS336 and ZS65. To explore the functional relevance of ZS1C5 binding, we modeled its interactions within the context of Gn-Gc heterodimers on the surface of the SFTSV virion (*9*). Our analysis revealed that ZS1C5 binds efficiently to Gn in both hexon and penton configurations without inducing steric hindrance (***Fig. 4M***). This structural versatility, together with the ability to target an interdomain neutralization epitope and the presence of a long CDRH3 region, likely contributes to the superior neutralization potency of ZS1C5.

**ZS1C5 Confers Robust Therapeutic Protection in a Lethal SFTSV Murine Model**

To assess the therapeutic efficacy of ZS1C5, we employed a lethal SFTSV infection model in STAT1$^{-/-}$ mice. A single intraperitoneal administration of ZS1C5 at 24 hours post-SFTSV-infection demonstrated dose-dependent protection: high (500 μg) and medium (50 μg) doses achieved 100% survival, while the low-dose regimen (5 μg) resulted in 60% survival (***Fig. 5A-B***). Body weight dynamics inversely correlated with antibody dosage, with full recovery observed in the high-dose group (***Fig. 5B***). In contrast, the control IgG and reference NAb MAb4-5 exhibited no protective efficacy, exhibiting rapid weight loss and 80%-100% mortality (***Fig. 5C***). Histopathological evaluation by haematoxylin and eosin (H&E) staining and immunochemistry (IHC) staining demonstrated that a single ZS1C5 administration profoundly mitigated SFTSV-induced pathology. Control animals displayed extensive splenic necrosis

Langtaosha (LTS) Preprint doi: https://doi.org/10.65215/apb7tn58 This version posted November 28, 2025. The copyright holder for this preprint (which was not certified by peer review) is the author/funder. Creative Commons license: CC Attribution-NonCommercial-NoDerivatives 4.0 https://creativecommons.org/licenses/by-nc-nd/4.0

(***Fig. 5D***) and elevated viral antigen burden, as evidenced by SFTSV nucleoprotein (NP) expression (***Fig. 5E***). In contrast, ZS1C5-treated mice displayed significantly reduced histopathology scores in spleen, liver, lung, and kidney (***Fig. 5D, 5F and S7A-B***), with near-physiological tissue architecture. IHC analysis revealed dose-dependent suppression of viral replication. High-dose ZS1C5 treatment (500 μg) resulted in near-undetectable viral antigen expression across all examined organs, while medium (50 μg) and low (5 μg) doses achieved statistically significant reductions in viral antigen burden compared to control IgG (***Fig. 5E, 5G and S7A-B***). These findings correlate with the dose-dependent survival outcomes (***Fig. 5B-C***), confirming that ZS1C5 effectively restricts viral replication and limits end-organ damage.

To delineate the therapeutic window, a single 500 μg dose of ZS1C5 was administered at 48, 72, or 96 hours post-infection (***Fig. 5H***). Treatment at 48 hours post-infection maintained 100% survival (***Fig. 5I***) and reduced viral antigen to undetectable levels, with significantly less severe SFTSV-induced tissue damage compared to the control antibody group (***Fig. 5J-K and S7C***). In contrast, only 4/10 and 1/10 mice in each group survived when receiving ZS1C5 treatment at 72 and 96 hours post-infection, respectively (***Fig. 5I***). Late treatment at 72 and 96 hours also showed less effectiveness in preventing SFTSV viral antigen expression and histopathological alterations across multiple organs (***Fig. 5J-K and S7C***). These results demonstrated that a single therapeutic dose of ZS1C5, when delivered within 48 hours-post infection, confers complete protection against lethal SFTSV challenge.

**ZS1C5 Protected Rhesus Macaques from SFTSV-Induced Symptoms**

To further evaluate ZS1C5 in a model closely resembling human physiology,, we performed *in vivo* protection study in rhesus macaques (*Macaca mulatta*), which exhibit symptoms of mild SFTSV infection similar to those in humans (*17, 20*). Macaques ($n$=4 per group) were subcutaneously challenged with $10^7$ PFU SFTSV and intravenously administered a single dose of ZS1C5 (30 mg/kg) or control mAb within 6 hours post-infection (***Fig. 6A***). Serum neutralization titers ($NT_{50}$) in ZS1C5-treated animals reached 1,152 on Day 1 and remained high levels ($NT_{50}$=512) at Day 7, whereas no neutralization activity was observed

Langtaosha (LTS) Preprint doi: https://doi.org/10.65215/apb7tn58 This version posted November 28, 2025. The copyright holder for this preprint (which was not certified by peer review) is the author/funder. Creative Commons license: CC Attribution-NonCommercial-NoDerivatives 4.0 https://creativecommons.org/licenses/by-nc-nd/4.0

in the control mAb group (***Fig. 6B***). Clinical monitoring revealed marked differences between the two groups: all the four macaques in the control mAb group developed lethargy and anorexia within two days, with two subjects experiencing severe complications such as limb stiffness or diarrhea lasting over three days. Conversely, ZS1C5-treated animals showed only transient mild anorexia on Day 2 post-infection (***Fig. 6C and Table S3***). Both groups displayed comparable low-grade fevers two days after SFTSV challenge, with no significant differences in body weight or temperature trajectories (***Fig. S8A and Table S3***).

Complete blood count (CBC) tests showed that ZS1C5 reversed SFTSV-induced thrombocytopenia, restoring platelet counts (PLT) and plateletcrit (PCT) to normal ranges, significantly higher than those in the control mAb group (***Fig. 6D and S8B; Table S3***). Coagulation dysfunction, evidenced by prolonged activated partial thromboplastin time (APTT), was observed exclusively in the control mAb group (***Fig. 6E and S8C; Table S3***). Additionally, comprehensive metabolic panel (CMP) tests revealed dramatically elevated ferritin levels in control monkeys, peaking on Day 6 post-infection and resulting in higher blood iron levels (***Fig. S8D and Table S3***). We also noted a sharp decline in blood calcium levels in SFTSV-infected monkeys, which returned to normal in the ZS1C5 group but remained low in the control mAb group (***Fig. S8D and Table S3***). Therefore, ZS1C5 antibody treatment alleviated a series of symptoms caused by SFTSV infection.

**ZS1C5 Treatment Suppressed SFTSV Viremia and Tissue Viral Replication**

To evaluate viral replication dynamics across groups, SFTSV genomic RNA levels were quantified in serum and tissues. In the control mAb-treated animals, severe viremia was observed, with average serum viral loads reaching $1.14\times10^{6}$ copies/mL on Day 1 post-infection, progressively increasing to a peak of $1.06\times10^{8}$ copies/mL by Day 5. In contrast, ZS1C5 treatment significantly reduced serum viral RNA levels by ~ 90% (averaging $1.27\times10^{5}$ copies/mL) on Day 1 and reached undetectable levels (<500 copies/mL) in all the four monkeys by Day 3 (***Fig. 6F***). At necropsy (Day 7), control mAb-treated animals exhibited extensive tissue viral replication, with the highest viral RNA loads detected in

Langtaosha (LTS) Preprint doi: https://doi.org/10.65215/apb7tn58 This version posted November 28, 2025. The copyright holder for this preprint (which was not certified by peer review) is the author/funder. Creative Commons license: CC Attribution-NonCommercial-NoDerivatives 4.0 https://creativecommons.org/licenses/by-nc-nd/4.0

lymphoid and gastrointestinal tissues, including the spleen ($5.6\times10^9$ copies/g), axillary lymph nodes (LNs; $1.7\times10^9$ copies/g), inguinal LNs ($2.1\times10^8$ copies/g), rectum ($4.3\times10^7$ copies/g), and duodenum ($3.7\times10^6$ copies/g). ZS1C5 treatment markedly suppressed viral replication across all organs, reducing RNA levels to undetectable ranges in the lung, liver, duodenum, and rectum, while achieving statistically significant reductions in the heart, kidney, pancreas, spleen, and inguinal lymph nodes (***Fig. 6G***).

Although H&E staining showed no obvious tissue histopathological changes on Day 7 (***Fig. S8E***), IHC analysis of SFTSV NP expression revealed ubiquitous antigen presence in tissues from the control mAb group. In contrast, ZS1C5 treatment nearly abolished antigen presence. Quantitative comparisons demonstrated significant reductions in viral antigen levels in the lung, heart, kidney, duodenum, rectum, and spleen (***Fig. 6H-I***). In tissues such as the brain, liver, pancreas, and inguinal lymph nodes, inter-group differences in antigen levels did not reach statistical significance, consistent with the baseline inherently low viral antigen expression in these tissues (***Fig. 6I and S8F***). These data collectively demonstrate that a single-dose ZS1C5 treatment rapidly eliminates circulating virus and potently suppresses tissue-specific viral replication.

**Single-Cell Transcriptomic Profiling Reveals ZS1C5 Treatment Restores Immune Homeostasis and Reduces Inflammation**

To elucidate how ZS1C5 treatment modulates systemic immunity during SFTSV infection, we performed single-cell RNA sequencing (scRNA-seq) on spleen cells and PBMCs from macaques at necropsy (Day 7 post-infection). Unsupervised clustering and comparative analysis revealed profound differences in immune cell composition and transcriptional programs between the ZS1C5 and control mAb groups (***Fig. S9A-C***). Control animals exhibited pronounced expansion of plasmablasts and plasma cells (PB/PC) in both spleen and PBMCs (***Fig. 7A-B***), likely a consequence of uncontrolled viral replication. While spleen germinal center (GC) B cells showed a decreasing trend in control animals ($p$=0.057), ZS1C5 treatment preserved GC B cell populations, implying that ZS1C5 may mitigate SFTSV-associated lymphoid follicle disruption (*21, 22*). Cellular immunity also exhibited significant

Langtaosha (LTS) Preprint doi: https://doi.org/10.65215/apb7tn58 This version posted November 28, 2025. The copyright holder for this preprint (which was not certified by peer review) is the author/funder. Creative Commons license: CC Attribution-NonCommercial-NoDerivatives 4.0 https://creativecommons.org/licenses/by-nc-nd/4.0

differences between groups: compared to ZS1C5-treated animals, control animals showed elevated levels of effector CD8+ T cells (CD8+ Teff) in both spleen and PBMCs (***Fig. 7C-D***) and higher cytotoxicity scores in CD8+ Teff, tissue-resident memory T cells (Ttrm), NK cells, and NKT cells (***Fig. 7E-F and Table S4***), indicative of hyperactivated cytotoxic profiles associated with prolonged viremia and tissue damage.

ZS1C5 treatment influenced megakaryocytes, which play essential roles in thrombopoiesis and immune regulation. While megakaryocyte numbers exhibited a decreasing trend in control animals (not statistically significant, ***Fig. S10A***), Gene Set Variation Analysis (GSVA) revealed enrichment of antiviral immune response pathways in megakaryocytes from the control group (***Fig. S10B***). These megakaryocytes predominantly functioned as signal senders to other immune cells while receiving weaker signals. In contrast, megakaryocytes from ZS1C5-treated animals primarily acted as signal receivers (***Fig. S10C-D***).

Monocytes, a key immune cell type targeted by SFTSV, exhibited distinct transcriptional profiles between treatment groups. While no significant difference was observed in intermediate monocyte ($CD14^+CD16^+$) levels (***Fig. S11A-B***), which are associated with unresolved inflammation in SFTSV-infected patients (*23*), Gene Set Variation Analysis (GSVA) showed that monocytes from ZS1C5-treated macaques were enriched in negative regulators of inflammation, suggesting suppression of inflammatory responses (***Fig. 7G***). Consistently, these monocytes displayed significantly higher anti-inflammatory transcript signature scores, along with reduced apoptosis and interferon-stimulated gene (ISG) scores (***Fig. 7H and Table S4***). ZS1C5 treatment also altered cell-cell interaction signals in key pathways, including IL1, TNF, TGFB, and IL2, across monocytes, dendritic cells (DCs), and macrophages, further indicating suppression of hyperinflammatory states (***Fig. S11C-J***). Serum cytokine profiling corroborated these findings: control animals exhibited sustained elevations of IFN-γ and IL-1RA, whereas ZS1C5-treated animals restored cytokine levels by Day 3 post-infection. Control animals also displayed dysregulated inflammatory cytokine expression, including suppressed TGF-α, elevated IL-2, and increased levels of Th17-associated cytokines (IL-17α and IL-23) (***Fig. 7I and Table S3***). Collectively,

Langtaosha (LTS) Preprint doi: https://doi.org/10.65215/apb7tn58 This version posted November 28, 2025. The copyright holder for this preprint (which was not certified by peer review) is the author/funder. Creative Commons license: CC Attribution-NonCommercial-NoDerivatives 4.0 https://creativecommons.org/licenses/by-nc-nd/4.0

scRNA-seq and cytokine profiling demonstrated that ZS1C5 treatment effectively restored immune homeostasis, suppressed infection-driven hyperinflammation, and preserved critical lymphoid and myeloid interactions during SFTSV infection.

**Computation-Assisted Identification of ZS1C5-like NAbs from Human BCR Repertoire**

Potent NAbs such as ZS1C5 were rare in humans but critical for protection against SFTSV infection. Based on the ZS1C5/Gn structure, we sought to determine if ZS1C5-like antibodies are present in human B cell repertoire and if these antibodies have Gn-binding and SFTSV neutralization functions similar to those of ZS1C5. To systematically identify structural homologs of the inter-domain epitope-targeting antibody ZS1C5, we established a multi-step computational mining pipeline combining sequence analysis, structural modeling, and functional validation (***Fig. 8A***). From the dataset of 87,600 antibody clonotypes established in this study by single-cell and bulk RNA-seq (***Fig. 2A***), we prioritized candidates based on genetic signatures—specifically, IGHV3-15/IGHJ4 pairing and CDRH3 lengths of 17 residues or more—reducing the pool to 121 antibodies, a manageable set for detailed computational prediction. We then implemented a scoring system incorporating nine distinct metrics, including AlphaFold2 (AF2) and RoseTTAFold2 (RF2), to rank these candidates by their structural similarity to ZS1C5. The normalized average scores generated a comprehensive ranking of the 121 antibodies (***Fig. 8B and Table S1***).

To evaluate the functional relevance of our computational approach, we synthesized, expressed, and tested the top 30 ranked antibodies for SFTSV Gn binding by ELISA. Their binding activities showed a significant correlation with the computational scores ($p = 0.0082$) (***Fig. 8C***). Notably, two of these 30 antibodies demonstrated SFTSV neutralizing activity ($IC_{50}$ = 2.9 and 2.8 μg/mL, respectively) (***Fig. 8D***). These two NAbs, Ab12842 and Ab38988, ranked 1$^{st}$ and 5$^{th}$ among all 121 candidates (***Fig. 8B***), demonstrating the reliability of our computational scoring system. These results confirm the effectiveness of our structure-guided computational pipeline for high-throughput discovery of epitope-specific NAbs.

Langtaosha (LTS) Preprint doi: https://doi.org/10.65215/apb7tn58 This version posted November 28, 2025. The copyright holder for this preprint (which was not certified by peer review) is the author/funder. Creative Commons license: CC Attribution-NonCommercial-NoDerivatives 4.0 https://creativecommons.org/licenses/by-nc-nd/4.0

Remarkably, the Ab12842 heavy chain is a fully germline-encoded IgM, lacking mutations in the variable ($V_H$) and joining ($J_H$) regions, suggesting the presence of ZS1C5-like germline or precursor antibodies capable of SFTSV neutralization. To further investigate this, we mined BCR repertoires from single-cell RNA-seq data of six healthy individuals from the UK (*24*), who are highly unlikely to have been exposed to SFTSV. Applying the same genetic filters (IGHV3-15/IGHJ4 pairing and CDRH3 ≥17 residues) and restricting to IgM/IgD antibodies with 0% VH or JH mutations (***Fig. 8E***), we identified 33 candidates from a total of 83,835 heavy chain clonotypes for subsequent synthesis and validation (***Table S1***). Among these 33 germline candidates, one antibody—Ab168b30, a germline-encoded IgD—demonstrated specific binding to SFTSV Gn (***Fig. 8F***) and dose-dependent neutralization of authentic SFTSV, albeit with modest potency ($IC_{50}$ = 20.8 μg/mL) (***Fig. 8G***). The identification of germline-encoded IgM/IgD antibodies with SFTSV-neutralizing activity (***Fig. 8H***) indicates that the human antibody repertoire contains precursors capable of neutralizing SFTSV prior to somatic hypermutation, highlighting the feasibility of eliciting such antibodies through vaccination.

## DISCUSSION

The development of effective therapeutics against SFTSV remains an urgent global health priority, given the high mortality rate, lack of approved treatments, and expanding geographic reach. This study identifies ZS1C5, a human NAb with subnanomolar potency, which recognizes a novel conformational epitope spanning Gn Domains I and III. Beyond *in vitro* ultrapotency, ZS1C5 demonstrated *in vivo* efficacy, achieving 100% survival in immunodeficient mice and mitigating viremia, thrombocytopenia, and tissue damage in rhesus macaques. Transcriptomic profiling further revealed its capacity to dampen hyperinflammation and restore immune homeostasis. Structural insights from ZS1C5 facilitated the computational identification of germline-encoded neutralizing antibodies, highlighting its dual role as a therapeutic candidate and as a foundation for rational vaccine design.

ZS1C5 employs a novel interdomain neutralizing mechanism, distinct from previously described antibodies that target isolated Gn domains. By simultaneously engaging Domain I, which mediates

Langtaosha (LTS) Preprint doi: https://doi.org/10.65215/apb7tn58 This version posted November 28, 2025. The copyright holder for this preprint (which was not certified by peer review) is the author/funder. Creative Commons license: CC Attribution-NonCommercial-NoDerivatives 4.0 https://creativecommons.org/licenses/by-nc-nd/4.0

receptor attachment, and Domain III, which supports Gc fusion loop activity (*8, 9*), ZS1C5 achieves ultrapotent neutralization. This mechanism is facilitated by its long 23-aa CDRH3 loop, which forms a "clamp-like" structure to bridge and disrupt the functional interplay between the two domains. This structural configuration likely disrupts viral entry through two potential mechanisms: 1) steric blockade of Domain I-mediated receptor binding and 2) disruption of Domain III interactions that are necessary for the Gn-Gc heterodimer conformational changes required for membrane targeting. In contrast, single-domain targeting antibodies such as MAb4-5(*8, 10*) (which binds Domain III) or 40C10(*13, 14*) (which binds Domain I) lack this dual-targeting capability and therefore do not exhibit the same dual mechanism of action. Nevertheless, these proposed mechanisms remain speculative and require further experimental validation. Future studies will be essential to confirm this dual-action model, including identifying SFTSV entry receptors, structurally characterizing Gn-Gc heterodimer dynamics during viral entry, and elucidating the role of Gn in the pre- to post-fusion transition.

Conservation analysis of all published SFTSV glycoprotein sequences shows that the interdomain epitope recognized by ZS1C5 is highly conserved across diverse human SFTSV variants, supporting its broad-spectrum neutralizing activity and therapeutic potential. In contrast, ZS336 and ZS65, though targeting overlapping epitopes, are less potent likely due to shorter CDRH3 loops and reliance on auxiliary light-chain interactions, restricting their inter-domain engagement. Consistent with this, computational modeling using tools such as FoldX and Rosetta indicates that ZS336 and ZS65 form less stable antigen-antibody complexes compared to ZS1C5. Additional factors, such as glycan-mediated steric hindrance (in the case of ZS336) and weaker hydrophobic complementarity (in ZS65), may further reduce their neutralization efficacy. The interdomain targeting strategy employed by ZS1C5 represents a novel paradigm for SFTSV neutralization, with promising implications for the development of pan-phlebovirus therapeutic antibodies and epitope-focused vaccines. Nonetheless, continued surveillance and further studies are important to monitor emerging mutations that could affect antibody efficacy.

Pre-existing immunity to SFTSV remains poorly understood. Our findings revealed that SFTSV-reactive B cells with high VH mutation rates and IgG subtypes were present not only during the

Langtaosha (LTS) Preprint doi: https://doi.org/10.65215/apb7tn58 This version posted November 28, 2025. The copyright holder for this preprint (which was not certified by peer review) is the author/funder. Creative Commons license: CC Attribution-NonCommercial-NoDerivatives 4.0 https://creativecommons.org/licenses/by-nc-nd/4.0

406 convalescent phase but also during acute infection. Specifically, Gn/Gc-specific BCRs with high VH
407 mutation rates (>5%) and IgG isotypes were detected in PBMCs as early as 4–7 days post-symptom
408 onset. Furthermore, analysis of submandibular LN samples from an acute-phase patient identified Gn-
409 specific antibodies, such as 29124-1, with SHM rates of 7.0% in the VH region. Given the short time
410 frame, it is highly unlikely for B cells to undergo extensive SHM and class-switch to IgG during the acute
411 phase of infection. Instead, these findings strongly suggest a rapid recall and expansion of pre-existing
412 memory B cells, possibly primed by prior, subclinical exposure to SFTSV or antigenically related
413 bunyaviruses. This is particularly evident given that four out of five convalescent donors were over 65
414 years old and had a history of tick bites.

415 In parallel, our computational identification of ZS1C5-like germline antibodies demonstrates that the
416 human antibody repertoire harbors genetic precursors with the capacity for SFTSV neutralization,
417 independent of prior antigen exposure. Germline IgM and IgD antibodies, such as Ab12842 and
418 Ab168b30, which lack VH and JH mutations, nevertheless exhibited neutralizing activity against SFTSV.
419 While this raises the possibility that the interdomain epitope may be accessible to antibodies without
420 extensive SHM, further structural studies are required to determine whether these germline antibodies
421 indeed engage the same epitope as ZS1C5. These findings have important implications for vaccine
422 design, highlighting the potential to develop immunogens that activate germline antibodies capable of
423 targeting key neutralizing epitopes. Moreover, structure-guided antibody discovery frameworks may be
424 broadly applicable for the rapid identification of therapeutic candidates against emerging viral threats.

425 The ability of ZS1C5 to confer robust protection in both murine and NHP models highlights its
426 therapeutic potential. In $STAT1^{-/-}$ mice, a single dose of ZS1C5 achieved 100% survival against lethal
427 SFTSV challenge, with dose-dependent reductions in viral antigen expression and tissue damage.
428 Histopathological analyses confirmed the capacity of ZS1C5 to suppress viral replication and mitigate
429 end-organ injury. In rhesus macaques, which exhibit mild SFTSV infection similar to humans (*17, 20*),
430 ZS1C5 significantly reduced viremia, preserved platelet counts, and alleviated coagulation dysfunction.
431 Despite the high viral dose used for infection ($5\times10^7$ $TCID_{50}$) that is vastly exceeding natural exposure

Langtaosha (LTS) Preprint doi: https://doi.org/10.65215/apb7tn58 This version posted November 28, 2025. The copyright holder for this preprint (which was not certified by peer review) is the author/funder. Creative Commons license: CC Attribution-NonCommercial-NoDerivatives 4.0 https://creativecommons.org/licenses/by-nc-nd/4.0

levels through tick bites, ZS1C5 effectively suppressed symptoms and viral loads, reducing peak viremia by 90% within 24 hours and eliminating detectable serum RNA by day 3. Importantly, the use of NHP models ensures the translational relevance of these findings, providing critical insights into the safety and efficacy of ZS1C5 in a biological context closely resembling human physiology.

Single-cell transcriptomic profiling demonstrated that ZS1C5 treatment effectively mitigates SFTSV-induced immune dysregulation, preserving immune homeostasis and restoring essential cellular functions. In alignment with patient data (*23*), uncontrolled viral replication in the control mAb-treated monkeys led to: 1) expansion of PB/PC; 2) upregulated cytotoxicity signatures in CD8+ T, NK and NKT cells; and 3) hyperactivation of monocytes, as evidenced by altered inflammatory-related signatures and inflammatory pathway cell-cell interactions. By contrast, ZS1C5 neutralized circulating virus rapidly, thereby preventing these dysregulated immune phenotypes. Specifically, ZS1C5 treatment exhibited enrichment of anti-inflammatory pathways and suppression of hyperactivated immune states, which were further validated at the protein level by Luminex assay. In addition to phenotypes paralleling severe human cases, decreased GC B cells and increased CD8+ Teff cells were observed in the control group. While intermediate monocyte expansion was noted in human studies, it was only observed in one control monkey, likely due to differences in sampling time points. Interestingly, megakaryocytes, rarely seen in peripheral blood and therefore have not been analyzed in human SFTSV cases, were observed in monkeys. Transcriptional analyses of spleen megakaryocytes revealed functional alterations linked to SFTSV-induced thrombocytopenia and coagulation dysfunction.

While this study highlights ZS1C5 as a promising therapeutic candidate, several limitations remain to be addressed. First, our stringent selection criteria during NAb discovery—requiring long CDRH3 (>17 aa) and high SHM rates (>6%)—may have inadvertently excluded potent neutralizing antibodies with shorter CDRH3 loops or lower SHM. Although ZS1C5 was identified based on these parameters, additional studies are needed to determine whether antibodies targeting other valuable neutralizing epitopes may also hold therapeutic potential. Second, the efficacy of ZS1C5 in treating late-stage infections remains unclear, as most patients seek medical care several days after symptom onset. Future

Langtaosha (LTS) Preprint doi: https://doi.org/10.65215/apb7tn58 This version posted November 28, 2025. The copyright holder for this preprint (which was not certified by peer review) is the author/funder. Creative Commons license: CC Attribution-NonCommercial-NoDerivatives 4.0 https://creativecommons.org/licenses/by-nc-nd/4.0

458 studies should focus on optimizing treatment regimens and evaluating long-term safety and efficacy in
459 clinical settings. Third, the high viral dose used in the NHP challenge model does not fully replicate
460 natural infection dynamics, where SFTSV transmission typically occurs via tick bites and involves only
461 small amounts of virus. Notably, ZS1C5 demonstrated efficacy even against high-dose viral challenges in
462 macaques, suggesting that under real-world conditions with much lower viral loads, ZS1C5 could be even
463 more effective. This enhanced effectiveness may enable a larger time window for post-exposure
464 treatment, which is critical for addressing delays in medical care often seen in SFTSV patients. Finally,
465 while the computational pipeline for identifying ZS1C5-like antibodies proved reliable, further refinement
466 is needed to improve predictive accuracy and scalability for broader applications. Despite these
467 limitations, ZS1C5 represents a significant advance in therapeutic antibody development for SFTSV. The
468 ability to target a novel interdomain epitope, combined with strong *in vivo* protective and
469 immunomodulatory effects, provides a solid foundation for clinical translation.
470
471
472 **MATERIALS AND METHODS**
473 **Study Design**
474 The primary objective of this study was to identify potent neutralizing antibodies for the therapeutic
475 treatment of SFTSV infection. Antibodies were isolated from human PBMCs. Small animal efficacy was
476 evaluated using mice, while NHPs were employed as a highly translatable model to assess clinical
477 relevance. All human sample collections and animal experiments were conducted in compliance with
478 protocols approved by the relevant Institutional Animal Care and Use Committees (IACUCs),
479 Institutional Review Board (IRB) and Biosafety Committees. Experimental group sizes were predefined
480 as 10 mice and 4 monkeys per group to ensure adequate statistical power for detecting meaningful
481 differences. Animals were selected based on availability and appropriate age criteria, and were randomly
482 allocated to experimental groups with balanced sex distribution. Blinding was implemented in the NHP
483 experiments, but not in the mouse studies. Data collection was sustained until all predefined study

Langtaosha (LTS) Preprint doi: https://doi.org/10.65215/apb7tn58 This version posted November 28, 2025. The copyright holder for this preprint (which was not certified by peer review) is the author/funder. Creative Commons license: CC Attribution-NonCommercial-NoDerivatives 4.0 https://creativecommons.org/licenses/by-nc-nd/4.0

endpoints were met. Throughout the study, animals received ad libitum access to food and water, as well as appropriate veterinary care. All animals enrolled, including any outliers, were included in the final data analyses.

Detailed methods are provided in the Supplementary Materials.

## ACKNOWLEDGMENTS

We thank the technical support from the Biomedical Research Core Facility, Laboratory Animal Resources Center and High-Performance Computing Center at Westlake University. We thank Chi Biotech Co., Ltd. for assisting in the single-cell sequencing and Manli Wang from Wuhan Institute of Virology for providing key reagents. We thank Chentong Wang and Dangsheng Li for scientific guidance and helpful discussion. This work was supported by Westlake Education Foundation (to D.Li.), Westlake Laboratory of Life Sciences and Biomedicine (grant 1010060220B1/021 to D.Li.), Zhejiang Provincial Key Laboratory Construction Project (2024ZY01026), the National Natural Science Foundation of China (82241081 to Q.Z. and 82471858 to D.L.), the Key Regional Research and Development Program (2023CSJZN0600 to Q.Z.) from Ministry of Science and Technology of China, Zhoushan Municipal Public Welfare Project (2023C31006, to Q.W.), and Zhejiang Provincial Natural Science Foundation (LY21H100002, to S.L.).

## DATA AVAILABILITY

The data and codes that support the findings of this study are available from the corresponding authors on request. The structures of ZS1C5-Gn, ZS336-Gn, ZS65-Gn were deposited to the Protein Data Bank (PDB) with accession # 9LOE, 9LOF, and 9LOG, respectively.

## AUTHOR CONTRIBUTIONS

Langtaosha (LTS) Preprint doi: https://doi.org/10.65215/apb7tn58 This version posted November 28, 2025. The copyright holder for this preprint (which was not certified by peer review) is the author/funder. Creative Commons license: CC Attribution-NonCommercial-NoDerivatives 4.0 https://creativecommons.org/licenses/by-nc-nd/4.0

509 J.B., X.H., Y.Z., S.Lu., X.L. and G.S. performed experiments. Z.D. performed computational
510 analysis. Q.W., Y.M., H.L. and S.Li. collected human specimens and provided clinical surports. Y.Z.,
511 Y.L., Z.W. and Q.Z. performed structure experiments and analysis. S.Lu., W.Y., Y.Y. and Q.S. performed
512 and supervised the NHP study. X.M., D.Liu. and R.S. provided critical scientific guidance. D.Li.
513 conceived, designed and supervised the study. B.J., Z.D., and D.Li. wrote the paper. All authors reviewed
514 and approved the manuscript.
515
516 **DECLARATION OF INTERESTS**
517 D.Li., J.B., X.H., Y.Z., Q,Z, and S.Li. have applied for patents concerning SFTSV antibodies that are
518 related to this work. All other authors declare no conflict of interest.
519
520
521 **REFERENCES AND NOTES**
522 1. X. J. Yu, M. F. Liang, S. Y. Zhang, Y. Liu, J. D. Li, Y. L. Sun, L. Zhang, Q. F. Zhang, V. L.
523 Popov, C. Li, J. Qu, Q. Li, Y. P. Zhang, R. Hai, W. Wu, Q. Wang, F. X. Zhan, X. J. Wang, B.
524 Kan, S. W. Wang, K. L. Wan, H. Q. Jing, J. X. Lu, W. W. Yin, H. Zhou, X. H. Guan, J. F. Liu, Z.
525 Q. Bi, G. H. Liu, J. Ren, H. Wang, Z. Zhao, J. D. Song, J. R. He, T. Wan, J. S. Zhang, X. P. Fu,
526 L. N. Sun, X. P. Dong, Z. J. Feng, W. Z. Yang, T. Hong, Y. Zhang, D. H. Walker, Y. Wang, D.
527 X. Li, Fever with thrombocytopenia associated with a novel bunyavirus in China. *N Engl J Med*
528 **364**, 1523-1532 (2011).
529 2. Y. Liu, Q. Li, W. Hu, J. Wu, Y. Wang, L. Mei, D. H. Walker, J. Ren, Y. Wang, X. J. Yu, Person-
530 to-person transmission of severe fever with thrombocytopenia syndrome virus. *Vector Borne*
531 *Zoonotic Dis* **12**, 156-160 (2012).
532 3. M. Wang, W. Tan, J. Li, L. Fang, M. Yue, The Endless Wars: Severe Fever With
533 Thrombocytopenia Syndrome Virus, Host Immune and Genetic Factors. *Front Cell Infect*
534 *Microbiol* **12**, 808098 (2022).

Langtaosha (LTS) Preprint doi: https://doi.org/10.65215/apb7tn58 This version posted November 28, 2025. The copyright holder for this preprint (which was not certified by peer review) is the author/funder. Creative Commons license: CC Attribution-NonCommercial-NoDerivatives 4.0 https://creativecommons.org/licenses/by-nc-nd/4.0

4. H. Li, Q. B. Lu, B. Xing, S. F. Zhang, K. Liu, J. Du, X. K. Li, N. Cui, Z. D. Yang, L. Y. Wang, J. G. Hu, W. C. Cao, W. Liu, Epidemiological and clinical features of laboratory-diagnosed severe fever with thrombocytopenia syndrome in China, 2011-17: a prospective observational study. *Lancet Infect Dis* **18**, 1127-1137 (2018).

5. H. Cui, S. Shen, L. Chen, Z. Fan, Q. Wen, Y. Xing, Z. Wang, J. Zhang, J. Chen, B. La, Y. Fang, Z. Yang, S. Yang, X. Yan, S. Pei, T. Li, X. Cui, Z. Jia, W. Cao, Global epidemiology of severe fever with thrombocytopenia syndrome virus in human and animals: a systematic review and meta-analysis. *Lancet Reg Health West Pac* **48**, 101133 (2024).

6. Z. Liu, Z. Wang, Northeastern China, a Hotspot for Tick-Borne Viral Diseases. *Zoonoses* **5**, (2025).

7. J. W. Seo, D. Kim, N. Yun, D. M. Kim, Clinical Update of Severe Fever with Thrombocytopenia Syndrome. *Viruses* **13**, (2021).

8. Y. Wu, Y. Zhu, F. Gao, Y. Jiao, B. O. Oladejo, Y. Chai, Y. Bi, S. Lu, M. Dong, C. Zhang, G. Huang, G. Wong, N. Li, Y. Zhang, Y. Li, W. H. Feng, Y. Shi, M. Liang, R. Zhang, J. Qi, G. F. Gao, Structures of phlebovirus glycoprotein Gn and identification of a neutralizing antibody epitope. *Proc Natl Acad Sci U S A* **114**, E7564-E7573 (2017).

9. S. Du, R. Peng, W. Xu, X. Qu, Y. Wang, J. Wang, L. Li, M. Tian, Y. Guan, J. Wang, G. Wang, H. Li, L. Deng, X. Shi, Y. Ma, F. Liu, M. Sun, Z. Wei, N. Jin, W. Liu, J. Qi, Q. Liu, M. Liao, C. Li, Cryo-EM structure of severe fever with thrombocytopenia syndrome virus. *Nat Commun* **14**, 6333 (2023).

10. X. Guo, L. Zhang, W. Zhang, Y. Chi, X. Zeng, X. Li, X. Qi, Q. Jin, X. Zhang, M. Huang, H. Wang, Y. Chen, C. Bao, J. Hu, S. Liang, L. Bao, T. Wu, M. Zhou, Y. Jiao, Human antibody neutralizes severe Fever with thrombocytopenia syndrome virus, an emerging hemorrhagic Fever virus. *Clin Vaccine Immunol* **20**, 1426-1432 (2013).

11. K. H. Kim, J. Kim, M. Ko, J. Y. Chun, H. Kim, S. Kim, J. Y. Min, W. B. Park, M. D. Oh, J. Chung, An anti-Gn glycoprotein antibody from a convalescent patient potently inhibits the

Langtaosha (LTS) Preprint doi: https://doi.org/10.65215/apb7tn58 This version posted November 28, 2025. The copyright holder for this preprint (which was not certified by peer review) is the author/funder. Creative Commons license: CC Attribution-NonCommercial-NoDerivatives 4.0 https://creativecommons.org/licenses/by-nc-nd/4.0

561 infection of severe fever with thrombocytopenia syndrome virus. *PLoS Pathog* **15**, e1007375
562 (2019).
563 12. X. Ren, J. Sun, W. Kuang, F. Yu, B. Wang, Y. Wang, W. Deng, Z. Xu, S. Yang, H. Wang, Y.
564 Hu, Z. Deng, Y. J. Ning, H. Zhao, A broadly protective antibody targeting glycoprotein Gn
565 inhibits severe fever with thrombocytopenia syndrome virus infection. *Nat Commun* **15**, 7009
566 (2024).
567 13. X. Wu, A. Moming, Y. Zhang, Z. Wang, T. Zhang, L. Fu, J. Qian, J. Ni, S. Hu, S. Tang, X.
568 Zheng, H. Wang, S. Shen, F. Deng, Identification and characterization of three monoclonal
569 antibodies targeting the SFTSV glycoprotein and displaying a broad spectrum recognition of
570 SFTSV-related viruses. *PLoS Negl Trop Dis* **18**, e0012216 (2024).
571 14. P. Yang, X. Wu, H. Shang, Z. Sun, Z. Wang, Z. Song, H. Yuan, F. Deng, S. Shen, Y. Guo, N.
572 Zhang, Molecular mechanism and structure-guided humanization of a broadly neutralizing
573 antibody against SFTSV. *PLoS Pathog* **20**, e1012550 (2024).
574 15. Z. Chang, D. Gao, L. Liao, J. Sun, G. Zhang, X. Zhang, F. Wang, C. Li, B. O. Oladejo, S. Li, Y.
575 Chai, Y. Hu, X. Lu, H. Xiao, J. Qi, Z. Chen, F. Gao, Y. Wu, Bispecific antibodies targeting two
576 glycoproteins on SFTSV exhibit synergistic neutralization and protection in a mouse model. *Proc*
577 *Natl Acad Sci U S A* **121**, e2400163121 (2024).
578 16. S. Zhang, H. Shang, S. Han, J. Li, X. Peng, Y. Wu, X. Yang, Y. Leng, F. Wang, N. Cui, L. Xu,
579 H. Zhang, Y. Guo, X. Xu, N. Zhang, W. Liu, H. Li, Discovery and characterization of potent
580 broadly neutralizing antibodies from human survivors of severe fever with thrombocytopenia
581 syndrome. *EBioMedicine* **111**, 105481 (2024).
582 17. Y. H. Li, W. W. Huang, W. Q. He, X. Y. He, X. H. Wang, Y. L. Lin, Z. J. Zhao, Y. T. Zheng, W.
583 Pang, Longitudinal analysis of immunocyte responses and inflammatory cytokine profiles in
584 SFTSV-infected rhesus macaques. *Front Immunol* **14**, 1143796 (2023).

Langtaosha (LTS) Preprint doi: https://doi.org/10.65215/apb7tn58 This version posted November 28, 2025. The copyright holder for this preprint (which was not certified by peer review) is the author/funder. Creative Commons license: CC Attribution-NonCommercial-NoDerivatives 4.0 https://creativecommons.org/licenses/by-nc-nd/4.0

18. B. J. DeKosky, T. Kojima, A. Rodin, W. Charab, G. C. Ippolito, A. D. Ellington, G. Georgiou, In-depth determination and analysis of the human paired heavy- and light-chain antibody repertoire. *Nat Med* **21**, 86-91 (2015).

19. B. J. DeKosky, O. I. Lungu, D. Park, E. L. Johnson, W. Charab, C. Chrysostomou, D. Kuroda, A. D. Ellington, G. C. Ippolito, J. J. Gray, G. Georgiou, Large-scale sequence and structural comparisons of human naive and antigen-experienced antibody repertoires. *Proc Natl Acad Sci U S A* **113**, E2636-2645 (2016).

20. C. Jin, H. Jiang, M. Liang, Y. Han, W. Gu, F. Zhang, H. Zhu, W. Wu, T. Chen, C. Li, W. Zhang, Q. Zhang, J. Qu, Q. Wei, C. Qin, D. Li, SFTS virus infection in nonhuman primates. *J Infect Dis* **211**, 915-925 (2015).

21. Y. Sakai, S. Mura, Y. Kuwabara, S. Kagimoto, M. Sakurai, M. Morimoto, E. S. Park, M. Shimojima, N. Nagata, Y. Ami, T. Yoshikawa, N. Iwata-Yoshikawa, S. Fukushi, S. Watanabe, T. Kurosu, A. Okutani, M. Kimura, K. Imaoka, M. Saijo, S. Morikawa, T. Suzuki, K. Maeda, Lethal severe fever with thrombocytopenia syndrome virus infection causes systemic germinal centre failure and massive T cell apoptosis in cats. *Front Microbiol* **14**, 1333946 (2023).

22. D. Kim, C. J. Lai, I. Cha, J. U. Jung, Current Progress of Severe Fever with Thrombocytopenia Syndrome Virus (SFTSV) Vaccine Development. *Viruses* **16**, (2024).

23. H. Li, X. Li, S. Lv, X. Peng, N. Cui, T. Yang, Z. Yang, C. Yuan, Y. Yuan, J. Yao, Z. Yuan, J. Li, X. Ye, X. Zhang, S. Zhu, K. Peng, W. Liu, Single-cell landscape of peripheral immune responses to fatal SFTS. *Cell Rep* **37**, 110039 (2021).

24. K. Le Quy, M. Chernigovskaya, M. Stensland, S. Singh, J. Leem, S. Revale, D. A. Yadin, F. L. Nice, C. Povall, D. H. Minns, J. D. Galson, T. A. Nyman, I. Snapkow, V. Greiff, Benchmarking and integrating human B-cell receptor genomic and antibody proteomic profiling. *NPJ Syst Biol Appl* **10**, 73 (2024).

25. D. Li, R. J. Edwards, K. Manne, D. R. Martinez, A. Schafer, S. M. Alam, K. Wiehe, X. Lu, R. Parks, L. L. Sutherland, T. H. Oguin, 3rd, C. McDanal, L. G. Perez, K. Mansouri, S. M. C.

Langtaosha (LTS) Preprint doi: https://doi.org/10.65215/apb7tn58 This version posted November 28, 2025. The copyright holder for this preprint (which was not certified by peer review) is the author/funder. Creative Commons license: CC Attribution-NonCommercial-NoDerivatives 4.0 https://creativecommons.org/licenses/by-nc-nd/4.0

Gobeil, K. Janowska, V. Stalls, M. Kopp, F. Cai, E. Lee, A. Foulger, G. E. Hernandez, A. Sanzone, K. Tilahun, C. Jiang, L. V. Tse, K. W. Bock, M. Minai, B. M. Nagata, K. Cronin, V. Gee-Lai, M. Deyton, M. Barr, T. Von Holle, A. N. Macintyre, E. Stover, J. Feldman, B. M. Hauser, T. M. Caradonna, T. D. Scobey, W. Rountree, Y. Wang, M. A. Moody, D. W. Cain, C. T. DeMarco, T. N. Denny, C. W. Woods, E. W. Petzold, A. G. Schmidt, I. T. Teng, T. Zhou, P. D. Kwong, J. R. Mascola, B. S. Graham, I. N. Moore, R. Seder, H. Andersen, M. G. Lewis, D. C. Montefiori, G. D. Sempowski, R. S. Baric, P. Acharya, B. F. Haynes, K. O. Saunders, In vitro and in vivo functions of SARS-CoV-2 infection-enhancing and neutralizing antibodies. *Cell* **184**, 4203-4219 e4232 (2021).

26. S. Q. Zheng, E. Palovcak, J. P. Armache, K. A. Verba, Y. Cheng, D. A. Agard, MotionCor2: anisotropic correction of beam-induced motion for improved cryo-electron microscopy. *Nat Methods* **14**, 331-332 (2017).

27. T. Grant, N. Grigorieff, Measuring the optimal exposure for single particle cryo-EM using a 2.6 Å reconstruction of rotavirus VP6. *Elife* **4**, e06980 (2015).

28. K. Zhang, Gctf: Real-time CTF determination and correction. *J Struct Biol* **193**, 1-12 (2016).

29. A. Punjani, J. L. Rubinstein, D. J. Fleet, M. A. Brubaker, cryoSPARC: algorithms for rapid unsupervised cryo-EM structure determination. *Nat Methods* **14**, 290-296 (2017).

30. D. Kimanius, B. O. Forsberg, S. H. Scheres, E. Lindahl, Accelerated cryo-EM structure determination with parallelisation using GPUs in RELION-2. *Elife* **5**, (2016).

31. S. H. Scheres, A Bayesian view on cryo-EM structure determination. *J Mol Biol* **415**, 406-418 (2012).

32. S. H. Scheres, RELION: implementation of a Bayesian approach to cryo-EM structure determination. *J Struct Biol* **180**, 519-530 (2012).

33. S. H. Scheres, Semi-automated selection of cryo-EM particles in RELION-1.3. *J Struct Biol* **189**, 114-122 (2015).

Langtaosha (LTS) Preprint doi: https://doi.org/10.65215/apb7tn58 This version posted November 28, 2025. The copyright holder for this preprint (which was not certified by peer review) is the author/funder. Creative Commons license: CC Attribution-NonCommercial-NoDerivatives 4.0 https://creativecommons.org/licenses/by-nc-nd/4.0

636 34. P. B. Rosenthal, R. Henderson, Optimal determination of particle orientation, absolute hand, and
637 contrast loss in single-particle electron cryomicroscopy. *J Mol Biol* **333**, 721-745 (2003).
638 35. S. Chen, G. McMullan, A. R. Faruqi, G. N. Murshudov, J. M. Short, S. H. Scheres, R. Henderson,
639 High-resolution noise substitution to measure overfitting and validate resolution in 3D structure
640 determination by single particle electron cryomicroscopy. *Ultramicroscopy* **135**, 24-35 (2013).
641 36. J. Jumper, R. Evans, A. Pritzel, T. Green, M. Figurnov, O. Ronneberger, K. Tunyasuvunakool, R.
642 Bates, A. Zidek, A. Potapenko, A. Bridgland, C. Meyer, S. A. A. Kohl, A. J. Ballard, A. Cowie,
643 B. Romera-Paredes, S. Nikolov, R. Jain, J. Adler, T. Back, S. Petersen, D. Reiman, E. Clancy, M.
644 Zielinski, M. Steinegger, M. Pacholska, T. Berghammer, S. Bodenstein, D. Silver, O. Vinyals, A.
645 W. Senior, K. Kavukcuoglu, P. Kohli, D. Hassabis, Highly accurate protein structure prediction
646 with AlphaFold. *Nature* **596**, 583-589 (2021).
647 37. M. Varadi, S. Anyango, M. Deshpande, S. Nair, C. Natassia, G. Yordanova, D. Yuan, O. Stroe,
648 G. Wood, A. Laydon, A. Zidek, T. Green, K. Tunyasuvunakool, S. Petersen, J. Jumper, E.
649 Clancy, R. Green, A. Vora, M. Lutfi, M. Figurnov, A. Cowie, N. Hobbs, P. Kohli, G. Kleywegt,
650 E. Birney, D. Hassabis, S. Velankar, AlphaFold Protein Structure Database: massively expanding
651 the structural coverage of protein-sequence space with high-accuracy models. *Nucleic Acids Res*
652 **50**, D439-D444 (2022).
653 38. L. G. Trabuco, E. Villa, K. Mitra, J. Frank, K. Schulten, Flexible fitting of atomic structures into
654 electron microscopy maps using molecular dynamics. *Structure* **16**, 673-683 (2008).
655 39. J. F. Bruhn, R. N. Kirchdoerfer, S. M. Urata, S. Li, I. J. Tickle, G. Bricogne, E. O. Saphire,
656 Crystal Structure of the Marburg Virus VP35 Oligomerization Domain. *J. Virol.* **91**, 14 (2017).
657 40. P. D. Adams, P. V. Afonine, G. Bunkoczi, V. B. Chen, I. W. Davis, N. Echols, J. J. Headd, L. W.
658 Hung, G. J. Kapral, R. W. Grosse-Kunstleve, A. J. McCoy, N. W. Moriarty, R. Oeffner, R. J.
659 Read, D. C. Richardson, J. S. Richardson, T. C. Terwilliger, P. H. Zwart, PHENIX: a
660 comprehensive Python-based system for macromolecular structure solution. *Acta Crystallogr D*
661 *Biol Crystallogr* **66**, 213-221 (2010).

Langtaosha (LTS) Preprint doi: https://doi.org/10.65215/apb7tn58 This version posted November 28, 2025. The copyright holder for this preprint (which was not certified by peer review) is the author/funder. Creative Commons license: CC Attribution-NonCommercial-NoDerivatives 4.0 https://creativecommons.org/licenses/by-nc-nd/4.0

41. A. M. Waterhouse, J. B. Procter, D. M. Martin, M. Clamp, G. J. Barton, Jalview Version 2--a multiple sequence alignment editor and analysis workbench. *Bioinformatics* **25**, 1189-1191 (2009).

42. J. Delgado, L. G. Radusky, D. Cianferoni, L. Serrano, FoldX 5.0: working with RNA, small molecules and a new graphical interface. *Bioinformatics* **35**, 4168-4169 (2019).

43. J. K. Leman, B. D. Weitzner, S. M. Lewis, J. Adolf-Bryfogle, N. Alam, R. F. Alford, M. Aprahamian, D. Baker, K. A. Barlow, P. Barth, B. Basanta, B. J. Bender, K. Blacklock, J. Bonet, S. E. Boyken, P. Bradley, C. Bystroff, P. Conway, S. Cooper, B. E. Correia, B. Coventry, R. Das, R. M. De Jong, F. DiMaio, L. Dsilva, R. Dunbrack, A. S. Ford, B. Frenz, D. Y. Fu, C. Geniesse, L. Goldschmidt, R. Gowthaman, J. J. Gray, D. Gront, S. Guffy, S. Horowitz, P. S. Huang, T. Huber, T. M. Jacobs, J. R. Jeliazkov, D. K. Johnson, K. Kappel, J. Karanicolas, H. Khakzad, K. R. Khar, S. D. Khare, F. Khatib, A. Khramushin, I. C. King, R. Kleffner, B. Koepnick, T. Kortemme, G. Kuenze, B. Kuhlman, D. Kuroda, J. W. Labonte, J. K. Lai, G. Lapidoth, A. Leaver-Fay, S. Lindert, T. Linsky, N. London, J. H. Lubin, S. Lyskov, J. Maguire, L. Malmström, E. Marcos, O. Marcu, N. A. Marze, J. Meiler, R. Moretti, V. K. Mulligan, S. Nerli, C. Norn, S. Ó'Conchúir, N. Ollikainen, S. Ovchinnikov, M. S. Pacella, X. Pan, H. Park, R. E. Pavlovicz, M. Pethe, B. G. Pierce, K. B. Pilla, B. Raveh, P. D. Renfrew, S. S. R. Burman, A. Rubenstein, M. F. Sauer, A. Scheck, W. Schief, O. Schueler-Furman, Y. Sedan, A. M. Sevy, N. G. Sgourakis, L. Shi, J. B. Siegel, D. A. Silva, S. Smith, Y. Song, A. Stein, M. Szegedy, F. D. Teets, S. B. Thyme, R. Y. Wang, A. Watkins, L. Zimmerman, R. Bonneau, Macromolecular modeling and design in Rosetta: recent methods and frameworks. *Nat Methods* **17**, 665-680 (2020).

44. T. Hashiguchi, M. L. Fusco, Z. A. Bornholdt, J. E. Lee, A. I. Flyak, R. Matsuoka, D. Kohda, Y. Yanagi, M. Hammel, J. E. Crowe, Jr., E. O. Saphire, Structural basis for Marburg virus neutralization by a cross-reactive human antibody. *Cell* **160**, 904-912 (2015).

45. D. Pinto, M. M. Sauer, N. Czudnochowski, J. S. Low, M. A. Tortorici, M. P. Housley, J. Noack, A. C. Walls, J. E. Bowen, B. Guarino, L. E. Rosen, J. di Iulio, J. Jerak, H. Kaiser, S. Islam, S.

Langtaosha (LTS) Preprint doi: https://doi.org/10.65215/apb7tn58 This version posted November 28, 2025. The copyright holder for this preprint (which was not certified by peer review) is the author/funder. Creative Commons license: CC Attribution-NonCommercial-NoDerivatives 4.0 https://creativecommons.org/licenses/by-nc-nd/4.0

688 Jaconi, N. Sprugasci, K. Culap, R. Abdelnabi, C. Foo, L. Coelmont, I. Bartha, S. Bianchi, C.
689 Silacci-Fregni, J. Bassi, R. Marzi, E. Vetti, A. Cassotta, A. Ceschi, P. Ferrari, P. E. Cippa, O.
690 Giannini, S. Ceruti, C. Garzoni, A. Riva, F. Benigni, E. Cameroni, L. Piccoli, M. S. Pizzuto, M.
691 Smithey, D. Hong, A. Telenti, F. A. Lempp, J. Neyts, C. Havenar-Daughton, A. Lanzavecchia, F.
692 Sallusto, G. Snell, H. W. Virgin, M. Beltramello, D. Corti, D. Veesler, Broad betacoronavirus
693 neutralization by a stem helix-specific human antibody. *Science* **373**, 1109-1116 (2021).
694

Langtaosha (LTS) Preprint doi: https://doi.org/10.65215/apb7tn58 This version posted November 28, 2025. The copyright holder for this preprint (which was not certified by peer review) is the author/funder. Creative Commons license: CC Attribution-NonCommercial-NoDerivatives 4.0 https://creativecommons.org/licenses/by-nc-nd/4.0

## FIGURES

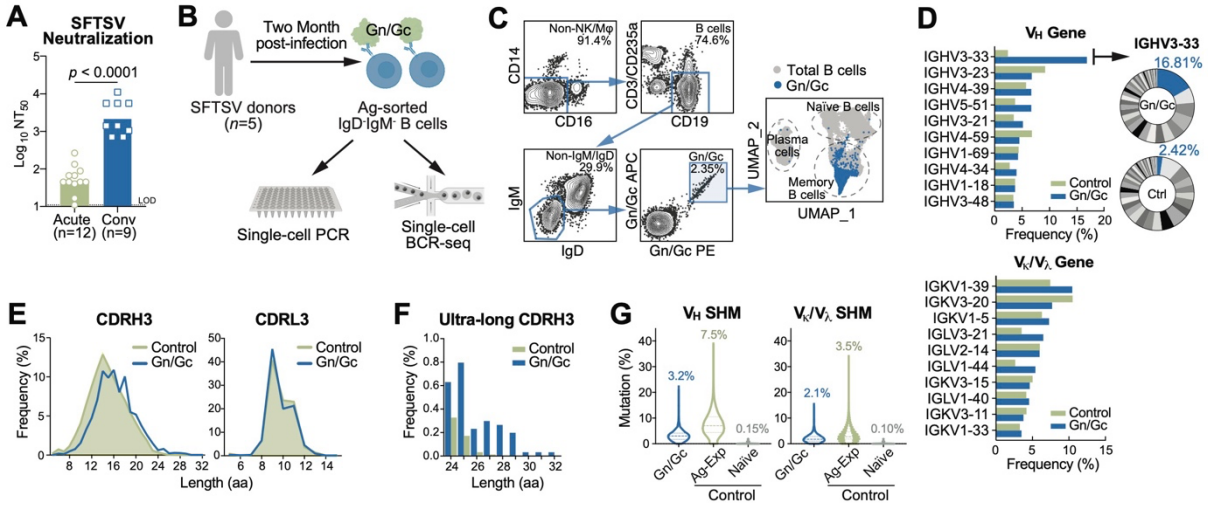


**Fig. 1. Characterization of SFTSV Glycoprotein Gn/Gc-Specific BCRs.**

**(A)** Neutralization titers of plasma samples collected from donors in SFTSV acute infection (*n*=12) and convalescent (*n*=9) phases. Bars represent geometric means of the half maximal neutralization titers ($NT_{50}$). Statistical significance was determined using Wilcoxon Rank Sum Test. LOD, limit of detection; Conv, convalescent.

**(B)** Scheme of isolating SFTSV Gn/Gc-specific antibodies. B cells were enriched from PBMCs through negative selection, and SFTSV Gn- or Gc- specific, $IgM^-IgD^-$ B cells were sorted by fluorescence-activated cell sorting (FACS) for single-cell PCR and single-cell BCR sequencing (BCR-seq).

**(C)** FACS of SFTSV Gn/Gc-specific B cells and UMAP clustering based on single-cell transcriptome.

**(D)** Gene usages of SFTSV Gn/Gc-specific BCRs illustrated in bar charts, with IGHV3-33 highlighted in pie charts. $V_H$, heavy chain variable region; Vκ, Kappa chain variable region; $V_\lambda$, lambda chain variable region. Reference repertoires (*n*=198,148) from three healthy donors (*18*) serve as controls.

**(E)** CDR3 lengths of Gn/Gc-specific BCRs. CDRH3, heavy chain CDR3; CDRL3, light chain CDR3.

Langtaosha (LTS) Preprint doi: https://doi.org/10.65215/apb7tn58 This version posted November 28, 2025. The copyright holder for this preprint (which was not certified by peer review) is the author/funder. Creative Commons license: CC Attribution-NonCommercial-NoDerivatives 4.0 https://creativecommons.org/licenses/by-nc-nd/4.0

713 **(F)** Frequency of ultra-long CDRH3 (>24 amino acids).

714 **(G)** Somatic hypermutation (SHM) rates of $V_H$ and $V_\kappa/V_\lambda$ genes in SFTSV Gn/Gc-specific BCRs in

715 violin plots, alongside reference sequences (*19*) from naïve (*n*=13,780) and antigen-experienced (Ag-Exp

716 *n*=34,692) repertoires.

717

Langtaosha (LTS) Preprint doi: https://doi.org/10.65215/apb7tn58 This version posted November 28, 2025. The copyright holder for this preprint (which was not certified by peer review) is the author/funder. Creative Commons license: CC Attribution-NonCommercial-NoDerivatives 4.0 https://creativecommons.org/licenses/by-nc-nd/4.0

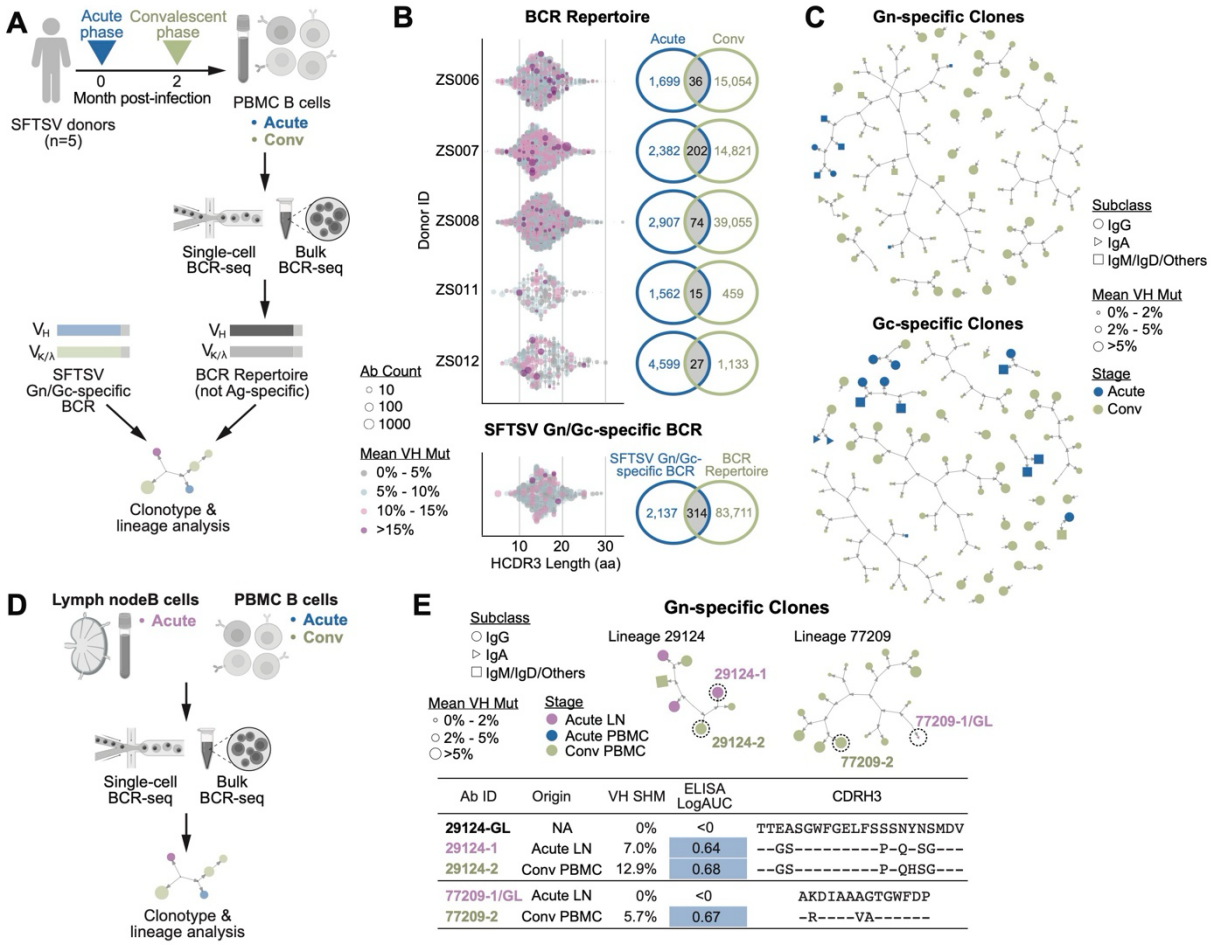


| Ab ID | Origin | VH SHM | ELISA LogAUC | CDRH3 |
|---|---|---|---|---|
| **29124-GL** | NA | 0% | <0 | TTEASGWFGELFSSSNYNSMDV |
| 29124-1 | Acute LN | 7.0% | 0.64 | --GS---------P-Q-SG--- |
| 29124-2 | Conv PBMC | 12.9% | 0.68 | --GS---------P-QHSG--- |
| 77209-1/GL | Acute LN | 0% | <0 | AKDIAAAGTGWFDP |
| 77209-2 | Conv PBMC | 5.7% | 0.67 | -R----VA------ |

**Fig. 2. Identification of SFTSV-Specific Antibody Clonotypes in PBMC and Lymph Node (LN).**

**(A)** Workflow for PBMC BCR-seq. Single-cell and bulk BCR-seq were performed during acute and convalescent phases of SFTSV infection (n=5) to generate a non-antigen-specific BCR repertoire, which was analyzed for clonotypes by VH sequences alongside SFTSV Gn/Gc-specific BCRs.

**(B)** Clonotypes of non-antigen specific and SFTSV-specific BCRs. Each dot represents one BCR clonotype, with size and color indicating count and $V_H$ mutation rate, respectively. Venn diagrams show overlap of clonotypes between acute/convalescent non-antigen-specific repertoires and between SFTSV-specific and total BCR repertoires.

**(C)** Gn/Gc-specific BCRs. Selected BCR genes were expressed as IgGs and validated by ELISA for SFTSV Gn/Gc binding. The network graph shows confirmed Gn/Gc-binding antibodies and their related clones.

Langtaosha (LTS) Preprint doi: https://doi.org/10.65215/apb7tn58 This version posted November 28, 2025. The copyright holder for this preprint (which was not certified by peer review) is the author/funder. Creative Commons license: CC Attribution-NonCommercial-NoDerivatives 4.0 https://creativecommons.org/licenses/by-nc-nd/4.0

730 **(D)** Workflow for LN BCR-seq. Single-cell and bulk BCR-seq were conducted on LN samples from
731 one donor during the acute phase, and PBMCs from the same donor during acute and convalescent
732 phases.
733 **(E)** Gn-specific clones derived from both LN and PBMC. BCRs highlighted by dashed lines were
734 expressed as IgGs and validated for Gn binding; associated antibody information is provided. GL,
735 germline; AUC, area-under-curve.
736

Langtaosha (LTS) Preprint doi: https://doi.org/10.65215/apb7tn58 This version posted November 28, 2025. The copyright holder for this preprint (which was not certified by peer review) is the author/funder. Creative Commons license: CC Attribution-NonCommercial-NoDerivatives 4.0 https://creativecommons.org/licenses/by-nc-nd/4.0

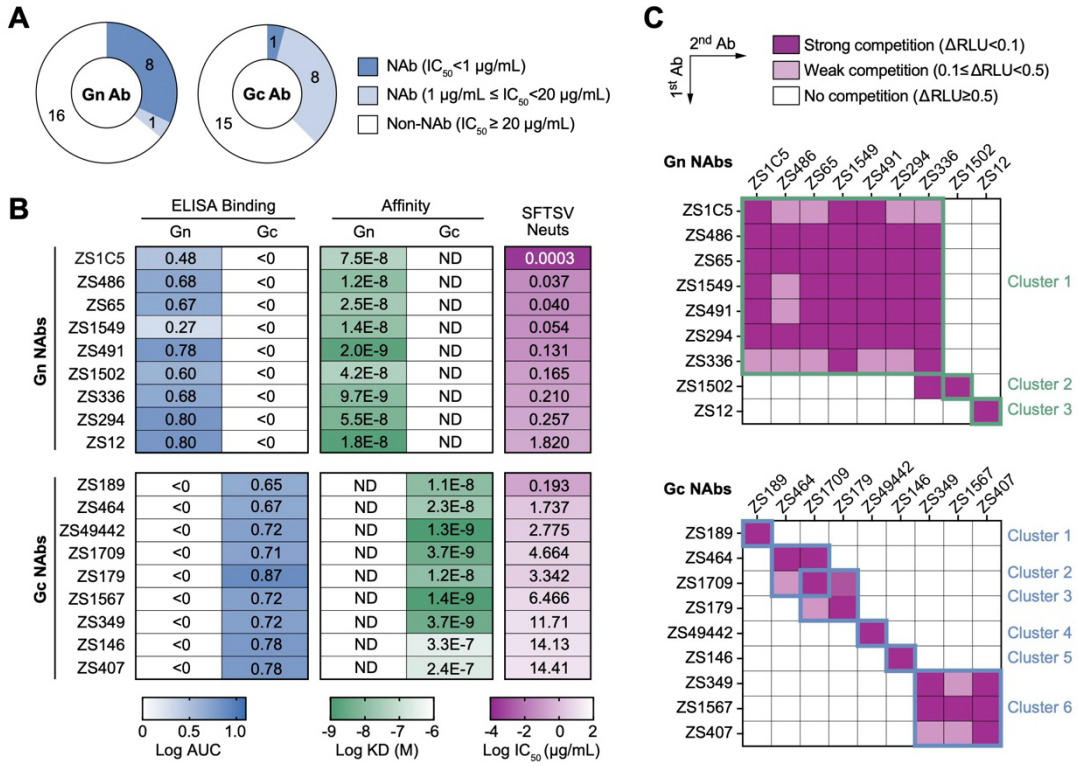


**Fig. 3. Isolation of an Ultrapotent SFTSV Neutralizing Antibody ZS1C5**.

**(A)** Summary of neutralization potencies of Gn/Gc-specific antibodies. Antibodies were categorized into potent neutralizing antibodies (NAbs), weak NAbs, and non-NAbs based on their fifty percent inhibitory concentrations ($IC_{50}$) as shown in the legend.

**(B)** Binding, affinity, and neutralization activities of NAbs. Binding to Gn/Gc was assessed by ELISA and expressed as logAUC. Affinities to antigens were measured using bio-layer interferometry (BLI) and reported as $K_D$ values. Neutralization capacities were evaluated using authentic SFTSV (genotype C4, strain WCH/97/HN/China/2011).

**(C)** Cross-competetion activities of NAbs tested by BLI. SFTSV Gn or Gc antigens were captured by one NAb (indicated on the y-axis), followed by the binding of a second NAb (indicated on the x-axis). The change in relative light units (ΔRLU) was calculated as the RLU of the second NAb minus the RLU of the first NAb. Antibodies were clustered based on cross-competetion patterns.

Langtaosha (LTS) Preprint doi: https://doi.org/10.65215/apb7tn58 This version posted November 28, 2025. The copyright holder for this preprint (which was not certified by peer review) is the author/funder. Creative Commons license: CC Attribution-NonCommercial-NoDerivatives 4.0 https://creativecommons.org/licenses/by-nc-nd/4.0

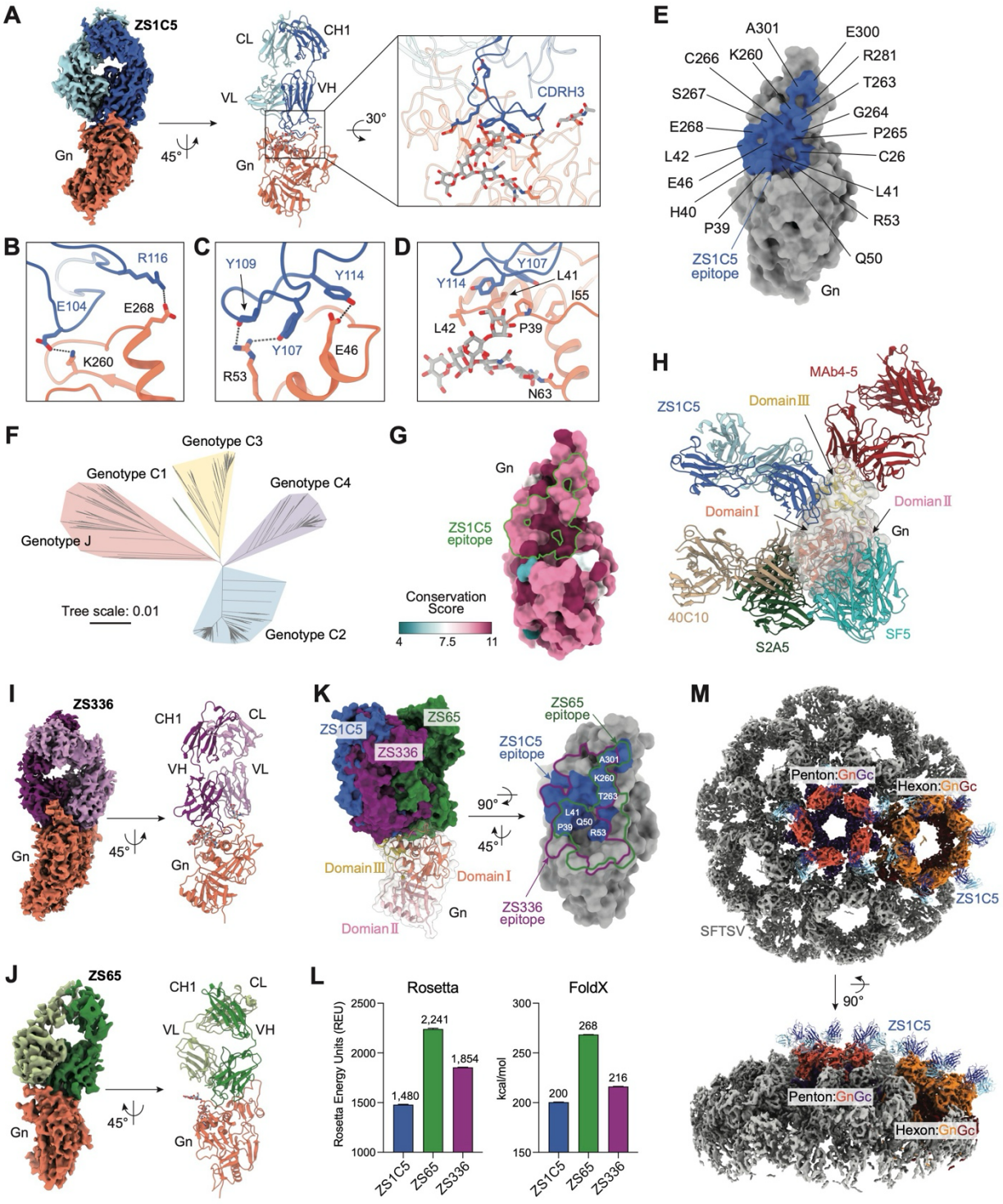


**Fig. 4. Binding of ZS1C5 to a Vulnerability Site Spanning Domain I and III of SFTSV Gn.**

Langtaosha (LTS) Preprint doi: https://doi.org/10.65215/apb7tn58 This version posted November 28, 2025. The copyright holder for this preprint (which was not certified by peer review) is the author/funder. Creative Commons license: CC Attribution-NonCommercial-NoDerivatives 4.0 https://creativecommons.org/licenses/by-nc-nd/4.0

753 **(A)** Cryo-EM structure of ZS1C5 Fab in complex with Gn. Inset shows binding interface; Gn:
754 orange; ZS1C5 heavy chain (HC): marine; ZS1C5 light chain (LC): cyan. Residues are shown as sticks.
755 Dashed lines indicate polar interactions.
756 **(B-D)** Key interactions at the Gn–ZS1C5 CDRH3 interface. (B) Salt bridges: $R116_{CDRH3}$-$E268_{Gn}$ and
757 $E104_{CDRH3}$-$K260_{Gn}$; (C) Hydrogen Bonds (H-bonds): $Y109_{CDRH3}$-$R53_{Gn}$, $Y107_{CDRH3}$-$R53_{Gn}$ and
758 $Y114_{CDRH3}$-$E46_{Gn}$; (D) Hydrophobic interactions: $Y114_{CDRH3}$, $Y107_{CDRH3}$ and $P39_{Gn}$, $L41_{Gn}$, $L42_{Gn}$, $I55_{Gn}$
759 and $N63_{Gn}$ glycan.
760 **(E)** ZS1C5 footprint on Gn surface.
761 **(F)** Radial phylogenetic tree of SFTSV constructed from 1,331 SFTSV *M* segment sequences
762 obtained from GenBank, with genotypes indicated.
763 **(G)** Conservation analysis of Gn with the ZS1C5 footprint highlighted in green. Conservation scores
764 were calculated from the alignment of 1,331 SFTSV M segment sequences, with each residue shaded
765 according to its conservation score.
766 **(H)** Overlay of ZS1C5 with published Gn-targeting antibodies MAb4-5 (red), SF5 (turquoise), S2A5
767 (forest) and 40C10 (wheat).
768 **(I-J)** Cryo-EM structures of ZS336 (I) and ZS65 (J) Fabs bound to Gn. Gn: orange; ZS336 HC: light
769 purple; ZS336 LC: violet; ZS65 HC: forest; ZS65 LC: pale green.
770 **(K)** Superposition and comparison of docking sites and footprints of ZS1C5 (marine), ZS336
771 (purple), and ZS65 (forest) on Gn domains I (orange), II (pink), and III (yellow).
772 **(L)** Energy comparison of Gn complexes with ZS1C5, ZS336, and ZS65, determined via FoldX and
773 Rosetta and shown as mean±SD from three independent runs.
774 **(M)** Visualization of ZS1C5 docked on SFTSV virion. SFTSV virion: gray; ZS1C5 HC: marine;
775 ZS1C5 LC: cyan. Penton: Gn in salmon, Gc in purple. Hexon: Gn in orange, Gc in maroon.
776

Langtaosha (LTS) Preprint doi: https://doi.org/10.65215/apb7tn58 This version posted November 28, 2025. The copyright holder for this preprint (which was not certified by peer review) is the author/funder. Creative Commons license: CC Attribution-NonCommercial-NoDerivatives 4.0 https://creativecommons.org/licenses/by-nc-nd/4.0

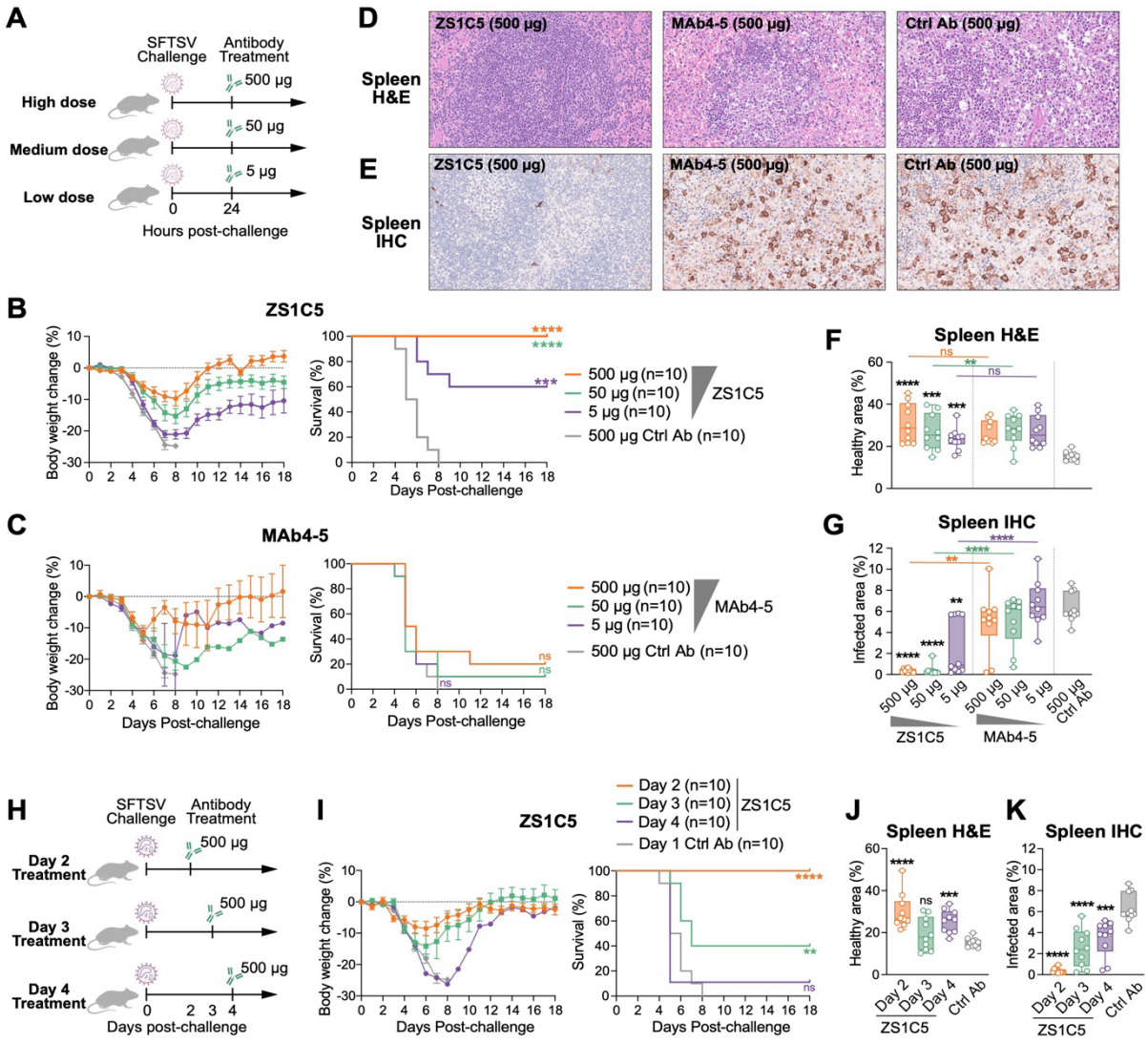


**Fig. 5. ZS1C5-Mediated Protection of Mice from Lethal SFTSV Challenge.**

**(A-G)** Dose-dependent ZS1C5 therapy. STAT1$^{-/-}$ mice (n=10/group) received ZS1C5 at high (500 μg), medium (50 μg), or low (5 μg) doses by intraperitoneal injection 24h post-SFTSV (WCH/97/HN/China/2011) infection; an irrelevant mAb served as a control. **(A)** Study design. **(B-C)** Body weight and survival rates after treatment with (B) ZS1C5 or (C) MAb4-5. **(D)** Representative spleen H&E staining. **(E)** Representative spleen IHC staining for SFTSV nucleoprotein (NP). **(F-G)** Quantification of spleen pathology by H&E (F, healthy area) and IHC (G, NP-positive area), scored using ImageJ.

Langtaosha (LTS) Preprint doi: https://doi.org/10.65215/apb7tn58 This version posted November 28, 2025. The copyright holder for this preprint (which was not certified by peer review) is the author/funder. Creative Commons license: CC Attribution-NonCommercial-NoDerivatives 4.0 https://creativecommons.org/licenses/by-nc-nd/4.0

786 **(H-K)** Time-dependent ZS1C5 therapy. STAT1$^{-/-}$ mice (n=10/group) received ZS1C5 (500 μg) at 48,
787 72, or 96 hours after infection. **(H)** Study design. **(I)** Changes in body weight and survival post-treatment.
788 **(J-K)** Quantification of spleen H&E staining (J, healthy area) and IHC staining (K, NP-positive area).
789 Tissue sections were analyzed and scored using ImageJ. Statistical analysis used Wilcoxon Rank
790 Sum Test; dots and error bars represent mean ± SEM. Asterisks indicate significance versus the control
791 group—except in (F-G), where colored asterisks mark significance between indicated groups. ns, not
792 significant; *$p < 0.05$; **$p < 0.01$; ***$p < 0.001$; ****$p < 0.0001$.
793

Langtaosha (LTS) Preprint doi: https://doi.org/10.65215/apb7tn58 This version posted November 28, 2025. The copyright holder for this preprint (which was not certified by peer review) is the author/funder. Creative Commons license: CC Attribution-NonCommercial-NoDerivatives 4.0 https://creativecommons.org/licenses/by-nc-nd/4.0

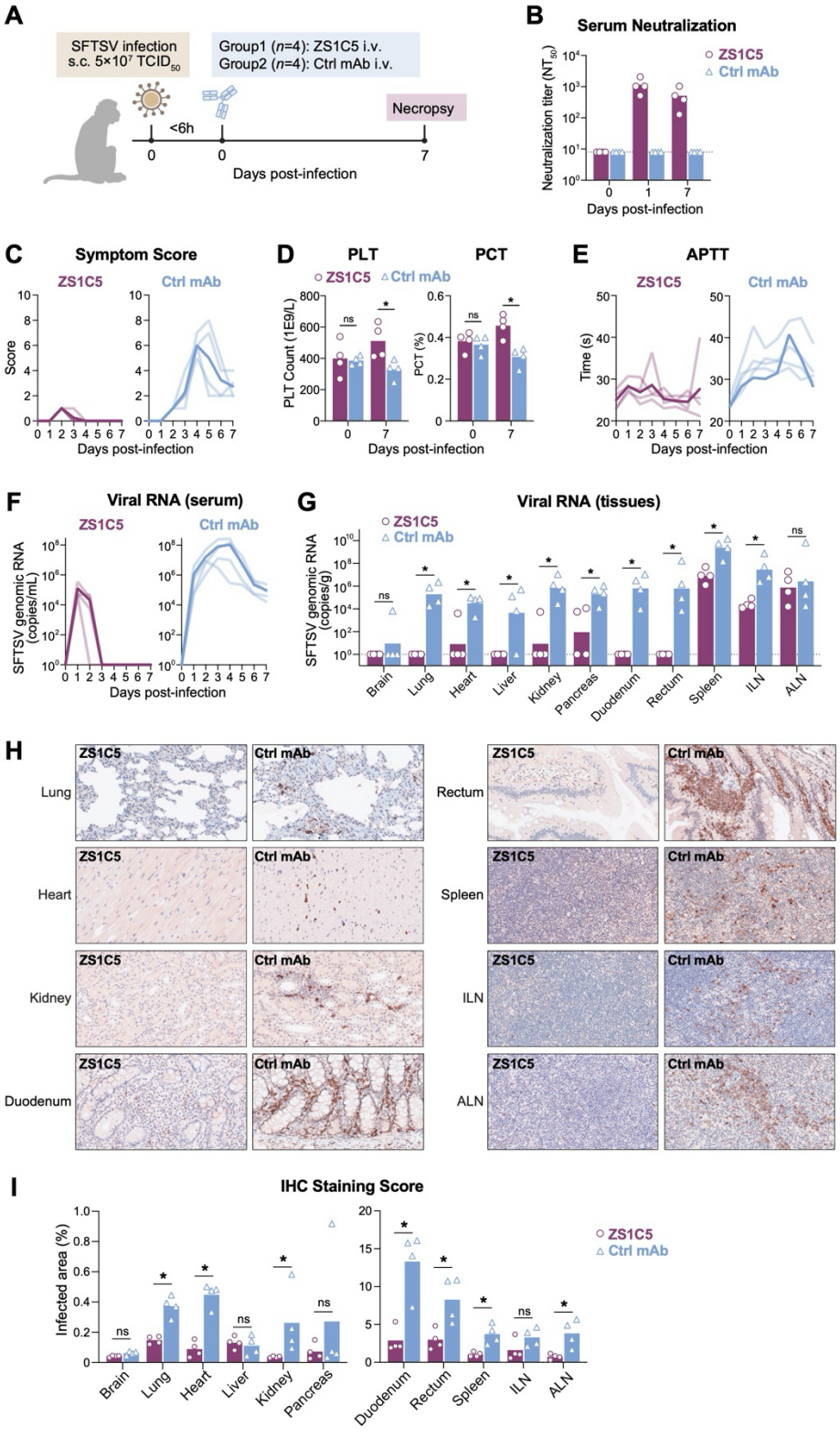


**Fig. 6. ZS1C5 Protection of Rhesus Macaques from SFTSV-Induced Disease and Viral Replication.**

Langtaosha (LTS) Preprint doi: https://doi.org/10.65215/apb7tn58 This version posted November 28, 2025. The copyright holder for this preprint (which was not certified by peer review) is the author/funder. Creative Commons license: CC Attribution-NonCommercial-NoDerivatives 4.0 https://creativecommons.org/licenses/by-nc-nd/4.0

**(A)** Study design. Rhesus macaques (n=4/group) were challenged with a multipoint subcutaneous (s.c.) injection of $5x10^7$ $TCID_{50}$ of SFTSV (HBMC5 strain). Within 6 hours, animals received an intravenous (i.v.) injection of ZS1C5 or an irrelevant control mAb (30 mg/kg body weight). Blood was collected daily, and necropsy occurred at day 7 post-challenge.

**(B)** Serum neutralization titers ($NT_{50}$) against SFTSV before and after ZS1C5 infusion (days 0, 1, 7). Detection limits are indicated by dashed lines.

**(C)** SFTSV-induced disease symptoms, including diarrhea, anorexia and lethargy, were monitored and scored daily.

**(D)** Platelet counts (PLT) and plateletcrit (PCT) on days 0 and 7.

**(E)** Daily measurements of activated partial thromboplastin time (APTT).

**(F-G)** SFTSV RNA quantification. (F) Serum viral RNA measured daily; (G) Tissue viral RNA assessed at endpoint in brain, lung, heart, liver, kidney, pancreas, duodenum, rectum, spleen, inguinal LN and axillary LN.

**(H-I)** IHC staining of multiple tissues. (H) Representative images for SFTSV NP expression; (I) Quantification of infected (NP-positive) areas.

Line charts show individual animals (light purple, ZS1C5; light steel blue, control mAb) with group means (bold lines). Bar charts: dots represent individual animals, bars indicate group mean. Statistical significance by Wilcoxon Rank Sum Test: ns, not significant; *$p < 0.05$.

Langtaosha (LTS) Preprint doi: https://doi.org/10.65215/apb7tn58 This version posted November 28, 2025. The copyright holder for this preprint (which was not certified by peer review) is the author/funder. Creative Commons license: CC Attribution-NonCommercial-NoDerivatives 4.0 https://creativecommons.org/licenses/by-nc-nd/4.0

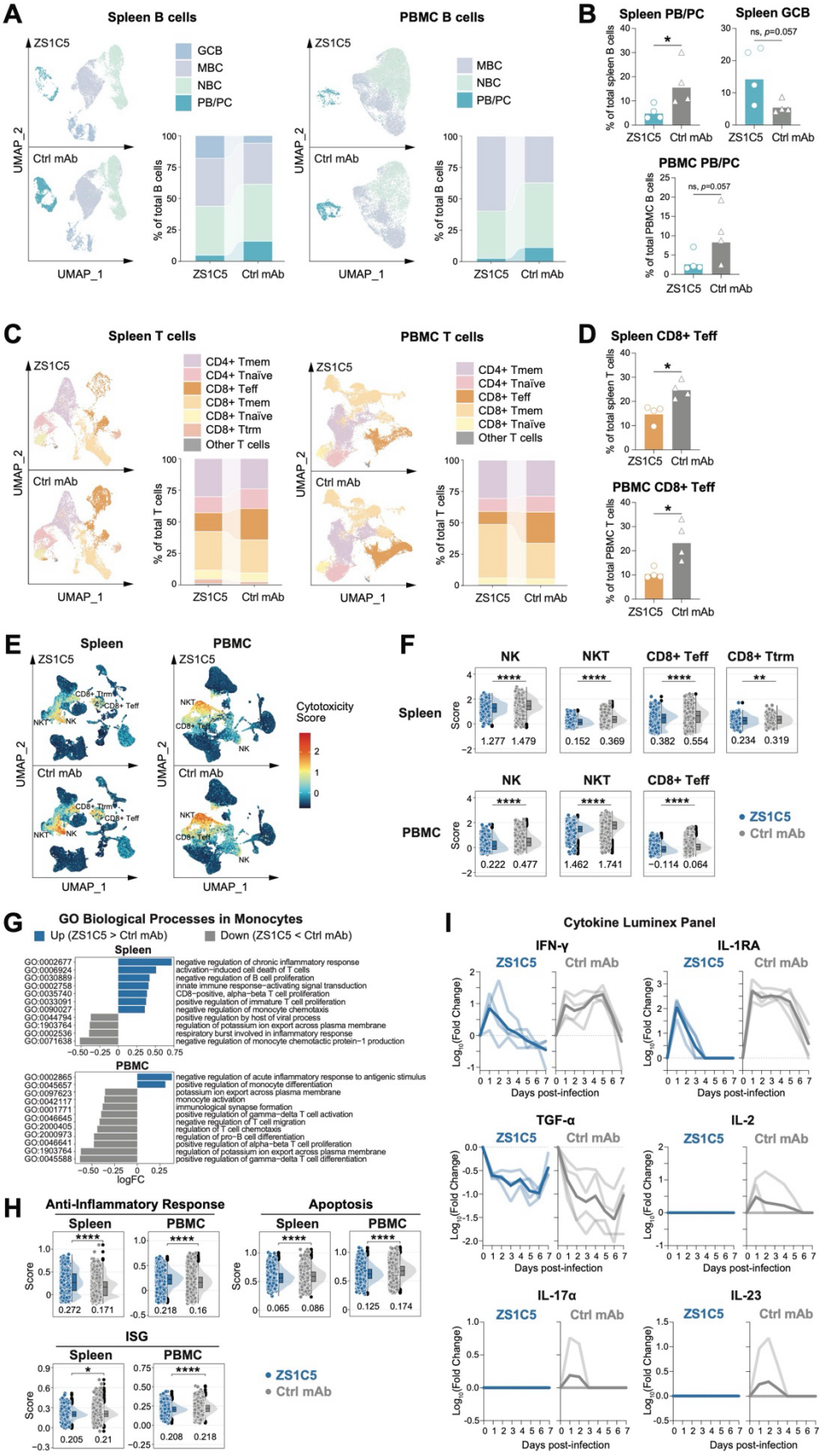


816

Langtaosha (LTS) Preprint doi: https://doi.org/10.65215/apb7tn58 This version posted November 28, 2025. The copyright holder for this preprint (which was not certified by peer review) is the author/funder. Creative Commons license: CC Attribution-NonCommercial-NoDerivatives 4.0 https://creativecommons.org/licenses/by-nc-nd/4.0

**Fig. 7. Single-Cell Transcriptom and Cytokine Profiling in SFTSV-Infected NHPs Treated with ZS1C5.**

**(A)** UMAP visualization of spleen and PBMC B cell subtypes in ZS1C5- and control-treated macaques, with subtype proportions shown in bar charts.

**(B)** Percentages of spleen plasmablast/plasma cell (PB/PC), PBMC PB/PC, and spleen germinal center B (GCB) cells in both groups. Dots represent individual animals; bars represent mean values.

**(C)** UMAP visualization of T cell subtypes and their proportions shown in bar charts.

**(D)** Percentages of CD8+ T effector (Teff) cells from spleen and PBMC in both groups.

**(E-F)** Cytotoxicity signature score comparisons in CD8+ T, NK, and NKT cells. (E) UMAP visualization of cytotoxicity score intensities. (F) Raincloud plots of cytotoxicity scores across groups, with average scores shown below each raincloud.

**(G)** Gene Set Variation Analysis (GSVA) in monocytes. Bar charts show Gene Ontology Biological Process (GOBP) terms with $\log_{10}$ fold-change (LogFC) >0.3 (higher in ZS1C5 group) shown in blue, and LogFC <-0.3 (higher in control group) shown in gray.

**(H)** Raincloud plots of anti-inflammatory, apoptosis, and interferon-stimulated gene (ISG) signature scores in monocytes. Average scores were shown below each raincloud.

**(I)** Cytokine expression dynamics monitored daily using Luminex. Fold changes relative to baseline (Day 0) for each animal are displayed with light blue/gray lines, and mean values are indicated by bold lines.

Bar charts: dots represent individual animals and bars indicate group mean. Statistical significances were performed using Wilcoxon Rank Sum Test. Raincloud plots: Signature scores were calculated using the *AddModuleScore* function in *Seurat* at the cellular level for each group. Statistical significance by *t*-test: ns, not significant; *p < 0.05; **p < 0.01; ***p < 0.001; ****p < 0.0001.

Langtaosha (LTS) Preprint doi: https://doi.org/10.65215/apb7tn58 This version posted November 28, 2025. The copyright holder for this preprint (which was not certified by peer review) is the author/funder. Creative Commons license: CC Attribution-NonCommercial-NoDerivatives 4.0 https://creativecommons.org/licenses/by-nc-nd/4.0

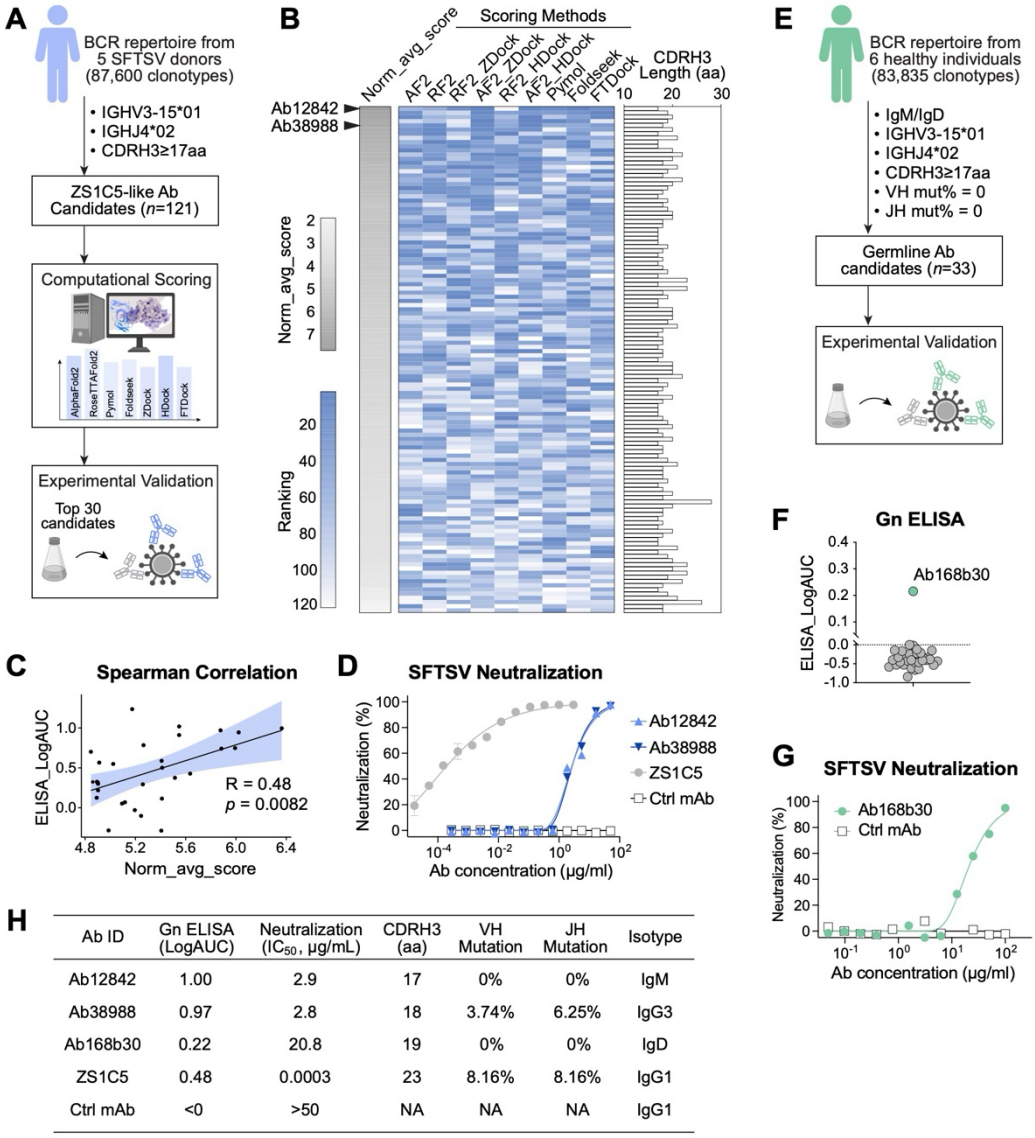


H

| Ab ID | Gn ELISA (LogAUC) | Neutralization ($IC_{50}$, μg/mL) | CDRH3 (aa) | VH Mutation | JH Mutation | Isotype |
|---|---|---|---|---|---|---|
| Ab12842 | 1.00 | 2.9 | 17 | 0% | 0% | IgM |
| Ab38988 | 0.97 | 2.8 | 18 | 3.74% | 6.25% | IgG3 |
| Ab168b30 | 0.22 | 20.8 | 19 | 0% | 0% | IgD |
| ZS1C5 | 0.48 | 0.0003 | 23 | 8.16% | 8.16% | IgG1 |
| Ctrl mAb | <0 | >50 | NA | NA | NA | IgG1 |

**Fig. 8. Computational Identification of ZS1C5-Like Neutralizing Antibodies from Human BCR Repertoire.**

**(A)** Workflow for ZS1C5-like NAb mining. From a BCR repertoire comprising 87,600 VH clonotypes, 121 ZS1C5-like antibody VH candidates were selected for computational scoring; the top 30 antibodies were expressed for downstream functional validation.

**(B)** Heatmap of the 121 candidates showing normalized average scores (gray) and rankings from individual tools (blue); CDRH3 lengths displayed as bar charts.

Langtaosha (LTS) Preprint doi: https://doi.org/10.65215/apb7tn58 This version posted November 28, 2025. The copyright holder for this preprint (which was not certified by peer review) is the author/funder. Creative Commons license: CC Attribution-NonCommercial-NoDerivatives 4.0 https://creativecommons.org/licenses/by-nc-nd/4.0

848 **(C)** Correlation of computational scores with ELISA binding activities for the top 30 purified
849 antibodies. Norm_avg_score, normalized average score; R, Spearman's correlation coefficient; p, p-value.
850 **(D)** Neutralization of SFTSV by two ZS1C5-like NAbs, with ZS1C5 as positive and irrelevant mAb
851 as negative control.
852 **(E)** ZS1C5-like germline antibody mining. From the BCR repertoire (83,835 VH clonotypes) of six
853 healthy individuals from the UK (*24*), 33 ZS1C5-like germline VH sequences were selected and
854 expressed for functional screening.
855 **(F)** ELISA binding of purified germline candidates to SFTSV Gn. Detection baseline was shown as
856 dashed line. Each dot represents a single antibody and green dot highlights Ab168b30.
857 **(G)** Neutralization of SFTSV by germline antibody Ab168b30.
858 **(H)** Summary table of ZS1C5-like NAbs, including binding and neutralization titers, CDRH3 length,
859 VH/JH SHM%, and isotype.
860

Langtaosha (LTS) Preprint doi: https://doi.org/10.65215/apb7tn58 This version posted November 28, 2025. The copyright holder for this preprint (which was not certified by peer review) is the author/funder. Creative Commons license: CC Attribution-NonCommercial-NoDerivatives 4.0 https://creativecommons.org/licenses/by-nc-nd/4.0

Supplementary Materials for

# A Potent Interdomain-Targeting Antibody Protects against SFTSV in Mice and Non-Human Primates

**This Word file includes:**

Materials and Methods

Supplementary Figs. S1 to S11

Supplementary Table S2

**Other Supplementary Materials for this manuscript includes the following:**

Supplementary Table S1, S3 and S4 (Excel files)

Langtaosha (LTS) Preprint doi: https://doi.org/10.65215/apb7tn58 This version posted November 28, 2025. The copyright holder for this preprint (which was not certified by peer review) is the author/funder. Creative Commons license: CC Attribution-NonCommercial-NoDerivatives 4.0 https://creativecommons.org/licenses/by-nc-nd/4.0

## MATERIALS AND METHODS

### Human Subjects and PBMC Isolation

Convalescent blood samples were collected from 4 donors (3 male and 1 female) who had been previously infected with SFTSV between 2016 and 2022. In another group of donors, both acute- and convalescent-phase samples were collected from 12 individuals (3 males and 9 females) who were hospitalized for treating SFTSV infection in the summer of 2023. Peripheral blood was collected during both the acute (Days 4-7 after the onset of the symptoms) and convalescent phases (2 months after discharge) based on informed consent. One of the donors received submandibular lymph node dissection on day 5 after the onset of the symptoms to have one of the submandibular lymph nodes removed, from which we obtained lymph node B cell samples. This study was approved by the Ethics Review Committee of Zhoushan Hospital (IRB#2022430) and Westlake University (IRB#20230414LDP001).

Fresh anticoagulated whole blood from donors was collected, and peripheral blood mononuclear cells (PBMCs) were isolated using lymphocyte separation tubes (DAKEWE, Cat#7922112) according to the manufacturer's instructions. Briefly, 10 mL of blood containing EDTA was centrifuged at 1,200 g for 10 min. The upper plasma was transferred to a new tube and stored at -80°C. The lower cell layer was carefully transferred to a new tube, mixed with an equal amount of D-PBS (Gibco, Cat#C14190500BT), and centrifuged again. The middle layer, consisting of white PBMCs, was carefully transferred to a new tube and washed twice with a large volume of D-PBS containing 2 % FBS (ExCellBio, Cat# FSP500) at 300 g for 8 min. Finally, the cells were resuspended in 500 μL of 2 % FBS D-PBS and counted. The entire blood processing procedure was completed in a BSL-2 laboratory at Westlake University (BSL20225712116).

### Recombinant Protein Expression and Purification

The codon-optimized SFTSV Gn head domain (aa20-340, Genbank: AQX34652.1) and Gc head domain (aa563-996, Genbank: AQX34652.1) were individually clone into the pCAGGS with N-terminal Kozak sequence and IL-2 signal sequence, and with a C-terminal 10× His-tag. The recombinant

Langtaosha (LTS) Preprint doi: https://doi.org/10.65215/apb7tn58 This version posted November 28, 2025. The copyright holder for this preprint (which was not certified by peer review) is the author/funder. Creative Commons license: CC Attribution-NonCommercial-NoDerivatives 4.0 https://creativecommons.org/licenses/by-nc-nd/4.0

glycoproteins were expressed transiently by transfecting Expi293F cells using PEI MAX (Polysciences, Cat#24765). Five days post-transfection, the supernatant was collected by centrifugation and filtered through a 0.22 μm filter before purification. Cell supernatants were purified using a $Ni^{2+}$ chromatography column (SunResin, Cat#A453201) on the AKTA system.

**Antigen-specific B cell Sorting**

Antigen-specific B cells were sorted from freshly isolated PBMCs samples. Specifically, PBMCs were stained with anti-human IgD conjugated FITC (BioLegend, Cat#348206), anti-human IgM conjugated PerCP-Cy5.5 (BD Biosciences, Cat#561285), anti-human CD3 conjugated PE-Cy5 (BioLegend, Cat#300310), anti-human CD27 conjugated PE-Cy7 (BioLegend, Cat#302838), anti-human CD38 conjugated AF700 (BioLegend, Cat#303524), anti-human CD19 conjugated APC-Cy7 (Biolegend, Cat#363010), anti-human CD14 conjugated BV605 (Biolegend, Cat#301834), anti-human CD16 conjugated BV785 (BioLegend, Cat#302046), Zombie Aqua (BioLegend, Cat#423102) for live/dead, at 4 ℃ for 30 min in the dark. To probe SFTSV-Gn/Gc specific B cells, the his-tagged Gc and Gn were incubated with PE anti-His (BioLegend, Cat#362603) and APC anti-His (BioLegend, Cat#362605). Bait proteins were subsequently incubated with PBMCs in separate tubes. After fluorescent surface staining, the PBMCs were loaded onto a CytoFLEX SRT (Beckman) for analysis and sorting. SFTSV-Gn/Gc specific B cells were gated as CD14-CD16-CD3-CD19+IgM-IgD-PE+ and CD14-CD16-CD3-CD19+IgM-IgD-APC+, respectively.

For antibody gene PCR and cloning, antigen-specific B cells were single-cell sorted into 96-well PCR plates containing 20 μL per well of lysis buffer [2.5 μL of 10x RT buffer, 2.5 μL of 5x gDNA wiper mix (Vazyme, Cat#R312), 0.0625 μL of IGEPAL (Sigma-Aldrich, Cat#I8896), 0.5 μL of Carrier RNA (Sangon Biotech, Cat#B518271-0100), and 14.4375 μL $dH_2O$]. The plates were briefly centrifuged and then stored at -80℃. For single-cell transcriptome and BCR sequencing, antigen-specific B cells were sorted into D-PBS containing 2 % FBS and counted for subsequent sequencing analysis. For bulk RNA-

Langtaosha (LTS) Preprint doi: https://doi.org/10.65215/apb7tn58 This version posted November 28, 2025. The copyright holder for this preprint (which was not certified by peer review) is the author/funder. Creative Commons license: CC Attribution-NonCommercial-NoDerivatives 4.0 https://creativecommons.org/licenses/by-nc-nd/4.0

seq, non-antigen specific B cells were collected into a tube and lysed with 1 mL of Trizol (TaKaRa, Cat#9109) for RNA extraction and subsequent sequencing analysis.

**Single B cell PCR and Antibody Cloning**

The antibody gene PCR and cloning was performed as previously described (*25*). Briefly, cDNA is generated from sorted single B cell RNA by HiScript III 1st strand cDNA Synthesis Kit (Vazyme, Cat#R312). Correspondingly, heavy chain (HC) and light chain (LC) were amplified with 2 rounds of PCRs, where the first-round primer sets target 5' leader region and immunoglobulin (Ig) constant regions to amplify different Ig fragments, the second-round primer sets perform a nested-PCR for targeted amplification of HC and LC, as well as to incorporate homologous end of the expression vectors. The resulting PCR products were visualized on 1% agarose gels, and bands at ~500 bp and ~450 bp were sent for sequencing as HC and LC sequences, respectively. The sequenced DNA was analyzed on IMGT/V-QUEST. The identified HC and LC pairs from the second-round PCR were digested and cloned (Vazyme, Cat#C116) into mammalian expression vectors.

**Human Single-Cell Transcriptome and BCR Sequencing**

PBMCs RNA were extracted, and quality control was performed (Agilent 4200). The RNA samples were then analyzed by high-throughput sequencing of IGH with the BCR profiling system at a deep level. Briefly, a 5' RACE unbiased amplification protocol was used. This protocol utilizes unique molecular barcodes (UMBs) introduced during cDNA synthesis to control bottlenecks and minimize PCR and sequencing errors. Sequencing was performed on an Illumina NovaSeq system using the PE150 mode (Illumina, X plus). The UMBs attached to each raw sequence read were applied to correct PCR and sequencing errors and to remove PCR duplicates.

**Human Sequencing Data Processing and Cell Type Identification**

Langtaosha (LTS) Preprint doi: https://doi.org/10.65215/apb7tn58 This version posted November 28, 2025. The copyright holder for this preprint (which was not certified by peer review) is the author/funder. Creative Commons license: CC Attribution-NonCommercial-NoDerivatives 4.0 https://creativecommons.org/licenses/by-nc-nd/4.0

For the single-cell transcriptome sequencing data obtained from patient PBMCs, we applied the Cell Ranger (v7.2) workflow for the assembly and annotation of the raw sequencing data. The reference genome used was the GRCh38 human reference genome downloaded from the 10× Genomics official website. The expression matrix processed by Cell Ranger was further analyzed using the Seurat R package for downstream dimensionality reduction, clustering, and cell annotation. For the integrated object, cells with nFeature values greater than 200 and less than 8,000, and nCount values less than 70,000, were filtered for subsequent analysis. A total of 45,654 cells were included in the study after filtering. After removing batch effects, we performed dimensionality reduction and clustering on the data. The dims value was set to 1:25, and the resolution value was set to 0.6. We identified the differentially expressed genes in cell clusters using the FindAllMarkers function and annotated cell types and subtypes using both the SingleR and SCSA methods. The marker gene database for SCSA was the human blood marker gene set downloaded from the CellMarker 2.0 database.

**Antibody Gene Sequence and Clonal Analysis**

The antibody sequences involved in this study were derived from single-cell BCR sequencing data from 11 samples of 5 patients, bulk BCR sequencing data from 3 patient samples, and single-cell BCR sequencing data from 1 pooled sample. Single-cell BCR sequencing data were processed and annotated using the VDJ module of Cell Ranger (v7.2), with the GRCh38 Human V(D)J reference (GRCh38-alts-ensembl-7.1.0) downloaded from the 10× Genomics website as the reference genome. Bulk BCR sequencing data were assembled and annotated using TRUST4 (v1.0.13), with the reference genome provided by TRUST4 (hg38_bcrtcr.fa) and the detailed V/D/J/C gene reference file downloaded from the IMGT database.

The identification of antibody clonal lineages was performed using the Change-O workflow. The workflow employed the IMGT human IG reference for processes such as IgBLAST and germline reconstruction. For single-cell BCR data, annotations from the Cell Ranger VDJ module were additionally incorporated. During clone definition, nucleotide Hamming distance was used as the

Langtaosha (LTS) Preprint doi: https://doi.org/10.65215/apb7tn58 This version posted November 28, 2025. The copyright holder for this preprint (which was not certified by peer review) is the author/funder. Creative Commons license: CC Attribution-NonCommercial-NoDerivatives 4.0 https://creativecommons.org/licenses/by-nc-nd/4.0

substitution model for calculating sequence distances. The clone definition distance threshold was determined using the distToNearest function in the SHazaM R package. Ultimately, antibodies sharing the same V and J genes and with inter-sequence distances of less than 0.1100311 were identified as belonging to the same clone.

**Production of Monoclonal Antibodies**

For antibody plasmids derived from single B cell PCR and cloning, purified PCR products were used for overlapping PCR to generate linear human IgG expression cassettes as previously described (*25*). The expression cassettes were transfected into 3 mL Expi293F cells using PEI MAX. The supernatant samples containing recombinant IgGs were used for IgG quantification and preliminary ELISA binding screening. For antibody genes obtained through single-cell BCR sequencing, HC and LC genes were synthesized and cloned into mammalian expression vectors. Plasmids were transfected into 10 mL Expi293F cells, harvested after 4 days, and then purified using protein A magnetic bead (GenScript, Cat#L00695) enrichment for preliminary ELISA binding screening and neutralization assay. Antibodies that showed positive ELISA results and visibly reduced virus foci were selected for large-scale production. To produce antibodies JK-8 (*16*), MAb4-5 (*8, 10*), 40C10 (*13, 14*), S2A5 (*12*), and SF5 (*15*), the HC and LC variable regions were synthesized and cloned into human IgG expression cassettes for subsequent large-scale production.

For large-scale production of the down-selected antibodies, HC and LC plasmids were expressed transiently by transfecting Expi293F cells with a 1:1 ratio using PEI MAX. After 5 days, the supernatant was collected by centrifugation and filtered through a 0.22 μm filter before purification. Cell supernatants were purified using protein A affinity chromatography column (SunResin, Cat#A4093101) on the AKTA system. This was eluted with 100 mM glycine at pH 2.5 and neutralized with 1/10 volume of 1 M Tris-HCl. The eluted mAbs were buffer-exchanged into PBS.

**ELISA**

Langtaosha (LTS) Preprint doi: https://doi.org/10.65215/apb7tn58 This version posted November 28, 2025. The copyright holder for this preprint (which was not certified by peer review) is the author/funder. Creative Commons license: CC Attribution-NonCommercial-NoDerivatives 4.0 https://creativecommons.org/licenses/by-nc-nd/4.0

To assess antibody-antigen binding by ELISA, 96-well high-binding ELISA plates were coated overnight with specific glycoproteins at 0.5 μg/mL. Plates were washed three times in wash buffer (PBST, 0.1% Tween-20 in D-PBS) and blocked with 100 μL/well of blocking buffer (3% BSA in PBS) for 2 h at 37℃. Plates were washed with wash buffer, and antibodies diluted to 5 μg/mL in blocking buffer were added to the first well, followed by 3-fold serial dilutions across subsequent wells. Following 2 h incubation, the plates were washed, and a 1:5000 dilution of anti-human IgG-HRP (Promega, Cat#W4031) was added and incubated for 1 h. The plates were washed three times in the washing buffer. TMB Chromogen solution (Beyotime, Cat#P0209) was added at 100 μL per well and developed for 10 minutes at room temperature in the dark. After which, the reaction was stopped with 50 μL 1M sulfuric acid per well. Absorbance was measured at 450nm. All mAbs were tested in duplicates.

**Bio-layer Interferometry (BLI)**

BLI kinetic measurements were acquired at 30℃ with an Octet protein analysis system (Sartorius, Octet R8). For binding kinetics, antibodies (Basic buffer: 0.1% BSA in D-PBS) were captured with Protein A sensors (Sartorius, Cat#18-5010) for 300 s as loading. After loading, the baseline was recorded for 200 s in the basic buffer before association. For association, the sensors were immersed in the antigen solution with serial 3-fold dilutions for 300 s. Following that, the sensors were dipped into a basic buffer for 600 s to facilitate dissociation. The sensors were regenerated with Glycine-HCl to start a new round of binding. The binding curves were fit to a 1:1 binding model using the Octect Analysis Studio 13.0.2.46.

Cross-blocking BLI was established by loading the Gn/Gc protein onto HIS1K biosensors (Sartorius, Cat#18-5120), followed by association with the first antibody. Subsequently, the antibody-antigen complexes were incubated with the same or a second antibody. The experimental conditions were the same as previously described. The shifted binding signal between the second mAb and the first, resulting from different binding domains, was captured and reported as relative light units (RLU). Data were analyzed using the Epitope Binning model in Octet Analysis Studio.

Langtaosha (LTS) Preprint doi: https://doi.org/10.65215/apb7tn58 This version posted November 28, 2025. The copyright holder for this preprint (which was not certified by peer review) is the author/funder. Creative Commons license: CC Attribution-NonCommercial-NoDerivatives 4.0 https://creativecommons.org/licenses/by-nc-nd/4.0

**Neutralization Assay**

Antibodies were diluted to a starting concentration of 1 μg/well, followed by serial 2-fold dilutions. Authentic SFTSV (WCH/97/HN/China/2011 Strain) at $10^2$ $TCID_{50}$/well was incubated with diluted antibodies for 1 h at 37°C. $1.5 \times 10^6$ cells/well of Vero cells were added to the antibody-virus mixture in a 96-well plate and incubated for 48 h at 37°C. To perform immunofluorescence, infectious media was discarded, and cells were fixed and permeabilized with pre-cooled 80% acetone at room temperature for 30 minutes. Plates were then washed twice with PBST, followed by incubation with the primary antibody, anti-SFTSV-NP polyclonal antibody (1:200), for 2 h at 37°C. Then, the plates were washed and incubated with 2000-fold diluted goat anti-rabbit IgG, conjugated to AF488 (Thermo, Cat#A-11008), for 1 h at 37°C in the dark. Infected cells were visualized under the fluorescence microscope. $IC_{50}$ values for each antibody were determined from log response curves with variable slopes and four parameters using nonlinear regression analysis (GraphPad Prism 10).

**Cryo-EM Sample Preparation and Data Collection**

The Gn was incubated with antibodies at a molar ratio of about 1: 3 for two hours. Then the mixture was subject to size-exclusion chromatography (Cytiva, Superose Increase 10/300 GL) in buffer containing 25 mM Tris (pH 8.0), 150 mM NaCl. The peak fractions were collected and concentrated for EM analysis. The complex of Gn bound with ZS1C5, 336 and 65 were concentrated to ~ 3.5 mg/mL and applied to the grids, respectively. Aliquots of the protein (3.5 μL) were deposited on glow-discharged holey carbon grids (Quantifoil Au R1.2/1.3). The grids were blotted for a period of 4 s and flash-frozen in liquid ethane cooled by liquid nitrogen with a Vitrobot (Thermo Fisher Scientific, Mark IV). The prepared grids were transferred to a Titan Krios operating at 300 kV, which is equipped with a Gatan K3 detector and a GIF Quantum energy filter. The movie stacks were automatically collected using the EPU software (Thermo Fisher Scientific), with a slit width of 20 eV on the energy filter and a defocus range from ~ 1.2 μm to ~ 2.2 μm in super-resolution mode at a nominal magnification of 81,000×. Each stack

Langtaosha (LTS) Preprint doi: https://doi.org/10.65215/apb7tn58 This version posted November 28, 2025. The copyright holder for this preprint (which was not certified by peer review) is the author/funder. Creative Commons license: CC Attribution-NonCommercial-NoDerivatives 4.0 https://creativecommons.org/licenses/by-nc-nd/4.0

was exposed for 2.56 s, with an exposure time of 0.08 s per frame, resulting in a total of 32 frames per stack. The total dose rate was ~ 50 e-/Å2 for each stack.

**Cryo-EM Data Processing**

The movie stacks were motion corrected with MotionCor2(*26*) and binned twofold, resulting in a pixel size of 1.087 Å/pixel. Meanwhile, dose weighting was performed(*27*). Then the preprocessing movie stacks were imported to CryoSPARC (v4.6.0, Structure Biotechnology) for CTF estimation and downstream processing(*28, 29*). Particles of Gn-Abs complex were automatically picked using CryoSPARC(*29*). After 2D classification, the particles with clear secondary structure features were selected and subjected to ab-initio reconstruction to obtain the initial models, then multi-heterogeneous refinement without symmetry were performed to selected good particles using CryoSPARC. The selected particles were subjected to non-uniform refinement, global CTF refinement and local refinement with C1 symmetry, resulting in the 3D reconstruction for the whole structures. However, the ZS65 complex failed to yield a high-resolution density map after the above-mentioned processing steps. Therefore, the obtained particles were proceeded to transfer to Relion(*30-33*) for further 3D classification. Finally, the best class were selected and subjected to 3D refinement to get a superior overall map. The resolution was estimated with the gold-standard Fourier shell correlation 0.143 criterion(*34*) with high-resolution noise substitution(*35*). Refer to ***Table S2*** for details of data collection and processing.

**Model Building and Structure Refinement**

In the construction of the ZS1C5 model, the predicted atomic model generated by Alphafold 2 (*36, 37*) was employed as a template. That was then subjected to molecular dynamics flexible fitting(*38*) and manual adjustment with Coot(*39*) to create the atomic model of the antibody in its various states. Each residue was manually checked with the chemical properties taken into consideration during model building. For the complex, the model building was performed on the basis of the focused refinement. For the rGn, the atomic model (PDB ID: 5Y10) was used as a template. Each residue was manually checked

Langtaosha (LTS) Preprint doi: https://doi.org/10.65215/apb7tn58 This version posted November 28, 2025. The copyright holder for this preprint (which was not certified by peer review) is the author/funder. Creative Commons license: CC Attribution-NonCommercial-NoDerivatives 4.0 https://creativecommons.org/licenses/by-nc-nd/4.0

against the chemical properties considered during model building. Several segments whose corresponding densities were not visible were not modelled. Structural refinement was performed in Phenix(*40*) with secondary structure and geometry constraints to prevent overfitting. To monitor for potential overfitting, the model was refined against one of the two independent half maps from the gold standard 3D refinement approach. The refined model was then tested against the other map. Statistics associated with data collection, 3D reconstruction, and model building of other antigen-antibody complex structures are provided in ***Table S2***.

**Conservation Analysis**

All 1,331 SFTSV *M* segment sequences used for conservation analysis were downloaded from the NCBI GenBank database (Taxonomy ID:1003835 and 2748958), and screened to ensure sequence integrity and accurate translation. The amino acid sequences for the Gn protein were derived from the nucleotide sequences, with residues 23–340 (matching the structural model) extracted for further analysis.

Phylogenetic trees were constructed using the Neighbor-Joining method implemented in MEGA X, based on the 1,331 complete M segment sequences. Tree confidence was assessed with 1,000 bootstrap replications. Evolutionary distances were computed with the Kimura 2-parameter method and are expressed as the number of base substitutions per site.

For conservation analysis, conservation scores were calculated using Jalview (*41*), with scores ranging from 0 (non-conserved) to 11 (highly conserved). A custom Python script assigned these conservation scores to the B-factor field of the Gn structure file, and epitope conservation was visualized using ChimeraX.

**Energy Calculation**

We evaluated the structural stability of the antigen–antibody complex using both FoldX(*42*) and Rosetta(*43*). FoldX computes an empirical folding free energy in kcal/mol using a fast physics-based energy function, while Rosetta reports a total energy score in Rosetta Energy Units (REU) derived from a

Langtaosha (LTS) Preprint doi: https://doi.org/10.65215/apb7tn58 This version posted November 28, 2025. The copyright holder for this preprint (which was not certified by peer review) is the author/funder. Creative Commons license: CC Attribution-NonCommercial-NoDerivatives 4.0 https://creativecommons.org/licenses/by-nc-nd/4.0

combination of physical and statistical potentials. Although the units are not directly comparable, both methods provide relative metrics for structural stability and were used for cross-validation.

To perform the energy calculation, all antigen–antibody complexes were truncated to ensure consistent antigen sequence length (residues 23–340 of Gn), and antibodies were trimmed to retain only the variable region. For FoldX, the input structures were first preprocessed using the RepairPDB command to correct structural errors. Then, the Stability command was used to calculate the folding free energy (ΔG_folding) of the entire complex. For Rosetta, we employed the rosetta_relax to optimize each complex structure and evaluate its total energy score. Each structure was subjected to three independent runs in parallel.

**Computational Identification of Structurally Related Antibodies**

We employed multiple methods to assess the structural similarity between candidate antibodies and the target antibody. The crystal structures of all candidate antibodies were predicted as monomeric structures using AlphaFold v2.3 and RoseTTAFold v2. Structural similarity searches between candidate antibodies and the target antibody were conducted using the align function in PyMOL v2.5.7 and the easy-search module in Foldseek v8.ef4e960.

To evaluate the binding capability of candidate antibodies to the target antigen epitope, we used three docking prediction tools: ZDOCK v3.0.2, HDOCK v1.1, and FTDock v2.0. ZDOCK and HDOCK were utilized to directly assess binding to the antigen epitope, while FTDock employed SCscore to evaluate the similarity between candidate and target antibodies.

The final scoring for candidate antibodies comprised nine components: the mean pLDDT of AlphaFold2 monomeric predictions, the mean pLDDT of RoseTTAFold2 monomeric predictions, HDOCK scores for RoseTTAFold2-predicted structures, HDOCK scores for AlphaFold2-predicted structures, ZDOCK scores for RoseTTAFold2-predicted structures, ZDOCK scores for AlphaFold2-predicted structures, RMSD values from PyMOL align, Pidentity scores from Foldseek easy-search, and

Langtaosha (LTS) Preprint doi: https://doi.org/10.65215/apb7tn58 This version posted November 28, 2025. The copyright holder for this preprint (which was not certified by peer review) is the author/funder. Creative Commons license: CC Attribution-NonCommercial-NoDerivatives 4.0 https://creativecommons.org/licenses/by-nc-nd/4.0

SCscore from FTDock. Each of the nine scores was normalized to a 1-10 scale, and the final candidate antibody score was calculated as the average of these normalized values.

**Mouse Challenge**

The dose-dependent efficacy of ZS1C5 was evaluated in STAT1$^{-/-}$ mice [Jax#012606, B6.129S(Cg)-Stat1$^{tm1Dlv}$/J; n = 10 per group] infected intraperitoneally (i.p.) with 10 $LD_{50}$ of SFTSV (WCH/97/HN/China/2011 Strain). Three doses of ZS1C5 (high: 500 μg, medium: 50 μg, low: 5 μg) were administered i.p. 24 hours post-infection, alongside a control human antibody (*44*) (500 μg). Survival rates, body weight changes, and tissue pathology (liver, spleen, lungs, kidneys) were monitored for 18 days. At the end of the study, mice were euthanized, and tissues were fixed in 4% paraformaldehyde for histopathological analysis using hematoxylin and eosin (H&E) staining and immunohistochemical (IHC) staining with a rabbit anti-SFTSV nucleoprotein (NP) polyclonal antibody (developed in-house). Representative tissue sections were analyzed using ImageJ software. For H&E sections, the healthy tissue area ratio was quantified using the color deconvolution plugin in "vectors=H&E" mode. For IHC sections, the infected tissue area ratio was determined by splitting channels, isolating the layer specifically recognized by anti-SFTSV NP polyclonal antibodies, and performing quantitative analysis.

A separate study was conducted to evaluate time-dependent efficacy. ZS1C5 (500 μg) was administered at 48, 72, and 96 hours post-infection with 10 $LD_{50}$ SFTSV. All experiments were conducted in an ABSL-2 facility, where mice were provided with adequate food and water throughout the experiment. Ethical approval for the animal challenge study was obtained from the Biosafety Committee of Westlake University (Approval ID: AP#22-069-2-LDP; applied on September 19, 2022; approved on October 31, 2022).

**NHP Challenge**

The SFTSV HBMC5 strain (genotype C3, GenBank ID: KY440769-KY440771), purified through two rounds of plaque isolation, was used to infect eight male rhesus monkeys (*Macaca mulatta*) aged 3-5

Langtaosha (LTS) Preprint doi: https://doi.org/10.65215/apb7tn58 This version posted November 28, 2025. The copyright holder for this preprint (which was not certified by peer review) is the author/funder. Creative Commons license: CC Attribution-NonCommercial-NoDerivatives 4.0 https://creativecommons.org/licenses/by-nc-nd/4.0

years (4-6 kg). Animals were randomly divided into two groups and administered multiple subcutaneous injections of $5 \times 10^7$ $TCID_{50}$ SFTSV in the hind limb inner surface. Six hours post-infection, monkeys received intravenous injections of either 30 mg/kg ZS1C5 (test antibody) or S2P6 (*45*) (control anti-SARS-CoV-2 spike antibody) at 2 mL/min. Both antibodies were produced via transient transfection in Expi293F cells (10 L fermentation scale) and subjected to endotoxin adsorption (Thermo Fisher Scientific, Cat#88274). Endotoxin levels were confirmed below 5 EU/kg/h during infusion using a chromogenic assay (Thermo Fisher Scientific, Cat#A39552).

Clinical scores were obtained by trained observers who were blinded to the vaccine groups from 0 to 7 dpi. Two observers recorded symptoms for 30 min each morning for each group. Clinical symptoms included spontaneous movement, feeding behavior, coat hair, muscle stiffness, urine color, faeces, reaction to tactile stimulation, and abdominal palpation. These indicators are further categorized into two levels: Healthy (0 point) and Sick (1 ponit). Scores are assigned based on actual observations. The sum of all scores is the total score. Specific evaluation criteria and symptom severity grading are detailed in ***Table S3***.

Body weight and temperature were monitored daily. Blood samples were collected continuously from 0-7 days post-infection for hematological profiling, viral load quantification, and serum-based analyses (biochemistry, coagulation, ELISA, neutralization assays, and cytokine Luminex assays). All procedures, including blood sampling, body weight, temperature measurement and euthanasia, were conducted under respiratory anesthesia.

Euthanasia was performed at 7 dpi, followed by complete necropsy. Heart, liver, spleen, lungs, kidneys, brain, pancreas, rectum, duodenum, axillary lymph nodes, and inguinal lymph nodes were collected for H&E staining, IHC staining, and viral load quantification.

The NHP experiments were conducted at the National Kunming High-level Biosafety Primate Research Center (ABSL-3). All rhesus macaques had a microbial background that met the national standard (GB 14922-2022). During the breeding and experimental periods, all animals were provided with readily accessible and adequate food, water, and veterinary care. The experiments were approved by

Langtaosha (LTS) Preprint doi: https://doi.org/10.65215/apb7tn58 This version posted November 28, 2025. The copyright holder for this preprint (which was not certified by peer review) is the author/funder. Creative Commons license: CC Attribution-NonCommercial-NoDerivatives 4.0 https://creativecommons.org/licenses/by-nc-nd/4.0

the Ethics Committee of the Chinese Academy of Medical Sciences and Peking Union Medical College (DWSP202410014).

**Complete blood count (CBC), Basic Metabolic Panel (BMP), and Coagulation Test**

During the entire monitoring period, from 0 to 7 dpi, rhesus monkeys were subjected to daily respiratory anesthesia for the collection of peripheral blood. Serum was collected using clot activator tubes and centrifuged at 3,000 rpm for 30 min at 4 °C. Whole blood was collected using EDTA anticoagulant tubes, and plasma samples were collected after additional centrifugation to obtain the supernatant. Complete blood counts (CBC) were performed using a five-part differential veterinary automatic hematology analyzer (Mindray, BC-5000Vet) with fresh whole blood collected daily. The parameters tested included total white blood cell count (WBC), absolute neutrophil and lymphocyte counts (Neu #, Lym #), percentages of neutrophils, lymphocytes, and monocytes (Neu %, Lym %, Mon %), red blood cell count (RBC), hemoglobin (HGB), hematocrit (HCT), mean corpuscular hemoglobin concentration (MCHC), platelet count (PLT), and platelet crit (PCT).

Serum samples were used for basic metabolic panel (BMP) testing and underwent heat inactivation (56 °C for 30 min) before testing. BMP testing was performed using an automated biochemical analyzer for animals (Zybio, EXC-2000), with 39 test indicators: total protein (TP), albumin (ALB), globulin (GLB), albumin/globulin ratio (ALB/GLB), alanine aminotransferase (ALT), aspartate aminotransferase (AST), alkaline phosphatase (ALP), total bilirubin (TBIL), direct bilirubin (DBIL), indirect bilirubin (IBIL), gamma-glutamyl transferase (GGT), uric acid (UA), creatinine (CREA), urea, triglycerides (TG), total cholesterol (CHOL), high-density lipoprotein cholesterol (HDL-C), low-density lipoprotein cholesterol (LDL-C), apolipoprotein A1 (ApoA1), apolipoprotein B (ApoB), glucose (GLU), creatine kinase (CK), CK-MB, lactate dehydrogenase (LDH), α-hydroxybutyrate dehydrogenase (α-HBDH), C-reactive protein (CRP), complement C3, complement C4, immunoglobulin A (IgA), immunoglobulin M (IgM), immunoglobulin G (IgG), lipoprotein (a) [Lp(a)], phosphorus (P), magnesium (Mg), calcium (Ca), iron (Fe), α-amylase (α-AMY), lipase (LPS), and ferritin (Fer).

Langtaosha (LTS) Preprint doi: https://doi.org/10.65215/apb7tn58 This version posted November 28, 2025. The copyright holder for this preprint (which was not certified by peer review) is the author/funder. Creative Commons license: CC Attribution-NonCommercial-NoDerivatives 4.0 https://creativecommons.org/licenses/by-nc-nd/4.0

Coagulation tests were conducted to characterize platelet function by monitoring activated partial thromboplastin time (APTT), prothrombin time (PT), fibrinogen (FIB), and thrombin time (TT). The fully automated coagulation analyzer was calibrated and quality-controlled by the manufacturer's recommended protocols (Sysmex, CA-620). Fresh plasma samples were collected daily for testing.

**Histopathology and Immunohistochemistry (IHC)**

On the seventh day post-infection, all rhesus macaques were euthanized. The post-mortem examination was conducted on the heart, liver, spleen, lung, kidney, pancreas, brain, inguinal lymph nodes, axillary lymph nodes, duodenum, and rectal tissues. During the collection of lung tissues, the right and left lobes were distinguished and further divided into upper, middle, and lower lobes. All tissues were immersed in a 4 % paraformaldehyde solution (Biosharp, Cat#BL539A) for 24 h to complete fixation. After fixation, the tissues were removed and trimmed to a uniform size under a fume hood.

For tissue embedding: Embedding frames containing tissue were placed into the cassette and dehydrated using a gradient of ethanol. In 75 % ethanol for 2 h, 85 % ethanol for 2 h, 95 % ethanol for 3 h, absolute ethanol for 2 h, xylene for 2 h, and melted paraffin for 2 h. The wax-soaked tissue was embedded by using a tissue embedder. Finally, the mold with tissue inside was covered by an embedding frame and then moved to the -20 °C freezing table for cooling. The paraffin block was removed from the mold after the paraffin solidified. The trimmed paraffin block was placed on the microtome to be sliced at a thickness of 4 μm. Sections were floated on 42 °C distilled water to be flattened and were picked up vertically by using a glass slide. After the tissue was dried, sections were placed in an incubator at 60 °C for 30 min to 1 h. Sections were removed from the incubator and stored at room temperature.

For H&E staining, tissue sections were immersed in xylene for 10 min. Tissue sections were immersed in progressively more dilute ethanol solutions. Then, they rehydrated in the following sequence: absolute ethanol for 5 min, 95 % ethanol for 5 min, 85 % ethanol for 5 min, and 75 % ethanol for 5 min. Rinsing with distilled water for 1 min. Sections were stained with a hematoxylin solution (BIOSSCI, Cat#BP0211) for 4 min and then washed with distilled water for 2 min until no excess dye

Langtaosha (LTS) Preprint doi: https://doi.org/10.65215/apb7tn58 This version posted November 28, 2025. The copyright holder for this preprint (which was not certified by peer review) is the author/funder. Creative Commons license: CC Attribution-NonCommercial-NoDerivatives 4.0 https://creativecommons.org/licenses/by-nc-nd/4.0

was visible on the sections. Sections were differentiated with 0.8 % hydrochloric acid alcohol for 2 sec. Sections were stained with an eosin solution (alcohol-soluble) for 20 sec without water washing. Then, the sections were treated with 95 % ethanol for 5 min and dehydrated with absolute ethanol for 4 min. The tissue sections were transparent after being treated with xylene and then mounted with neutral balsam.

For IHC staining, the sections were deparaffinized in an environmentally friendly dewaxing agent for 10 min, followed by hydration through absolute ethanol, 95 % ethanol, and 75 % ethanol, each for 5 min. The sections were then washed three times with distilled water for 3 min each. Antigen retrieval was performed using high-pressure and high-temperature EDTA (BIOSSCI, Cat#BP0610). After rinsing the sections with distilled water, they were immersed in a 3 % (v/v) $H_2O_2$ solution (SCR, Cat#10011218) and incubated at room temperature in the dark for 30 min to block endogenous peroxidase activity. The sections were marked with a histochemical pen and then incubated with normal goat serum (BOSTER, Cat#AR1009) at room temperature for 30 min to block non-specific binding sites. The primary antibody used was an anti-SFTSV-N polyclonal antibody (1:2000), which was incubated overnight at 4 °C. The following day, the sections were brought to room temperature and washed three times with TBST. The secondary antibody was an HRP-conjugated rabbit polyclonal antibody (1:5000, Promega, Cat#W4011), which was incubated at 37 °C for 45 min, followed by three washes with TBST. Each section was then incubated with 100 μL of DAB solution (MXB Biotechnologies, Cat#Kit-0038) at room temperature for 5 min to develop color, and the reaction was terminated by rinsing with tap water.

All sections were scanned using a digital pathology system (HAMAMATSU, NanoZoomer S360). The software NDP. View 2 was used for magnification observation. ImageJ software evaluates the sections method in the same way as the mouse challenge.

**Luminex assay**

All *rhesus macaques* were euthanized on the 7 dpi. Serum collected from 0 - 7 dpi was used for cytokine profile analysis. The serum was obtained by centrifuging whole blood in the clot activator tube

Langtaosha (LTS) Preprint doi: https://doi.org/10.65215/apb7tn58 This version posted November 28, 2025. The copyright holder for this preprint (which was not certified by peer review) is the author/funder. Creative Commons license: CC Attribution-NonCommercial-NoDerivatives 4.0 https://creativecommons.org/licenses/by-nc-nd/4.0

at 4 °C, 3,000 rpm for 10 min. For cytokine profiling, undergone heat inactivation at 56°C 30min serum samples were measured using a 22-analyte multiplex bead array (Millipore, Cat#PCYTMG-40K-PX22) including IL-2, IL-6, IL-17α, GM-CSF (1.22 - 5,000 pg/mL); IFN-γ, VEGF-α, IL-10 (2.44 - 10,000 pg/mL); G-CSF, IL-1RA, TNF-α (4.88 - 20,000 pg/mL); IL-8 (0.05-200 pg/mL); IL-5 (2.93-12,000 pg/mL); IL-4 (12.21-50,000 pg/mL); IL-1β (0.98-4,000 pg/mL); IL-23 (19.53-80,000 pg/mL); IL-15 (6.10-25,000 pg/mL); IL-18 (19.53-80,000 pg/mL); MIP-1α (0.73-3,000); MIP-1β (6.10-25,000 pg/mL); MCP-1 (3.05-12,500 pg/mL); sCD40L (48.83-200,000 pg/mL); TGF-α (0.49-2,000 pg/mL). Samples were prepared according to the manufacturer's instructions, and the Mean Fluorescent Intensity (MFI) was collected using the Bio-Plex 200 suspension array system, followed by standard curve fitting. Each test well was measured 50 times. The doublet discriminator parameter was set to 8000.

**Viral RNA extraction and quantification**

SFTSV viral RNA was detected using quantitative polymerase chain reaction (qPCR). Viral RNA was extracted from peripheral blood and trizol homogenates (Thermo Fisher Scientific, Cat#10296028) of heart, liver, spleen, lung, kidney, pancreas, brain, inguinal lymph nodes, axillary lymph nodes, duodenum, and rectal tissues using the high-throughput automatic nucleic acid extraction system (Thermo Fisher Scientific, KingFisher Flex). The weight is recorded when taking tissue samples, while the volume is recorded for peripheral blood. A one-step method (Thermo Fisher Scientific, Cat#4444434) was used for viral RNA quantification, with the SFTSV M segment forward primer: 5'-CAG TGC TAC CCT GCA AAG AA-3', reverse primer: 5'-TGA TGG CAA ACA TTA GCT TC-3', and probe: 5'-FAM/TCA TCC TCC TTG GAT ATG CAG GCC TCA/BHQ1-3'. The qPCR was carried out on a CFX384 Touch Real-Time PCR Detection System (BioRad) using the following thermal cycler parameters: 25 °C for 2 min, heat to 50 °C, hold for 15 min, heat to 95 °C, hold for 2 min, then the following parameters are repeated for 40 cycles: heat to 95 °C, hold for 5 sec, cool to 60 °C (collect fluorescence signals) and hold for 31 sec. The reaction system consists of 20 μL, including 1 μL of each primer and probe, 5 μL of one-step polymerase, 5 μL of the RNA sample, and 7 μL of nuclease-free water. RNA copies per reaction were

Langtaosha (LTS) Preprint doi: https://doi.org/10.65215/apb7tn58 This version posted November 28, 2025. The copyright holder for this preprint (which was not certified by peer review) is the author/funder. Creative Commons license: CC Attribution-NonCommercial-NoDerivatives 4.0 https://creativecommons.org/licenses/by-nc-nd/4.0

interpolated using quantification cycle data and a serial dilution of a highly characterized custom RNA containing the SFTSV M segment sequence.

**NHP Single-cell Sequencing**

Single-cell transcriptome libraries were generated following the manufacturer's protocol for the Chromium Next GEM Single Cell 3' Kit (v3.1, 10x Genomics, Cat#1000268). Briefly, cellular suspensions containing between 10,000 and 20,000 cells per sample were partitioned into Gel Bead-In-EMulsions (GEMs) using the 10X Chromium Controller. Within each GEM, reverse transcription was performed using oligonucleotides that incorporated template-switching functionality and 16-base pair unique molecular identifiers (UMIs). These UMIs were employed to uniquely tag individual mRNA molecules, enabling precise quantification and mitigation of amplification biases and PCR duplicates during downstream analysis.

The resulting cDNA was amplified for 14 PCR cycles, a number optimized to preserve library complexity while minimizing the generation of duplicate reads. Final sequencing libraries were normalized to a concentration of 2 nM and pooled in equimolar amounts. Paired-end sequencing (2 × 150 bp) was performed on an Illumina NovaSeq 6000 (Illumina) instrument equipped with S4 flow cells, yielding a target depth exceeding 50,000 reads per cell. Post-sequencing, the embedded UMIs were used to correct PCR and sequencing errors computationally and to collapse PCR duplicates, ensuring accurate digital gene expression counting.

**NHP Sequencing Data Processing and Cell Type Identification**

For the single-cell transcriptome sequencing data obtained from 8 rhesus macaque PBMCs and spleens, we applied the Cell Ranger (v7.2) workflow for the assembly and annotation of the raw sequencing data. The reference genome used was the Mmul_10 (GCF_003339765.1) rhesus macaque reference genome downloaded from GenBank. The expression matrix processed by Cell Ranger was further analyzed using the Seurat R package for downstream dimensionality reduction, clustering, and cell

Langtaosha (LTS) Preprint doi: https://doi.org/10.65215/apb7tn58 This version posted November 28, 2025. The copyright holder for this preprint (which was not certified by peer review) is the author/funder. Creative Commons license: CC Attribution-NonCommercial-NoDerivatives 4.0 https://creativecommons.org/licenses/by-nc-nd/4.0

annotation. For the integrated object, cells with nFeature greater than 200 and less than 8,000, and nCount less than 90,000 were filtered for subsequent analysis. A total of 98,412 PBMC cells and 65,406 spleen cells were included in the study after filtering. After removing batch effects, we performed dimensionality reduction and clustering on the data. We calculated gene expression across all clusters using the FindAllMarkers and AverageExpression functions, and annotated cell types and subtypes through a hybrid approach combining manual annotation with automated tools. Automated annotation methods included SingleR and SCSA.

**Enrichment Analysis of Differential Genes**

We used the GSVA package for GSVA (Gene Set Variation Analysis) analysis and the limma package for differential calculation. The gene set database used for GSVA analysis comprised all gene sets under the BP (Biological Process) subontology of the GO database. For immune-related GSVA differences of interest, we filtered these gene sets using keyword-based criteria. Immune-related gene sets obtained from this filtering were further analyzed to identify differential immune pathway activities.

**Intercellular Communication Analysis**

We used the CellChat package to analyze intercellular communication with the "Secreted Signaling" interaction database. We selected "RNA" as the computational assay, set k.min to 10 and nboot to 100 to calculate communication probabilities, and applied min.cell = 10 to filter interactions. Cell-cell communication analyses were performed at multiple classification hierarchies to observe signaling states across different resolutions. For prioritized signaling pathways, we conducted detailed interaction analyses and further examined expression patterns of ligand-receptor pair genes.

**Inflammatory Scoring Analysis**

Langtaosha (LTS) Preprint doi: https://doi.org/10.65215/apb7tn58 This version posted November 28, 2025. The copyright holder for this preprint (which was not certified by peer review) is the author/funder. Creative Commons license: CC Attribution-NonCommercial-NoDerivatives 4.0 https://creativecommons.org/licenses/by-nc-nd/4.0

We evaluated cellular-level activity of four immune responses - cytotoxicity, negative_inflammatory, apoptosis, and ISG - using the AddModuleScore function. Reference gene sets for these immune responses are detailed in ***Table S4***.

**Quantification and Statistical Analysis**

Data visualization was performed using the R package ggplot2 and GraphPad Prism 10. For inter-group comparisons between experimental and control groups, statistical analyses employed paired t-tests and the limma method, selected based on data type and analytical objectives. Spearman correlation analysis was applied for association testing.

Langtaosha (LTS) Preprint doi: https://doi.org/10.65215/apb7tn58 This version posted November 28, 2025. The copyright holder for this preprint (which was not certified by peer review) is the author/funder. Creative Commons license: CC Attribution-NonCommercial-NoDerivatives 4.0 https://creativecommons.org/licenses/by-nc-nd/4.0

# SUPPLEMENTARY FIGURES

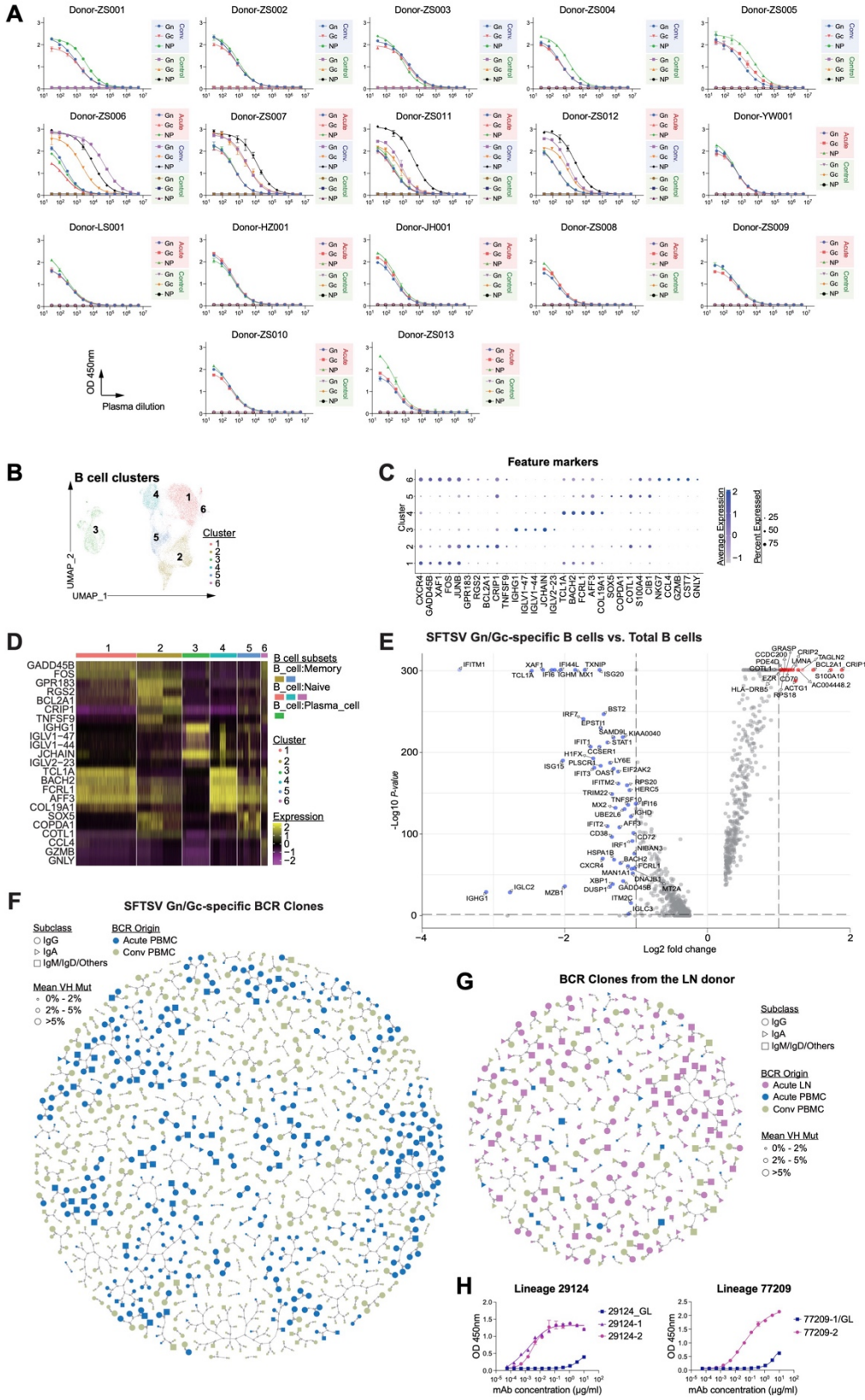

Langtaosha (LTS) Preprint doi: https://doi.org/10.65215/apb7tn58 This version posted November 28, 2025. The copyright holder for this preprint (which was not certified by peer review) is the author/funder. Creative Commons license: CC Attribution-NonCommercial-NoDerivatives 4.0 https://creativecommons.org/licenses/by-nc-nd/4.0

**Fig. S1. Single Cell Transcriptome and BCR Profiling in SFTSV-Infected Humans. (A)** Plasma ELISA binding assay. Plasma samples from donors in the acute and convalescent (conv) phases of SFTSV infection were tested for binding to SFTSV NP, Gn, or Gc proteins, with plasma from an uninfected individual serving as a negative control. **(B-D)** Clustering of total B Cells based on scRNA-seq. B cell subpopulations were identified based on unique gene expression profiles, visualized as a UMAP plot showing six subpopulations (B). Gene expression of feature cell markers across different B cell subpopulations is displayed as dot plots (C) and a heatmap (D). **(E)** Comparison between FACS-sorted SFTSV Gn/Gc-specific B cells and total B cells reveals genes with >2-fold change and $p<0.05$, highlighted in blue (down-regulated) and red (up-regulated). **(F)** Gn/Gc-specific BCR clones, as determined by BCR genes from FACS-sorted SFTSV Gn/Gc-specific B cells and their clone-related BCR genes from total B cells during the acute and convalescent phases of SFTSV infection. **(G)** BCRs derived from lymph node (LN) B cells and their clone-related BCRs from PBMCs. **(H)** Antibodies from two clonal lineages, 29124 and 77209, composed of both LN- and PBMC-derived BCRs, were recombinantly expressed and tested for ELISA binding to the SFTSV Gn protein. GL indicates germline.

Langtaosha (LTS) Preprint doi: https://doi.org/10.65215/apb7tn58 This version posted November 28, 2025. The copyright holder for this preprint (which was not certified by peer review) is the author/funder. Creative Commons license: CC Attribution-NonCommercial-NoDerivatives 4.0 https://creativecommons.org/licenses/by-nc-nd/4.0

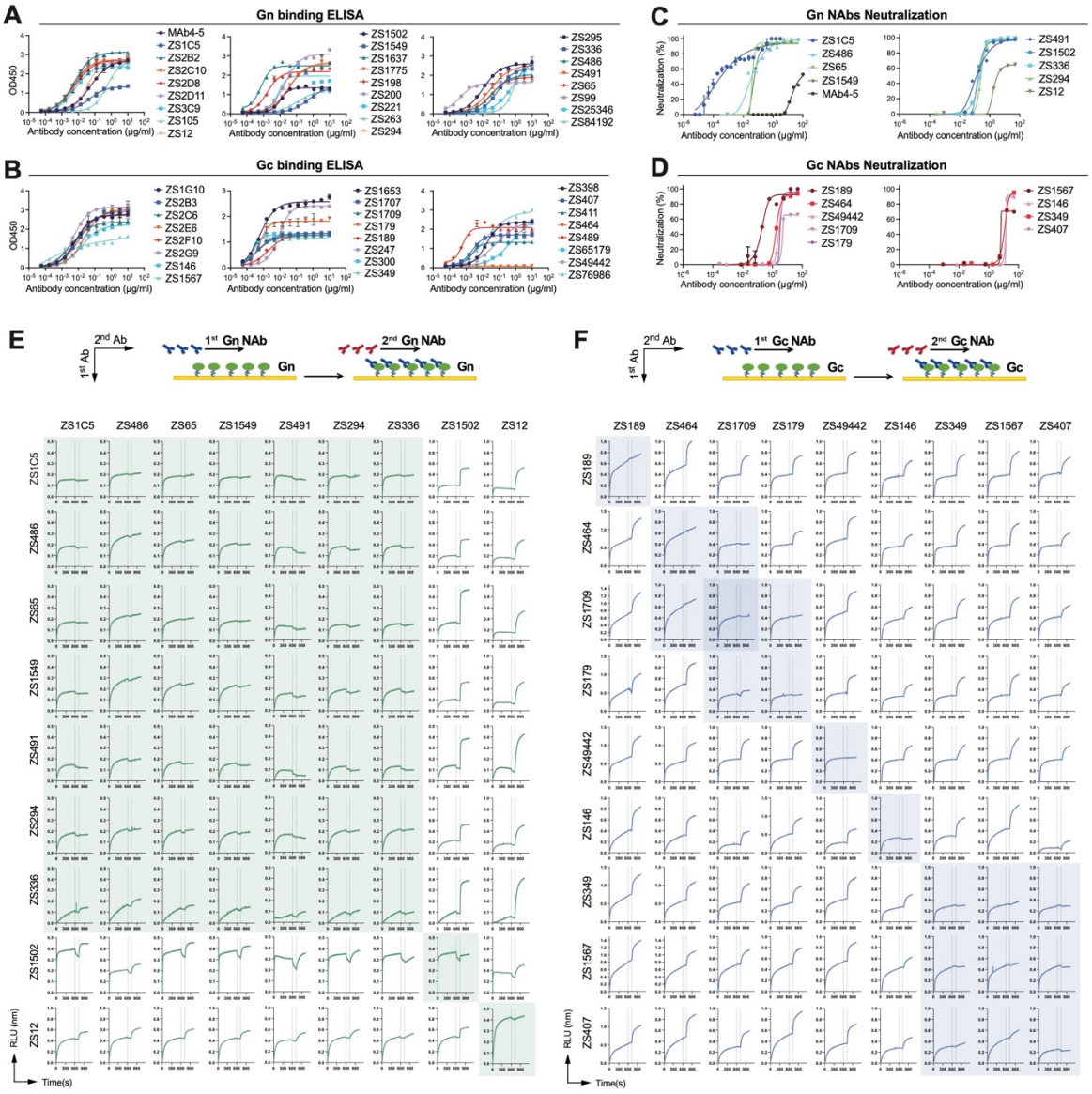


**Fig. S2. Characterization of SFTSV Gn/Gc-Specific Antibodies**. **(A-B)** ELISA curves of purified Gn/Gc-specific antibodies binding on SFTSV Gn (A) or Gc (B). **(C-D)** Neutralization assays were conducted for Gn-reactive (C) and Gc-reactive (D) antibodies using authentic SFTSV (genotype C4, strain WCH/97/HN/China/2011) in Vero cells. **(E-F)** Cross-competition activities of NAbs tested by BLI. SFTSV Gn (E) or Gc (F) were captured by one NAb (indicated on the y-axis), with a second NAb binding (indicated on the x-axis). The change in relative light units (ΔRLU) was calculated by subtracting the RLU of the first NAb from that of the second NAb. Antibodies were grouped based on their cross-competition patterns.

Langtaosha (LTS) Preprint doi: https://doi.org/10.65215/apb7tn58 This version posted November 28, 2025. The copyright holder for this preprint (which was not certified by peer review) is the author/funder. Creative Commons license: CC Attribution-NonCommercial-NoDerivatives 4.0 https://creativecommons.org/licenses/by-nc-nd/4.0

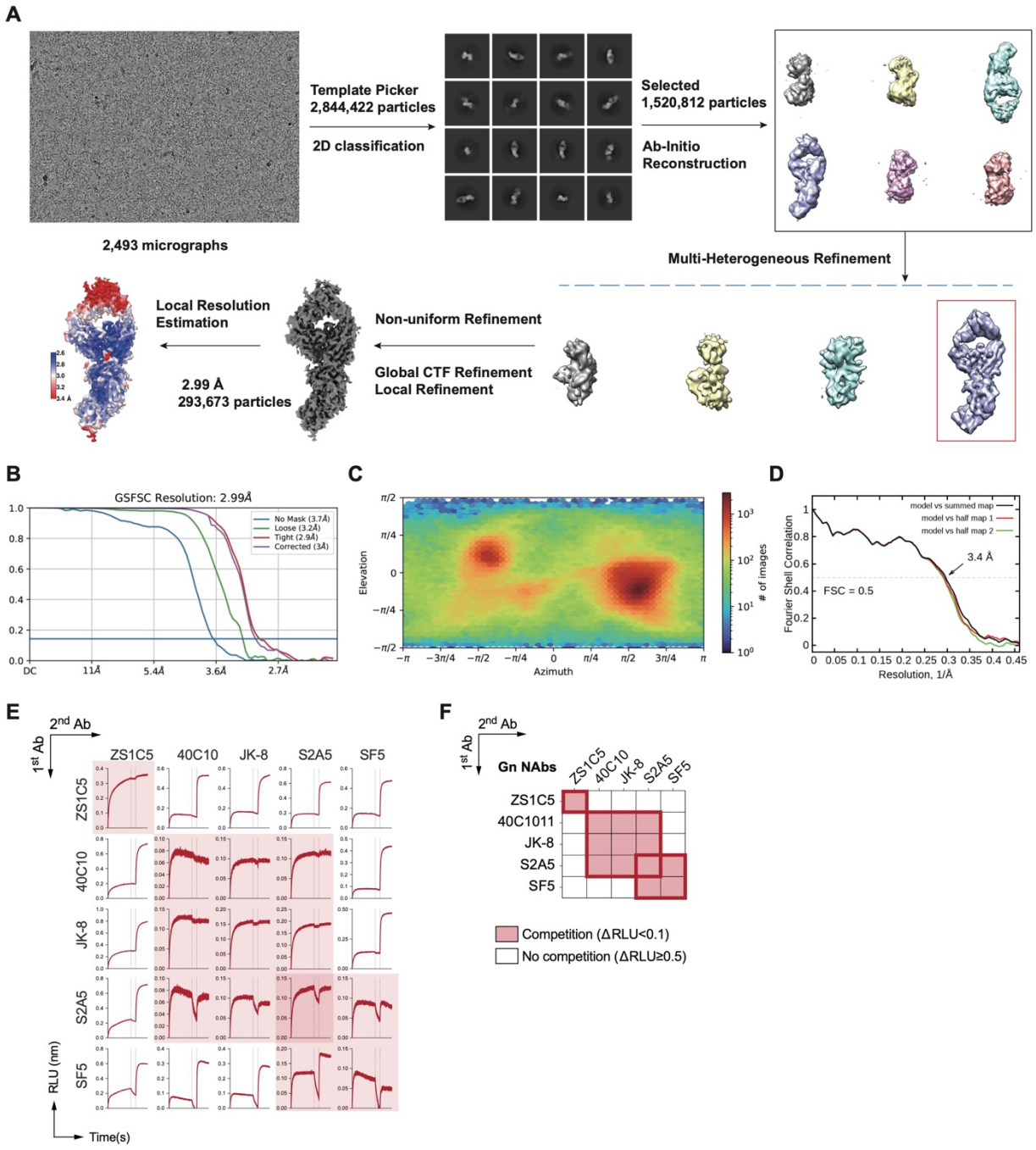


**Fig. S3. Cryo-EM analysis of Gn bound with ZS1C5. (A)** Flowchart for cryo-EM data processing. See the "Data Processing" section in Methods for details. **(B-D)** Gold standard FSC curves (B), Euler distribution plots (C), FSC curves for cross-validation of the structure (D) of Gn bound with ZS1C5. **(E-F)** Cross-competetion activities of ZS1C5 with previously reported NAbs tested by BLI. SFTSV Gn were captured by one NAb (indicated on the y-axis), followed by the binding of a second NAb (indicated on

Langtaosha (LTS) Preprint doi: https://doi.org/10.65215/apb7tn58 This version posted November 28, 2025. The copyright holder for this preprint (which was not certified by peer review) is the author/funder. Creative Commons license: CC Attribution-NonCommercial-NoDerivatives 4.0 https://creativecommons.org/licenses/by-nc-nd/4.0

the x-axis). The change in relative light units (△RLU) was calculated as the RLU of the second NAb minus the RLU of the first NAb. Antibodies were clustered based on cross-competetion patterns and shown as BLI curves (E) and heatmap (F).

Langtaosha (LTS) Preprint doi: https://doi.org/10.65215/apb7tn58 This version posted November 28, 2025. The copyright holder for this preprint (which was not certified by peer review) is the author/funder. Creative Commons license: CC Attribution-NonCommercial-NoDerivatives 4.0 https://creativecommons.org/licenses/by-nc-nd/4.0

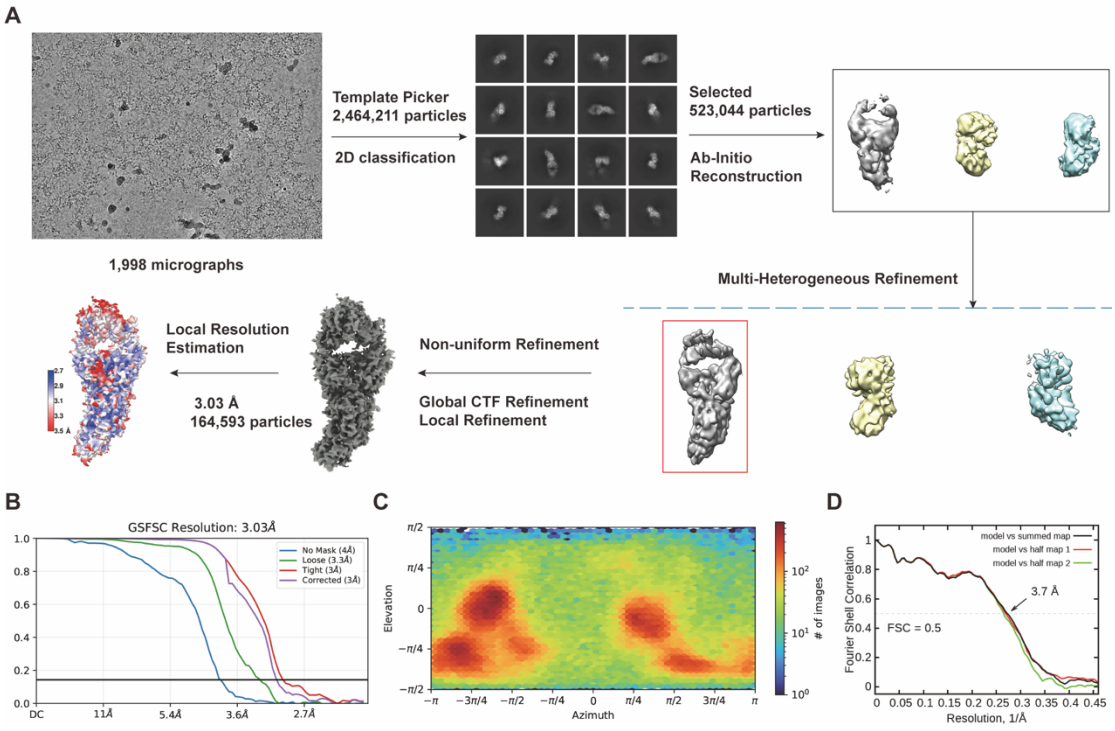


**Fig. S4. Cryo-EM analysis of Gn respectively bound with ZS336. (A)** Flowchart for cryo-EM data processing. See the "Data Processing" section in Methods for details. **(B-D)** Gold standard FSC curves (B), Euler distribution plots (C), FSC curves for cross-validation of the structure (D) of Gn bound with ZS336.

Langtaosha (LTS) Preprint doi: https://doi.org/10.65215/apb7tn58 This version posted November 28, 2025. The copyright holder for this preprint (which was not certified by peer review) is the author/funder. Creative Commons license: CC Attribution-NonCommercial-NoDerivatives 4.0 https://creativecommons.org/licenses/by-nc-nd/4.0

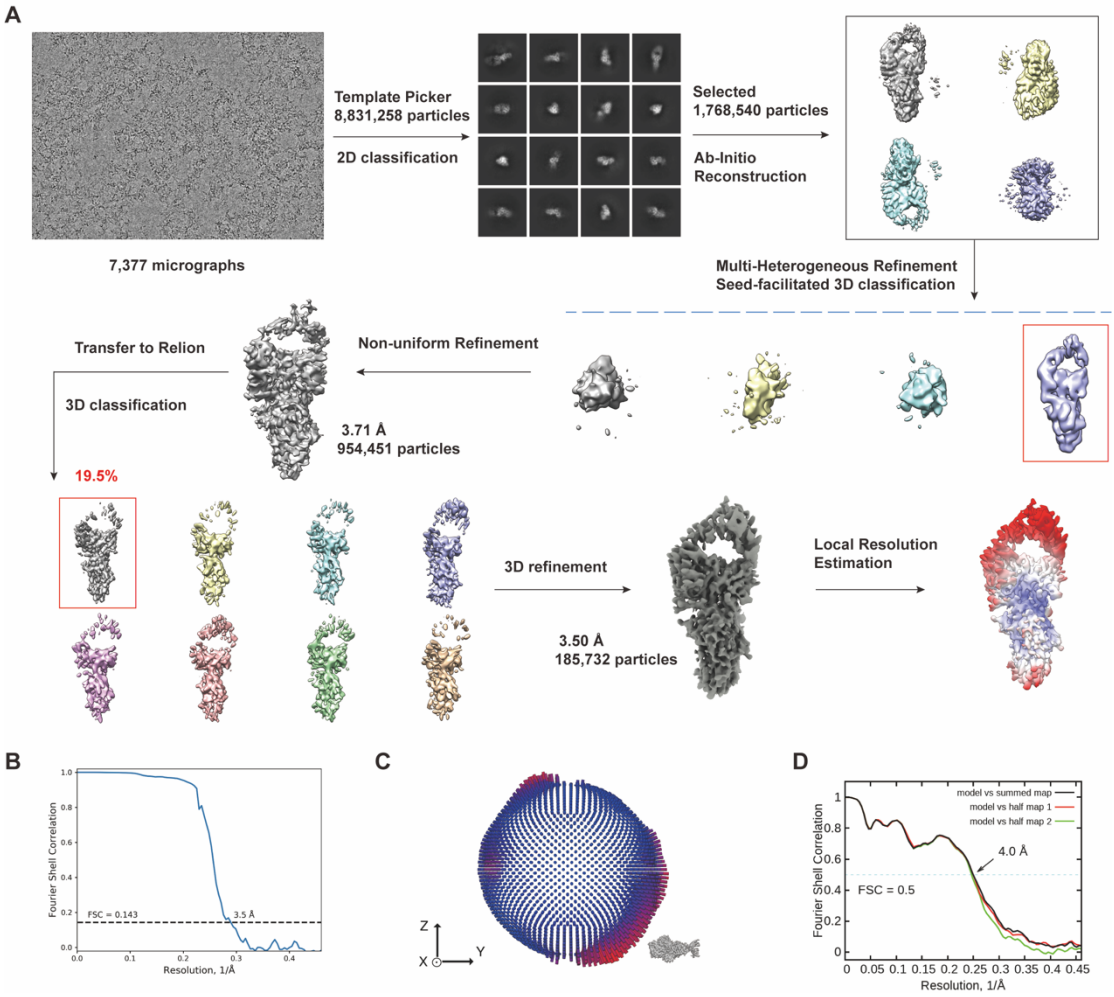


**Fig. S5. Cryo-EM analysis of Gn respectively bound with ZS65. (A)** Flowchart for cryo-EM data processing. See the "Data Processing" section in Methods for details. **(B-D)** Gold standard FSC curves (B), Euler distribution plots (C), FSC curves for cross-validation of the structure (D) of Gn bound with ZS65.

Langtaosha (LTS) Preprint doi: https://doi.org/10.65215/apb7tn58 This version posted November 28, 2025. The copyright holder for this preprint (which was not certified by peer review) is the author/funder. Creative Commons license: CC Attribution-NonCommercial-NoDerivatives 4.0 https://creativecommons.org/licenses/by-nc-nd/4.0

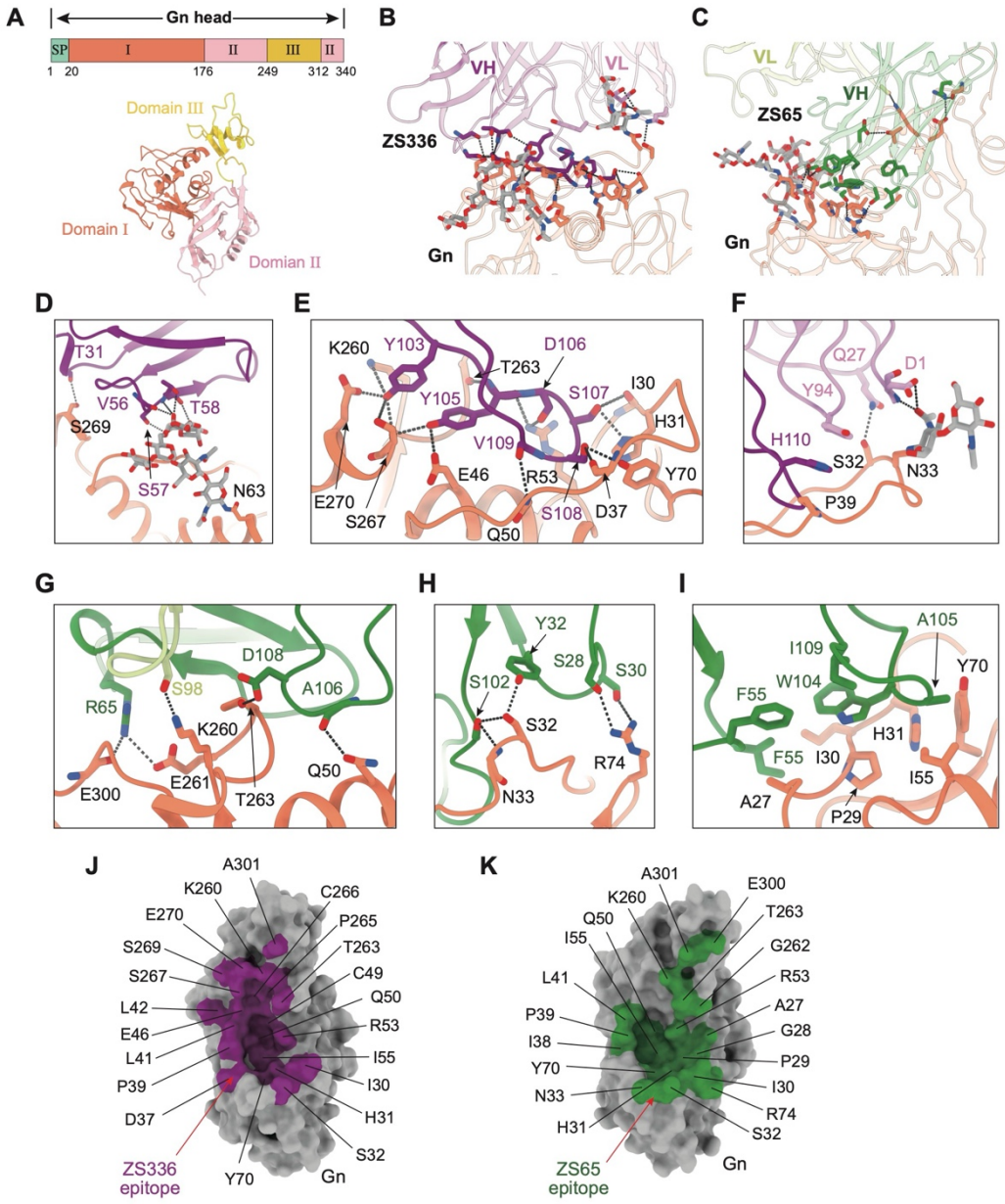


**Fig. S6. Interaction Interface and Epitope Identification of Gn Complexed with ZS336 and ZS65. (A)** Schematic representation and cryo-EM structure of the Gn head colored by domains. Signal peptide (SP) is in light green. Domain I of Gn: orange; Domain II of Gn: pink; Domain III of Gn: yellow. **(B)** Binding interface between Gn and ZS336. **(C)** Binding interface between Gn and ZS65. **(D-F)** Key interfacing residues between Gn and ZS336. (D) Salt bridges; (E) H-bonds; (F) hydrophobic interactions. Gn: orange; the heavy chain of ZS336: purple; the light chain of ZS336: violet. All residues are shown as

Langtaosha (LTS) Preprint doi: https://doi.org/10.65215/apb7tn58 This version posted November 28, 2025. The copyright holder for this preprint (which was not certified by peer review) is the author/funder. Creative Commons license: CC Attribution-NonCommercial-NoDerivatives 4.0 https://creativecommons.org/licenses/by-nc-nd/4.0

sticks and colored by heteroatom. Dashed lines indicate polar interactions. **(G-I)** Key interfacing residues between Gn and ZS65. (G) Salt bridges; (H) H-bonds; (I) hydrophobic interactions. Gn: orange; the heavy chain of ZS65: forest; the light chain of ZS65: pale green. All residues are shown as sticks and colored by heteroatom. Dashed lines indicate polar interactions. **(J)** Footprints of ZS336 on the Gn surface. **(K)** Footprints of ZS65 on the Gn surface.

Langtaosha (LTS) Preprint doi: https://doi.org/10.65215/apb7tn58 This version posted November 28, 2025. The copyright holder for this preprint (which was not certified by peer review) is the author/funder. Creative Commons license: CC Attribution-NonCommercial-NoDerivatives 4.0 https://creativecommons.org/licenses/by-nc-nd/4.0

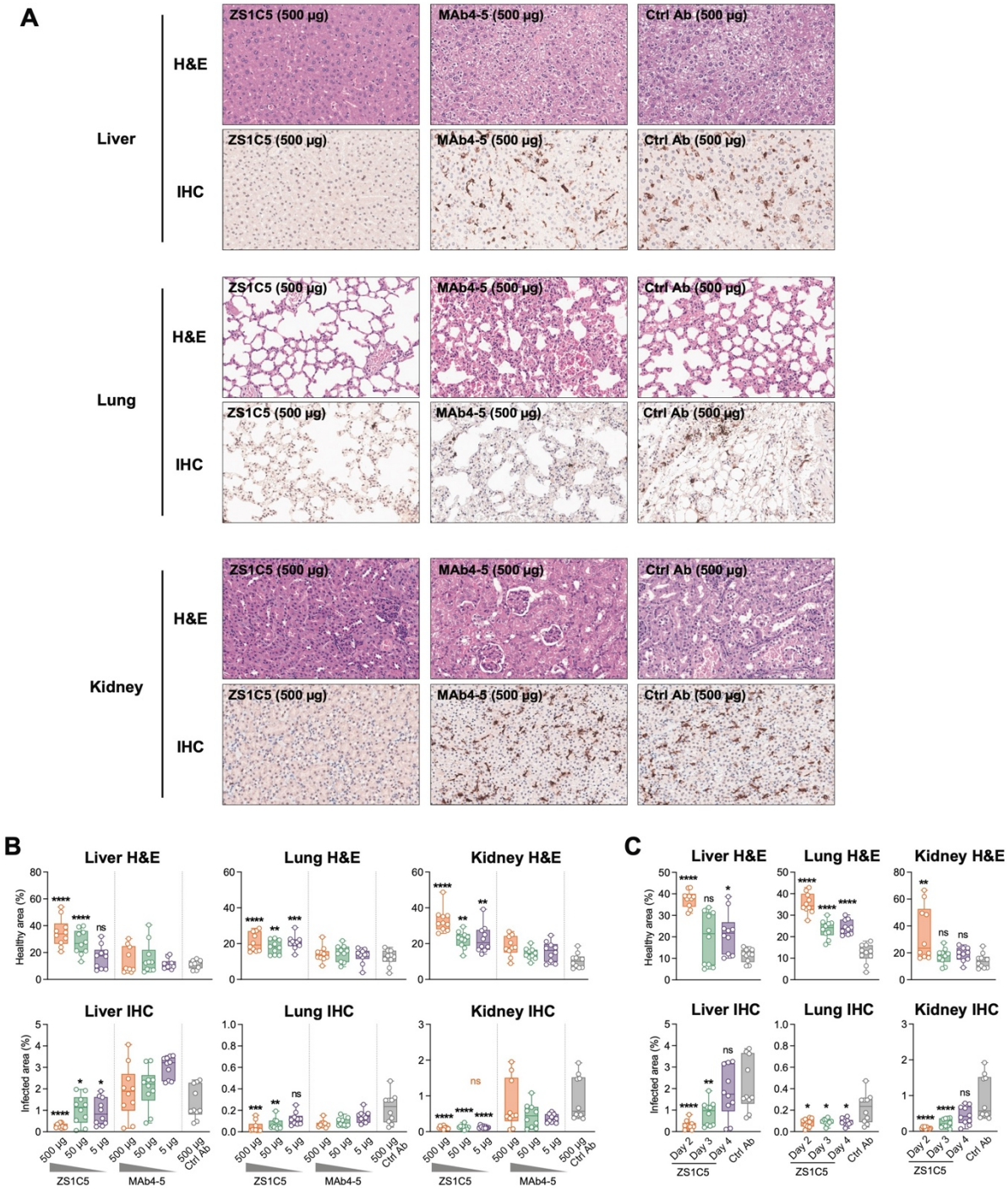


**Fig. S7. Pathological changes in mouse protection studies. (A)** Representative H&E and IHC staining images for liver, Lung and kidney. **(B)** H&E and IHC staining scores from the dose study. Related to Fig. 5A-G. **(C)** H&E and IHC staining scores from the time-point study. Related to Fig. 5H-K.

Langtaosha (LTS) Preprint doi: https://doi.org/10.65215/apb7tn58 This version posted November 28, 2025. The copyright holder for this preprint (which was not certified by peer review) is the author/funder. Creative Commons license: CC Attribution-NonCommercial-NoDerivatives 4.0 https://creativecommons.org/licenses/by-nc-nd/4.0

Dots and error bars represent mean±SEM of scores. Statistical significance was determined using the Wilcoxon Rank Sum Test. Asterisks indicate statistical significance between the specified group and the control antibody group: ns, not significant; *$p < 0.05$; **$p < 0.01$; ***$p < 0.001$; ****$p < 0.0001$.

Langtaosha (LTS) Preprint doi: https://doi.org/10.65215/apb7tn58 This version posted November 28, 2025. The copyright holder for this preprint (which was not certified by peer review) is the author/funder. Creative Commons license: CC Attribution-NonCommercial-NoDerivatives 4.0 https://creativecommons.org/licenses/by-nc-nd/4.0

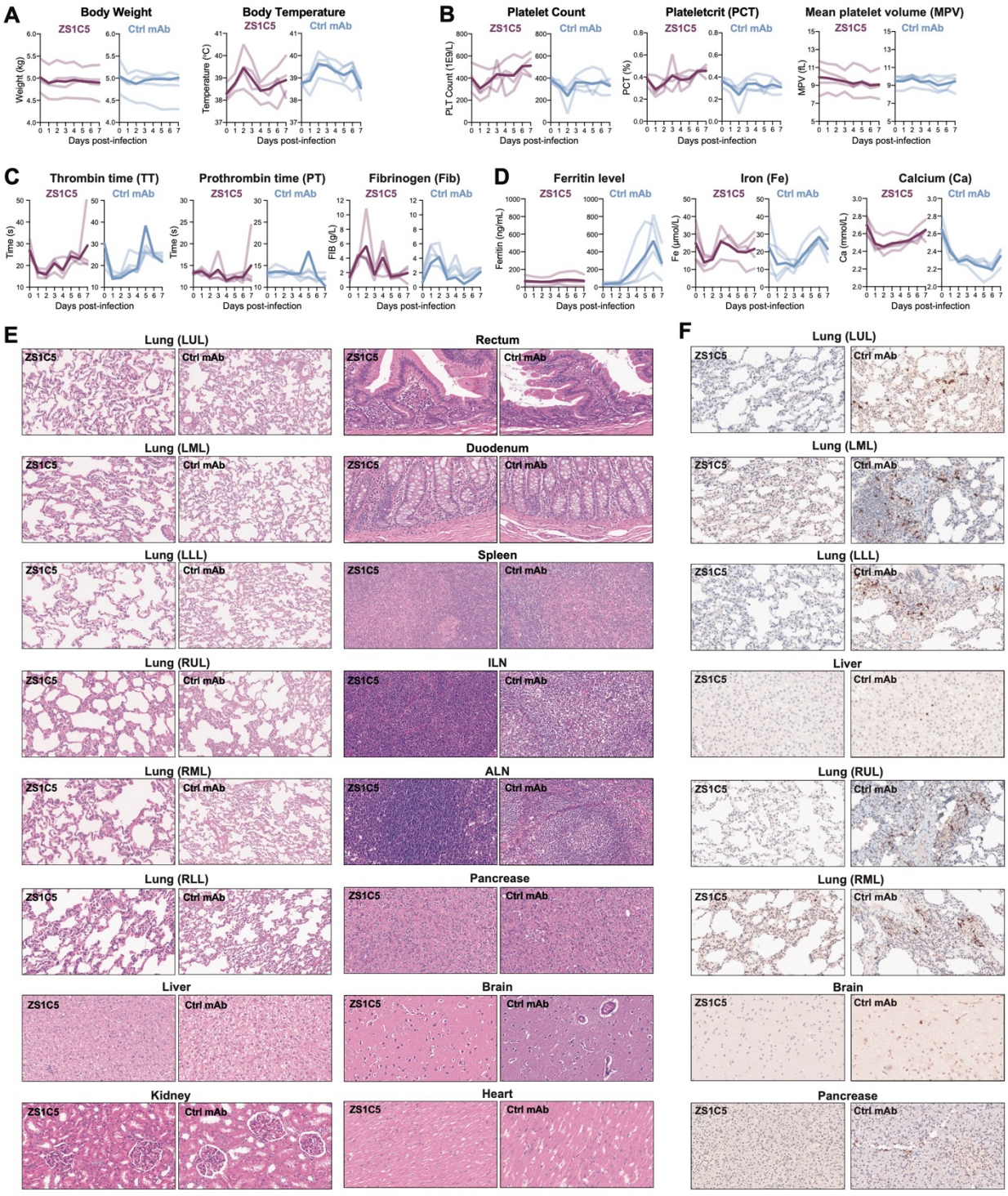


**Fig. S8. Symptom and pathological changes in NHP protection studies. (A)** Changes in Body weight and temperature. **(B)** Platelet-related tests. Daily monitoring of platelet count (PLT), plateletcrit (PCT), and mean platelet volume (MPV) through complete blood count (CBC) tests. **(C)** Blood

Langtaosha (LTS) Preprint doi: https://doi.org/10.65215/apb7tn58 This version posted November 28, 2025. The copyright holder for this preprint (which was not certified by peer review) is the author/funder. Creative Commons license: CC Attribution-NonCommercial-NoDerivatives 4.0 https://creativecommons.org/licenses/by-nc-nd/4.0

coagulation tests. Thrombin time (TT), prothrombin time (PT) and fibrinogen (Fib) levels for each animal were recorded daily through coagulation tests. **(D)** Blood ferritin, iron and calcium levels measured daily via comprehensive metabolic panel (CMP) tests. **(E)** Representative H&E staining of multiple tissues. **(F)** Representative IHC staining of tissues. Additional images complement those shown in Fig. 6H.

Langtaosha (LTS) Preprint doi: https://doi.org/10.65215/apb7tn58 This version posted November 28, 2025. The copyright holder for this preprint (which was not certified by peer review) is the author/funder. Creative Commons license: CC Attribution-NonCommercial-NoDerivatives 4.0 https://creativecommons.org/licenses/by-nc-nd/4.0

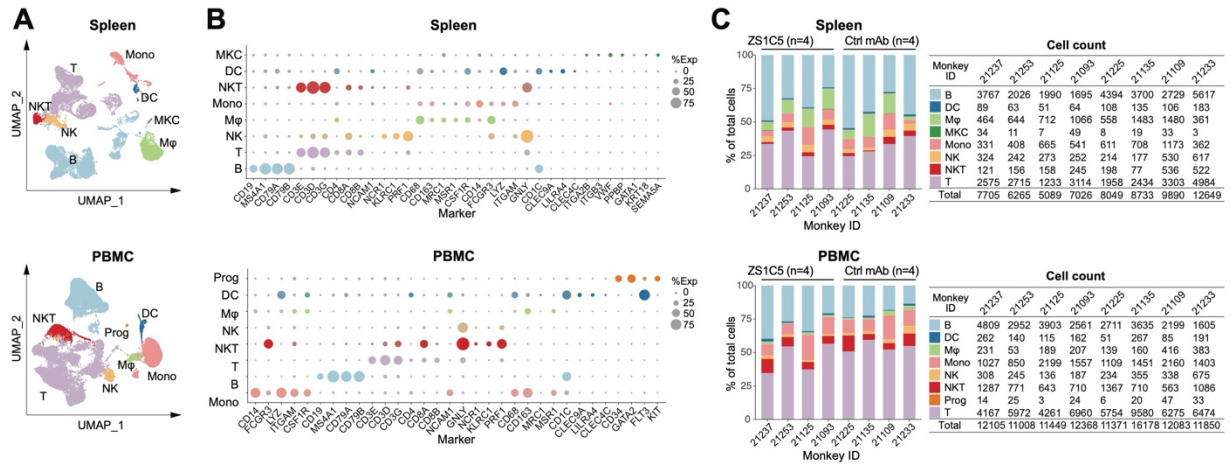


**Fig. S9. Single-cell atlas of NHP spleen and PBMC cells. (A)** The representative UMAP plot illustrates the distribution of single cells analyzed from one monkey, revealing distinct cell types. **(B)** Cell marker gene expression in different cell types shown as dot plots. Dot size indicates expression of indicated markers in each cell types. MKC, megakaryocyte; DC, dendritic cell; NK, natural killer cell; NKT, Natural killer T cell; Mono, monocyte; Mφ, macrophage; Prog, progenitor cell. **(C)** Proportions of all the cell types in spleen and PBMC samples. Data from each individual monkeys were shown as percentages in bar charts and shown as cell counts in tables.

Langtaosha (LTS) Preprint doi: https://doi.org/10.65215/apb7tn58 This version posted November 28, 2025. The copyright holder for this preprint (which was not certified by peer review) is the author/funder. Creative Commons license: CC Attribution-NonCommercial-NoDerivatives 4.0 https://creativecommons.org/licenses/by-nc-nd/4.0

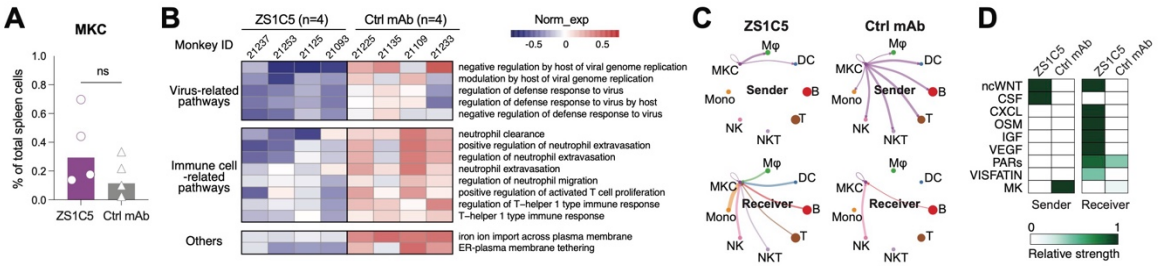


**Fig. S10. Single-cell transcriptomic profiling of megakaryocyte (MKCs). (A)** Comparison of the percentages of spleen MKC in the two groups. Each dot represents one animal, and bars represent mean values. Ns, not statistically significant (Wilcoxon Rank Sum Test). **(B)** Heatmap depicting GSVA score of differentially expressed gene sets in MKC of each animals using selected GOBP gene sets. The gene sets were selected from GOBP gene sets by virus- or immune-related terms. **(C)** Circle plots showing the intercellular interaction of MKCs as sender and receiver. Thickness of the connection lines indicate strength of interaction. **(D)** Heatmaps for comparison the overall communication strength for each signaling pathways in MKCs between ZS1C5 and control mAb groups. The y-axis displays differentially expressed signaling pathways involved in intercellular communication.

Langtaosha (LTS) Preprint doi: https://doi.org/10.65215/apb7tn58 This version posted November 28, 2025. The copyright holder for this preprint (which was not certified by peer review) is the author/funder. Creative Commons license: CC Attribution-NonCommercial-NoDerivatives 4.0 https://creativecommons.org/licenses/by-nc-nd/4.0

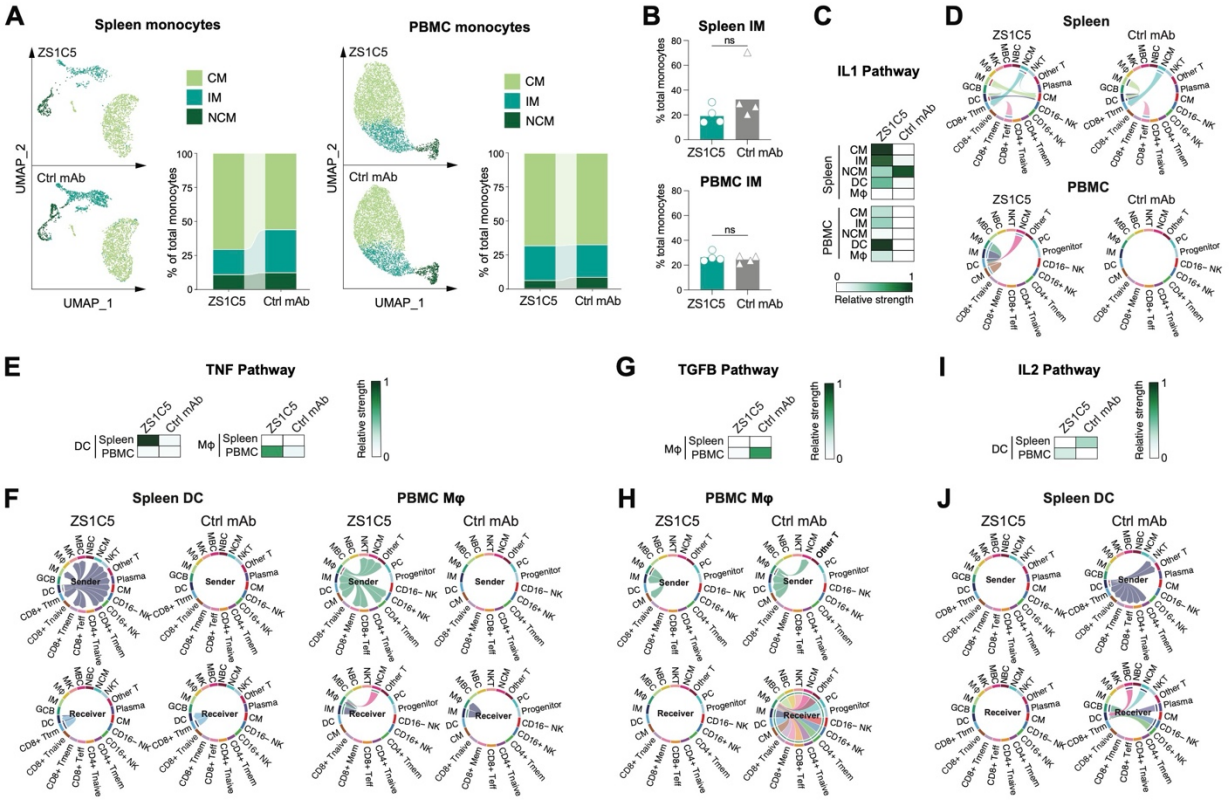


1444

1445 **Fig. S11. Single-cell transcriptomic analysis of monocytes. (A)** Spleen and PBMC monocyte

1446 subtypes from ZS1C5-treated and control mAb-treated macaques are visualized using UMAP

1447 dimensionality reduction. Subtype proportions are displayed in bar charts. CM, classical monocyte;

1448 NCM, non-classical monocyte; IM, intermediate monocyte. **(B)** Bar charts showing the percentages of

1449 spleen and PBMC IM in the two groups. **(C-D)** Intercellular interaction strength of IL1 pathway shown as

1450 heatmap (C) and chord plots (D) in CM, IM, NCM, DC and macrophages. **(E)** Heatmap shows

1451 intercellular interaction strength of TNF pathway in DC and macrophages. **(F)** Chord plots divided into

1452 sender and receiver show intercellular interaction strength in spleen DC and PBMC macrophages. **(G)**

1453 Heatmap shows intercellular interaction strength of TGFB pathway in macrophages. **(H)** Chord plots

1454 divided into sender and receiver show intercellular interaction strength in PBMC macrophages. **(I)**

1455 Heatmap shows intercellular interaction strength of IL2 pathway in DC. **(J)** Chord plots divided into

1456 sender and receiver show intercellular interaction strength in spleen DC. For bar charts, each dot

Langtaosha (LTS) Preprint doi: https://doi.org/10.65215/apb7tn58 This version posted November 28, 2025. The copyright holder for this preprint (which was not certified by peer review) is the author/funder. Creative Commons license: CC Attribution-NonCommercial-NoDerivatives 4.0 https://creativecommons.org/licenses/by-nc-nd/4.0

represents one animal, and bars represent mean values. Ns, not statistically significant (Wilcoxon Rank Sum Test). For chord plots, external rings represent cell subsets. Internal arrows represent intercellular communication in these pathways. Internal arcs represent receptor subsets and their proportion of output signals.

Langtaosha (LTS) Preprint doi: https://doi.org/10.65215/apb7tn58 This version posted November 28, 2025. The copyright holder for this preprint (which was not certified by peer review) is the author/funder. Creative Commons license: CC Attribution-NonCommercial-NoDerivatives 4.0 https://creativecommons.org/licenses/by-nc-nd/4.0

## SUPPLEMENTARY TABLES

**Table S1.** Immunogenetic analysis and experimental data of SFTSV Gn/Gc-specific antibodies (in Figure 1), ZS1C5-like antibodies and germline-encoded antibodies (in Figure 7). * Asterisk indicates antibodies derived from the 314 shared clones shown in Figure 1B.

**Table S2.** Cryo-EM data collection and refinement statistics of Gn complex with antibodies.

| | | | |
|---|---|---|---|
| **Data collection** | | | |
| EM equipment | Titan Krios (Thermo Fisher Scientific) | | |
| Voltage (kV) | 300 | | |
| Detector | Gatan K3 Summit | | |
| Energy filter | Gatan GIF Quantum, 20 eV slit | | |
| Pixel size (Å) | 1.087 | | |
| Electron dose (e-/Å2) | 50 | | |
| Defocus range (μm) | -1.2 ~ -2.2 | | |
| Number of collected micrographs | 2,493 | 1,998 | 7,377 |
| Sample | Gn-ZS1C5 | Gn-ZS336 | Gn-ZS65 |
| **3D Reconstruction** | | | |
| Software | cryoSPARC | cryoSPARC | cryoSPARC/Relion |
| Number of used particles | 367,785 | 164,593 | 185,732 |
| Resolution (Å) | 2.99 | 3.03 | 3.50 |
| Symmetry | C1 | | |
| Map sharpening B factor (Å$^2$) | -159.4 | -158.1 | -90 |
| **Refinement** | | | |
| Software | Phenix | | |
| Cell dimensions (Å) | 217.4 | | |

Langtaosha (LTS) Preprint doi: https://doi.org/10.65215/apb7tn58 This version posted November 28, 2025. The copyright holder for this preprint (which was not certified by peer review) is the author/funder. Creative Commons license: CC Attribution-NonCommercial-NoDerivatives 4.0 https://creativecommons.org/licenses/by-nc-nd/4.0

| | | | |
|---|---|---|---|
| Model composition | | | |
| Protein residues | 764 | 754 | 768 |
| NAG | 3 | 4 | 4 |
| MAN | 4 | 4 | 4 |
| R.m.s deviations | | | |
| Bonds length (Å) | 0.007 | 0.008 | 0.008 |
| Bonds Angle (°) | 1.081 | 1.015 | 1.003 |
| Ramachandran plot statistics (%) | | | |
| Preferred | 93.54 | 91.98 | 91.62 |
| Allowed | 5.67 | 8.02 | 8.38 |
| Outlier | 0.79 | 0.00 | 0 |

**Table S3.** Raw data from the NHP study in Figure 6 and 7, including symptom scores, body temperatures, CBC, CMP, and Luminex tests.

**Table S4.** Gene sets used for gene signature scoring in Figure 7.